

SYNTHESIS OF CALCIUM CARBONATE PARTICLES FOR BIOMEDICAL  
APPLICATIONS

A THESIS SUBMITTED TO  
THE GRADUATE SCHOOL OF NATURAL AND APPLIED SCIENCES  
OF  
MIDDLE EAST TECHNICAL UNIVERSITY

BY

ÇAĞATAY MERT ORAL

IN PARTIAL FULFILLMENT OF THE REQUIREMENTS  
FOR  
THE DEGREE OF MASTER OF SCIENCE  
IN  
METALLURGICAL AND MATERIALS ENGINEERING

JULY 2020



Approval of the thesis:

**SYNTHESIS OF CALCIUM CARBONATE PARTICLES FOR  
BIOMEDICAL APPLICATIONS**

submitted by **ÇAĞATAY MERT ORAL** in partial fulfillment of the requirements  
for the degree of **Master of Science in Metallurgical and Materials Engineering,**  
**Middle East Technical University** by,

Prof. Dr. Halil Kalıpçılar  
Dean, Graduate School of **Natural and Applied Sciences** \_\_\_\_\_

Prof. Dr. C. Hakan Gür  
Head of the Department, **Metallurgical and Materials Eng.** \_\_\_\_\_

Assoc. Prof. Dr. Batur Ercan  
Supervisor, **Metallurgical and Materials Eng., METU** \_\_\_\_\_

Assist. Prof. Dr. Derya Kapusuz  
Co-Supervisor, **Met. and Mat. Eng., Gaziantep University** \_\_\_\_\_

**Examining Committee Members:**

Prof. Dr. Zafer Evis  
Engineering Sciences, METU \_\_\_\_\_

Assoc. Prof. Dr. Batur Ercan  
Metallurgical and Materials Eng., METU \_\_\_\_\_

Assoc. Prof. Dr. Sedat Odabaş  
Chemistry, Ankara University \_\_\_\_\_

Assist. Prof. Dr. Simge Çınar  
Metallurgical and Materials Eng., METU \_\_\_\_\_

Assist. Prof. Dr. Eda Aydoğan  
Metallurgical and Materials Eng., METU \_\_\_\_\_

Date: 21.07.2020

**I hereby declare that all information in this document has been obtained and presented in accordance with academic rules and ethical conduct. I also declare that, as required by these rules and conduct, I have fully cited and referenced all material and results that are not original to this work.**

Name, Last name : Çağatay Mert Oral

Signature :

## ABSTRACT

### SYNTHESIS OF CALCIUM CARBONATE PARTICLES FOR BIOMEDICAL APPLICATIONS

Oral, Çağatay Mert

Master of Science, Metallurgical and Materials Engineering

Supervisor: Assoc. Prof. Dr. Batur Ercan

Co-Supervisor: Assist. Prof. Dr. Derya Kapusuz

July 2020, 80 pages

Calcium carbonate ( $\text{CaCO}_3$ ) particles have been widely used in biomedical applications owing to their biocompatibility and biodegradability. In order to effectively utilize  $\text{CaCO}_3$  particles in biomedical applications, their physical and chemical properties should be systematically controlled. However, this is a challenging task due to the presence of three different anhydrous  $\text{CaCO}_3$  polymorphs having complex crystallization behavior. In this thesis,  $\text{CaCO}_3$  particles were synthesized at distinct environments to control their properties. By altering temperature and ethylene glycol concentration of the precursor solutions, vaterite or aragonite content of the particles were maximized, while minimizing the average particle size. In addition, pH and  $[\text{Ca}^{2+}]:[\text{CO}_3^{2-}]$  ratio of the precursor solutions were adjusted to synthesize vaterite and calcite particles having distinct morphologies. By conducting control experiments, ethylene glycol concentration and solution pH were compared for their influence on  $\text{CaCO}_3$  particle properties. In order to assess the use of synthesized vaterite, aragonite and calcite particles in orthopedic applications, *in vitro* experiments were conducted using human bone cells. Moreover, an inert gas bubbling method was used to synthesize hollow  $\text{CaCO}_3$  microspheres for orthopedic

applications. Since requirements for the physical and chemical properties of CaCO<sub>3</sub> particles are diverse for each biomedical application, the findings of this thesis contributed to identify viable synthesis routes to obtain CaCO<sub>3</sub> particles with distinct properties.

Keywords: Calcium Carbonate, Biomaterials, Bioceramics, Orthopedics

## ÖZ

### BİYOMEDİKAL UYGULAMALAR İÇİN KALSİYUM KARBONAT PARÇACIKLARIN SENTEZİ

Oral, Çağatay Mert  
Yüksek Lisans, Metalurji ve Malzeme Mühendisliği  
Tez Yöneticisi: Doç. Dr. Batur Ercan  
Ortak Tez Yöneticisi: Dr. Öğr. Üyesi Derya Kapusuz

Temmuz 2020, 80 sayfa

Kalsiyum karbonat ( $\text{CaCO}_3$ ) parçacıklar, biyoyumluluk ve biyoçözünürlük özellikleri nedeniyle biyomedikal uygulamalarda yaygın olarak kullanılmaktadır.  $\text{CaCO}_3$  parçacıklardan biyomedikal uygulamalarda etkin olarak yararlanabilmek için, fiziksel ve kimyasal özelliklerin sistematik olarak kontrol edilmesi gerekmektedir. Ancak, bu amaç üç farklı susuz  $\text{CaCO}_3$  polimorfu bulunması ve polimorfların kompleks kristalizasyon davranışı nedeniyle zorlayıcıdır. Bu tezde,  $\text{CaCO}_3$  parçacıkların özelliklerini kontrol edebilmek için farklı ortamlar kullanılmıştır. Prekürsör solüsyonların sahip olduğu sıcaklık ve etilen glikol oranlarının değiştirilmesiyle birlikte, parçacıkların vaterit veya aragonit miktarları yükseltilmiş ve ortalama parçacık boyutu küçültülmüştür. Ek olarak, prekürsör solüsyonların pH ve  $[\text{Ca}^{2+}]:[\text{CO}_3^{2-}]$  oranları ayarlanarak, farklı morfolojilere sahip vaterit ve kalsit parçacıklar sentezlenmiştir. Kontrol deneyleriyle birlikte, etilen glikol kontrasyonu ve solüsyon pH değerinin  $\text{CaCO}_3$  parçacık özelliklerine olan etkisi karşılaştırılmıştır. Sentezlenen vaterit, aragonit ve kalsit parçacıkların ortopedi uygulamalarında kullanılmasını incelemek için, insan kemik hücreleri ile *in vitro* deneyler yürütülmüştür. Ayrıca, ortopedi uygulamalarına yönelik içi boş  $\text{CaCO}_3$

mikroküreler elde etmek için bir inert gaz yöntemi kullanılmıştır. Biyomedikal uygulamalar için gereken fiziksel ve kimyasal parçacık özelliklerinin çeşitli olması nedeniyle, bu tezdeki bulgular farklı özelliklere sahip  $\text{CaCO}_3$  parçacık elde edilebilmesi için güvenilir sentez yolları belirlenmesine katkı sağlamıştır.

Anahtar Kelimeler: Kalsiyum Karbonat, Biyomalzemeler, Biyoseramikler, Ortopedi

To my beloved parents

## ACKNOWLEDGEMENTS

I would like to express my sincere gratitude to my advisor Assoc. Prof. Dr. Batur Ercan for his support, guidance and patience. Starting from my undergraduate years, he has always shared his knowledge, experience and time without hesitation. I am thankful for the opportunity to conduct research with him.

I am also grateful to my co-advisor Assist. Prof. Dr. Derya Kapusuz for her support and guidance. In addition to having creative research ideas, her friendly attitude helped me to have a peaceful research environment.

I would like to acknowledge The Scientific and Technological Research Council of Turkey (117M754 and 118M652) and Middle East Technical University Research Funds (BAP-03-08-2016-009) for providing financial support. In addition, I am grateful to Center of Excellence in Biomaterials and Tissue Engineering for providing financial support to attend 2018 MRS Fall Meeting and 30<sup>th</sup> Annual Conference of the European Society for Biomaterials.

I am also thankful to the members of Biomaterials and Nanomedicine Laboratory for creating a peaceful research environment. I have special gratitude to Ece Uslu and Yiğithan Tufan for their friendship and Didem Mimirođlu for her help with cell culture experiments. In addition, I am grateful to Arda alıřkan and Yađmur Gcťu for being hardworking undergraduate researchers. I also would like to thank former labmates, Eyűp Can Demir, Merve Nur Dođu, Saba Najjarhagh and Merve İzmir, for their support and friendship.

I would like to acknowledge the members of Central Laboratory of Middle East Technical University, Center of Excellence in Biomaterials and Tissue Engineering and Department of Metallurgical and Materials Engineering, especially Gkhan Polat and Nilűfer zel for their help in XRD and Serkan Yılmaz for his help in SEM and TEM.

I have special thanks to Çađrı Özdilek and Merve Çobanođlu for their support and friendship throughout my undergraduate and graduate years.

Lastly, I want to express my profound gratitude to my mother and father for their unconditional support, patience and love to become who I am now. Every progress in my life is result of their belief in me.

## TABLE OF CONTENTS

ABSTRACT .....	v
ÖZ .....	vii
ACKNOWLEDGEMENTS .....	x
TABLE OF CONTENTS.....	xii
LIST OF TABLES.....	xiv
LIST OF FIGURES .....	xv
LIST OF ABBREVIATIONS .....	xix
CHAPTERS	
1 INTRODUCTION .....	1
1.1 Synthesis of CaCO <sub>3</sub> Particles.....	3
1.2 CaCO <sub>3</sub> Particles for Biomedical Applications.....	6
1.3 Research and Thesis Organization.....	7
2 EXPERIMENTAL METHODS .....	9
2.1 Materials .....	9
2.2 Particle Synthesis .....	9
2.3 Particle Characterization .....	11
2.3.1 Morphological Characterization.....	11
2.3.2 Polymorphic Characterization.....	12
2.3.3 Chemical Characterization.....	12
2.3.4 Internal Structure Analysis .....	13
2.3.5 Gas Adsorption Analysis .....	13
2.3.6 Particle Size Analysis .....	14

2.3.7	Cell Viability Assay .....	14
2.3.8	Statistical Analysis .....	15
3	ENHANCED VATERITE AND ARAGONITE CRYSTALLIZATION AT CONTROLLED ETHYLENE GLYCOL CONCENTRATIONS .....	17
3.1	Results and Discussion.....	17
4	INFLUENCE OF PH ON MORPHOLOGY, SIZE AND POLYMORPH OF ROOM TEMPERATURE SYNTHESIZED CaCO <sub>3</sub> PARTICLES .....	27
4.1	Results and Discussion.....	27
4.1.1	Effect of pH and [Ca <sup>2+</sup> ]:[CO <sub>3</sub> <sup>2-</sup> ] Ratio on CaCO <sub>3</sub> Particle Polymorph ...	27
4.1.2	Effect of pH and [Ca <sup>2+</sup> ]:[CO <sub>3</sub> <sup>2-</sup> ] Ratio on CaCO <sub>3</sub> Particle Size and Morphology .....	35
4.1.3	Comparison of pH and EG Ratio Effects on CaCO <sub>3</sub> Particle Properties	38
5	EFFECT OF POLYMORPHISM ON THE BIOCOMPATIBILITY OF CaCO <sub>3</sub> PARTICLES.....	43
5.1	Results and Discussion.....	44
6	SYNTHESIS OF CaCO <sub>3</sub> MICROSPHERES VIA INERT GAS BUBBLING FOR ORTHOPEDIC APPLICATIONS .....	51
6.1	Results and Discussion.....	53
6.1.1	Influence of Synthesis Parameters on CaCO <sub>3</sub> Polymorph and Morphology .....	53
6.1.2	Properties of CaCO <sub>3</sub> Microspheres .....	59
7	CONCLUSIONS AND FUTURE WORK.....	67
	REFERENCES .....	71

## LIST OF TABLES

### TABLES

<b>Table 6.1.</b> Physical properties of SC-P, SC-I, UL-A and FL-A particles. ....	58
--	----

## LIST OF FIGURES

### FIGURES

<b>Figure 1.1.</b> Crystallization pathways: A system may follow one-step route to the final mineral phase (pathway A) or proceed by sequential precipitation (pathway B) [15].....	2
<b>Figure 1.2.</b> Solubility product ( $K_{sp}$ ) of vaterite, aragonite, calcite and amorphous $\text{CaCO}_3$ at 1 bar [14]. .....	3
<b>Figure 1.3.</b> Typical morphologies of a) vaterite [21], b) aragonite [14] and c) calcite [21] particles.....	4
<b>Figure 1.4.</b> $\text{CaCO}_3$ particle synthesis methods: a) spontaneous precipitation, b) slow carbonation, c) reverse emulsion and d) $\text{CO}_2$ bubbling [19].....	5
<b>Figure 1.5.</b> Loading capacity of $\text{CaCO}_3$ particles having different morphologies and sizes. The capacity values were represented in $\mu\text{g}$ of dye per mg of the particles for the same total particle weight [45]. .....	7
<b>Figure 3.1.</b> XRD spectra of $\text{CaCO}_3$ particles synthesized at a) 25 °C and c) 70 °C. Weight percentages of vaterite and aragonite at b) 25 °C and d) 70 °C using different EG concentrations. Red lines are JCPDS references for vaterite, aragonite and calcite. ....	19
<b>Figure 3.2.</b> FTIR spectra of $\text{CaCO}_3$ particles synthesized using 0%, 20%, 40%, 60%, 80% and 90% EG at a) 25 °C and b) 70 °C. ‘V’, ‘A’ and ‘C’ denote peaks corresponding to vaterite, aragonite and calcite polymorphs, respectively. ....	20
<b>Figure 3.3.</b> SEM micrographs of $\text{CaCO}_3$ particles synthesized at 25 °C using a) 0%, b) 20%, c) 40%, d) 60%, e) 80% and f) 90% EG concentrations. Scale bars are 10 $\mu\text{m}$ . Insets show higher magnification micrographs of $\text{CaCO}_3$ particles and their scale bars are 1 $\mu\text{m}$ . ....	21
<b>Figure 3.4.</b> SEM micrographs of $\text{CaCO}_3$ particles synthesized at 70 °C using a) 0%, b) 20%, c) 40%, d) 60%, e) 80% and f) 90% EG concentrations. Scale bars are 10 $\mu\text{m}$ . Insets show higher magnification micrographs of $\text{CaCO}_3$ particles and their scale bars are 1 $\mu\text{m}$ . ....	23

**Figure 3.5.** Average size of CaCO<sub>3</sub> particles synthesized at 25 °C and 70 °C using different EG concentrations. Values are mean ± SEM, n=3. ....24

**Figure 4.1.** SEM micrographs of CaCO<sub>3</sub> particles synthesized at pH 8.0, 10.0, 11.0, 12.0 and 13.0 using 5 different [Ca<sup>2+</sup>]:[CO<sub>3</sub><sup>2-</sup>] ratios. Ellipsoidal, spherical and spheroidal vaterite particles transformed to rhombohedral, flower-like and irregular calcite particles with an increase in pH. Scale bars are 3 μm. ....29

**Figure 4.2.** XRD patterns of CaCO<sub>3</sub> particles synthesized at 5 different [Ca<sup>2+</sup>]:[CO<sub>3</sub><sup>2-</sup>] ratios at pH 8.0 and 13.0. Red, green, black, blue and purple lines indicate [5]:[1], [2]:[1], [1]:[1], [1]:[2] and [1]:[3] ratios, respectively. At pH 8.0, vaterite was the main CaCO<sub>3</sub> polymorph, while calcite was the main CaCO<sub>3</sub> polymorph at pH 13.0 for the investigated [Ca<sup>2+</sup>]:[CO<sub>3</sub><sup>2-</sup>] ratios. Gray lines are JCPDS references for vaterite (#033-0268) and calcite (#005-0586). ....30

**Figure 4.3.** Percentage of calcite polymorph at different pH values for different [Ca<sup>2+</sup>]:[CO<sub>3</sub><sup>2-</sup>] ratios. Red, black and purple lines denote [5]:[1], [1]:[1] and [1]:[3] ratios, respectively. Vaterite to calcite polymorphic transformation was observed with an increase in pH value of the precursor solutions. The transformation pH decreased with increasing [Ca<sup>2+</sup>]:[CO<sub>3</sub><sup>2-</sup>] ratio. ....32

**Figure 4.4.** FTIR spectra of CaCO<sub>3</sub> particles synthesized at 5 different [Ca<sup>2+</sup>]:[CO<sub>3</sub><sup>2-</sup>] ratios at pH 8.0 and 13.0. Red, green, black, blue and purple lines indicate [5]:[1], [2]:[1], [1]:[1], [1]:[2] and [1]:[3] [Ca<sup>2+</sup>]:[CO<sub>3</sub><sup>2-</sup>] ratios, respectively. ‘V’ and ‘C’ denote peaks corresponding to vaterite and calcite polymorphs. Both vaterite and calcite peaks were present at pH 8.0, while only calcite peaks were observed at pH 13.0. ....33

**Figure 4.5.** a) and b) vaterite (pH 8.0) and c) and d) calcite (pH 13.0) polymorphs synthesized at [1]:[2] [Ca<sup>2+</sup>]:[CO<sub>3</sub><sup>2-</sup>] ratio. a) and c) TEM and b) and d) HR-TEM micrographs. Insets show selected area diffraction patterns obtained from the particles. ....34

**Figure 4.6.** a) CaCO<sub>3</sub> particle size obtained at different pH values using 5 different [Ca<sup>2+</sup>]:[CO<sub>3</sub><sup>2-</sup>] ratios. Increase in particle size with an increase in precursor solution pH was observed. Values are mean ± SEM; n=5. b) Circularity index of CaCO<sub>3</sub>

particles synthesized at different pH values using 3 different  $[\text{Ca}^{2+}]:[\text{CO}_3^{2-}]$  ratios. Higher circularity indices were obtained for solutions having excess  $\text{Ca}^{2+}$  cations at lower pH values. Circularity indices of 1.0, 0.88 and 0.66 correspond to circle, square and ellipsoid particle morphology, respectively. Red, green, black, blue and purple lines indicate [5]:[1], [2]:[1], [1]:[1], [1]:[2] and [1]:[3]  $[\text{Ca}^{2+}]:[\text{CO}_3^{2-}]$  ratios, respectively..... 36

**Figure 4.7.** SEM micrographs of  $\text{CaCO}_3$  particles synthesized using [1]:[2]  $[\text{Ca}^{2+}]:[\text{CO}_3^{2-}]$  ratio a) with (top row) and b) without pH adjustment (bottom row). Particles on each column have the same EG concentration.  $\text{CaCO}_3$  particle morphology and polymorph differed upon changes in pH value. Scale bars are 3  $\mu\text{m}$ . ..... 39

**Figure 4.8.** a) XRD patterns of particles synthesized at pH 10.0, 11.0, 12.0 and 13.0 having [1]:[2]  $[\text{Ca}^{2+}]:[\text{CO}_3^{2-}]$  ratio (blue lines) and their corresponding control samples having the same EG concentration but without any pH adjustment (gray lines). Black lines are JCPDS references for vaterite (#033-0268) and calcite (#005-0586). b) FTIR spectra of the control samples. ‘V’ and ‘C’ denote peaks corresponding to vaterite and calcite, respectively. While pH-controlled samples exhibited vaterite to calcite transformation with an increase in pH, control samples did not show polymorph transformation. .... 40

**Figure 5.1.** SEM micrographs of a) ellipsoidal vaterite, b) bowknot-like aragonite and c) rhombohedral calcite particles synthesized at different conditions. Scale bars are 5  $\mu\text{m}$ . Inset shows high magnification SEM micrograph of bowknot-like aragonite particles and its scale bar is 1  $\mu\text{m}$ . ..... 44

**Figure 5.2.** XRD patterns of a) ellipsoidal vaterite, b) bowknot-like aragonite and c) rhombohedral calcite particles. Red lines are JCPDS references for vaterite (#033-0268), aragonite (#005-0453) and calcite (#005-0586). .... 46

**Figure 5.3.** FTIR spectra of a) ellipsoidal vaterite, b) bowknot-like aragonite and c) rhombohedral calcite particles. ‘V’, ‘A’ and ‘C’ denote peaks corresponding to vaterite, aragonite and calcite polymorphs, respectively. .... 47

**Figure 5.4.** Proliferation of hFOB cells exposed to a) ellipsoidal vaterite, b) bowknot-like aragonite and c) rhombohedral calcite particles at different concentrations up to 5 days of culture (Mean  $\pm$  SD, n = 3). Cells cultured without the particles were denoted as control. \*p < 0.01 and \*\*p < 0.001 compared to control group. #p < 0.001 compared to all groups. ....49

**Figure 6.1.** SEM micrographs of CaCO<sub>3</sub> particles prepared using a-d) 0% EG (25 °C), e-h) 0% EG (90 °C), i-l) 80% EG (25 °C) and m-p) 80% EG (90 °C) precursor solutions. a, e, i and m) have neither SDS nor N<sub>2</sub> bubbling, b, f, j and n) have SDS addition only, c, g, k and o) have N<sub>2</sub> bubbling only and d, h, l and p) have both SDS and N<sub>2</sub> bubbling. Platelet shaped spherical calcite (SC-P), irregular shaped spherical calcite (SC-I), flower-like aragonite (FL-A) and urchin-like aragonite (UL-A) particles are highlighted in the figure. Insets show higher magnification micrographs of the particles. Scale bars are 5  $\mu$ m and 1  $\mu$ m for lower and higher magnification micrographs, respectively. ....54

**Figure 6.2.** Surface morphologies of a) SC-P, b) SC-I, c) UL-A and d) FL-A particles. Scale bars are 1  $\mu$ m. ....56

**Figure 6.3.** a) XRD and b) FTIR spectra of SC-P, SC-I, UL-A and FL-A particles. Red lines are JCPDS references for aragonite (#005-0453) and calcite (#005-0586). ‘C’ and ‘A’ denote peaks corresponding to calcite and aragonite polymorphs, respectively. ....57

**Figure 6.4.** a, d and g) Bright-field TEM, b, e and h) SAED and c, f and i) HR-TEM micrographs of a, b and c) SC-P, d, e and f) SC-I and g, h and i) UL-A particles. .60

**Figure 6.5.** Nitrogen gas adsorption-desorption isotherms of a) SC-P, b) SC-I, c) UL-A and d) FL-A particles. Insets show pore size distribution of the particles....61

**Figure 6.6.** hFOB cell densities exposed to CaCO<sub>3</sub> particles at a) 0.01 mg/ml, b) 0.1 mg/ml and c) 1 mg/ml concentrations up to 5 days. Cells cultured without the particles were denoted as control. The results were represented as mean  $\pm$  SD. n = 3, \*p < 0.001. ....62

## LIST OF ABBREVIATIONS

### ABBREVIATIONS

<b>ATR</b>	Attenuated Total Reflection
<b>BET</b>	Branuer-Emmett-Teller
<b>BJH</b>	Barrett-Joyner-Halenda
<b>CaCO<sub>3</sub></b>	Calcium Carbonate
<b>CTAB</b>	Hexadecyl(trimethyl) Azanium Bromide
<b>DMEM</b>	Dulbecco's Modified Eagle's Medium
<b>DOX</b>	Doxorubicin
<b>EG</b>	Ethylene Glycol
<b>FIB</b>	Focused Ion Beam
<b>FL-A</b>	Flower-like Aragonite
<b>FTIR</b>	Fourier Transform Infrared Spectroscopy
<b>GSAS-II</b>	General Structure Analysis System II
<b>hFOB</b>	Human Bone Cells
<b>HR</b>	High Resolution
<b>MTT</b>	3-(4,5-dimethyl-2-thiazolyl)-2,5-diphenyl-2H-tetrazolium bromide
<b>N<sub>2</sub></b>	Nitrogen
<b>SAED</b>	Selected Area Electron Diffraction
<b>SBF</b>	Simulated Body Fluid
<b>SC-I</b>	Irregular Shaped Spherical Calcite
<b>SC-P</b>	Platelet Shaped Spherical Calcite

<b>SDS</b>	Sodium Dodecyl Sulfate
<b>SEM</b>	Scanning Electron Microscopy
<b>TEM</b>	Transmission Electron Microscopy
<b>UL-A</b>	Urchin-like Aragonite
<b>XRD</b>	X-ray Diffraction

## CHAPTER 1

### INTRODUCTION

Particulate systems with precisely engineered properties have been widely investigated for biomedical applications [1]. Though there are promising candidates for therapy, sensing and imaging applications, poor degradability and toxic by-product formation are the major drawbacks to attain optimum efficacy upon their implementation [2,3]. Therefore, particulate systems consisting of the naturally occurring ions in the human body have captured significant attention [2]. For instance, calcium is an ubiquitous element in the human body and it can exist in biominerals, *i.e.* calcium carbonate, calcium phosphate and calcium fluoride [2]. In addition to the critical roles of calcium in cellular and physiological processes, carbonate and phosphate groups can participate in the human metabolism [2,4].

Among different calcium-based forms, calcium carbonate ( $\text{CaCO}_3$ ) is the most abundant non-siliceous mineral in nature [5]. It is typically synthesized by living organisms, *i.e.* marine invertebrates, to build shells and exoskeletons for support and protection [6,7]. Over millions of years, these structures can accumulate by sedimentation to constitute 4% of the Earth's crust in various forms, *i.e.* limestone and chalk [8]. Due to its abundance in nature and suitable optical properties (white color and high refractive index),  $\text{CaCO}_3$  is used as a filler material for paint and paper industries [9]. In nature,  $\text{CaCO}_3$  exists in different crystalline (anhydrous and hydrous) and non-crystalline forms. Three different polymorphs, namely vaterite, aragonite and calcite, are the anhydrous crystalline forms of  $\text{CaCO}_3$  [10]. Monohydrocalcite ( $\text{CaCO}_3 \cdot \text{H}_2\text{O}$ ) and ikaite ( $\text{CaCO}_3 \cdot 6\text{H}_2\text{O}$ ) are the main hydrous crystalline forms of  $\text{CaCO}_3$ , with a recently discovered one, calcium carbonate hemihydrate ( $\text{CaCO}_3 \cdot \frac{1}{2}\text{H}_2\text{O}$ ) [8]. In addition,  $\text{CaCO}_3$  can also exist as a transient form, called as amorphous  $\text{CaCO}_3$  [10].

In both biogenic and abiotic systems, the anhydrous  $\text{CaCO}_3$  polymorphs are the most common forms, which are transformed from amorphous  $\text{CaCO}_3$  [11]. Since the anhydrous  $\text{CaCO}_3$  polymorphs have distinct solubilities in aqueous media, their order of precipitation during synthesis is dictated by the solubility differences. According to Ostwald-Lussac rule of stages, if a solution is supersaturated with more than one mineral, the initially formed mineral has the highest solubility, *i.e.* the lowest stability [12]. The initially obtained form of  $\text{CaCO}_3$  is amorphous, having  $\log K_{\text{solubility product}} (\log K_{\text{sp}})$  value of -6.400, and it can readily transform to the anhydrous polymorphs by following a sequential pathway (Figure 1.1) via dissolution and recrystallization reactions [13-15]. Among the anhydrous polymorphs, vaterite is the least stable polymorph ( $\log K_{\text{sp,vaterite}} = -7.913$ ), followed by aragonite ( $\log K_{\text{sp,aragonite}} = -8.360$ ), while calcite is the most stable one ( $\log K_{\text{sp,calcite}} = -8.475$ ) [16]. Although  $K_{\text{sp}}$  values are prone to changes with alterations in temperature (Figure 1.2), the higher solubility of vaterite and aragonite indicate the challenging nature of obtaining these polymorphs due to their unstable characteristic.

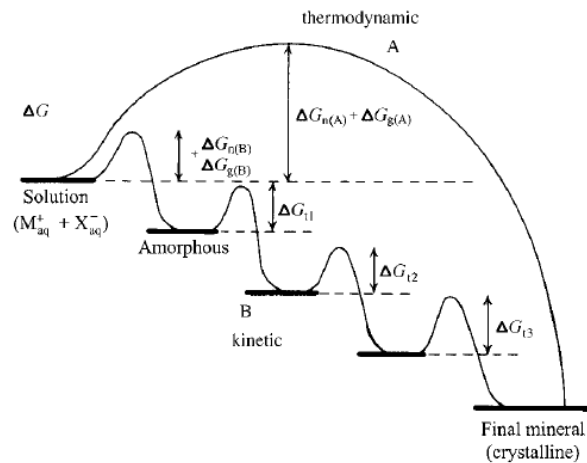


**Figure 1.1.** Crystallization pathways: A system may follow one-step route to the final mineral phase (pathway A) or proceed by sequential precipitation (pathway B) [15].

Though vaterite is the most unstable and calcite is the most stable anhydrous polymorphs of  $\text{CaCO}_3$ , aragonite has the highest hardness (3.5-4 in Mohs scale) and density ( $2.93 \text{ g/cm}^3$ ) values [17]. Furthermore, vaterite, aragonite and calcite polymorphs also have different crystal structures, hexagonal, orthorhombic and rhombohedral, respectively [18]. The difference in crystal structures leads to distinct particle morphologies for the anhydrous polymorphs (Figure 1.3), such as spherical (vaterite), needle-like (aragonite) and rhombohedral (calcite) [19].

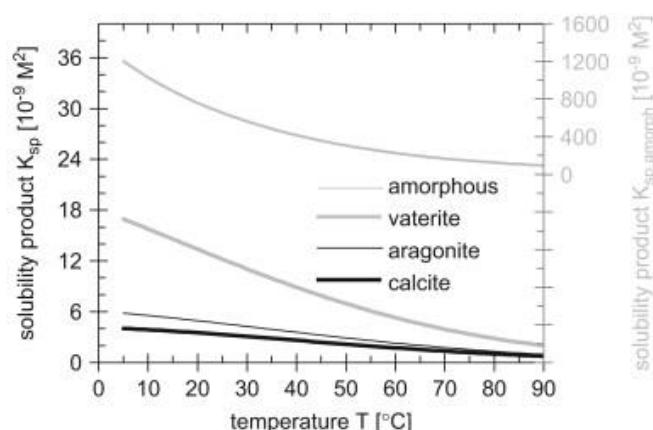


**Figure 1.2.** Solubility product ( $K_{sp}$ ) of vaterite, aragonite, calcite and amorphous  $\text{CaCO}_3$  at 1 bar [14].

### 1.1 Synthesis of $\text{CaCO}_3$ Particles

In addition to naturally occurring sources,  $\text{CaCO}_3$  particles having different physical and chemical characteristics can be fabricated synthetically [20]. There are two main methods to synthesize  $\text{CaCO}_3$  particles: biomimetic method (Figure 1.4a, b and c) and carbon dioxide ( $\text{CO}_2$ ) bubbling method (Figure 1.4d) [19]. Biomimetic method is divided into precipitation (Figure 1.4a and b) and reverse emulsion (Figure 1.4c) methods [19]. In addition, the precipitation method is further subdivided to spontaneous precipitation (Figure 1.4a) and slow carbonation (Figure 1.4b) methods [19]. In general, biomimetic method attempts to mimic nature's ability to form complex structures via dissolved materials under controlled environments [19]. On

the other hand, CO<sub>2</sub> bubbling is a more industrialized way to produce CaCO<sub>3</sub> particles by incorporation of CO<sub>2</sub> bubbles into Ca<sup>2+</sup> sources [19].

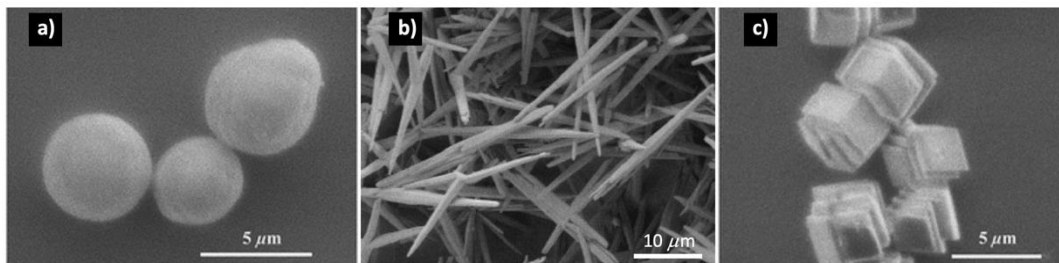


**Figure 1.3.** Typical morphologies of a) vaterite [21], b) aragonite [14] and c) calcite [21] particles.

Among different methods to synthetically obtain CaCO<sub>3</sub> particles, spontaneous precipitation method has captured significant attention due to the ease of particle precipitation with a wide range of properties [19]. In this method, solutions containing Ca<sup>2+</sup> cations and CO<sub>3</sub><sup>2-</sup> anions react inside a suitable aqueous environment at controlled conditions [17,22,23]. However, the polymorphic transformation of CaCO<sub>3</sub> particles makes it challenging to control their stability and require detailed investigations on the influence of several process parameters on the precipitation of particles [19]. In literature, there are several studies showing the influence of particle precipitation conditions, *i.e.* pH, supersaturation and temperature of the solution, solvent used to dissolve the precursors, precipitation time, stirring velocity, presence of additives on the properties of synthesized CaCO<sub>3</sub> particles [24-27]. By altering the precipitation conditions, researchers successfully synthesized spherical, ellipsoidal, flower-like, star-shaped, hexagon-shaped, rhombohedral, needle-like and dagger-like CaCO<sub>3</sub> particles [19,28-30]. For example, Chen *et al.* [31] synthesized rod-like aragonite and cake-like vaterite particles by changing the volume percentage of ethanol from 25% to 75%, respectively. In another study, rhombohedral calcite and ellipse-like vaterite particles were obtained at 90 °C by utilization of 0% and 50% ethylene glycol (EG), respectively [32]. Trushina *et al.* [21] controlled the synthesis temperature and successfully obtained rhombohedral

calcite (at 2-3 °C), spherical vaterite (at 25 °C) and star-like vaterite (at 40 °C) particles. In addition to these studies, different additives were utilized during synthesis of CaCO<sub>3</sub> particles to control their properties via altering the reaction conditions. For instance, Zhang *et al.* [33] focused on an alternate synthesis approach where they used 0.5 g/L Poly(sodium 4-styrenesulfate) to transform rhombohedral calcite to spherical vaterite inside deionized water without referring to the use of any solvents. In another study, hexadecyl(trimethyl) azanium bromide (CTAB) and sodium dodecyl sulfate (SDS) surfactants were added into the precursor solutions to transform vaterite into aragonite by altering CTAB/SDS ratio from 0 to 5 [34]. Similarly, Yan *et al.* [35] synthesized rod-like aragonite particles at 60 °C without incorporating any surfactants into the aqueous precursor solution, however flower-like vaterite particles were only crystallized upon the incorporation of Pluronic F127 and SDS surfactants inside the precursor solutions. Though these studies showed that CaCO<sub>3</sub> particles having distinct properties could be synthesized by altering the reaction conditions, more comprehensive studies were required to gain in-depth understanding on the effects of synthesis variables.

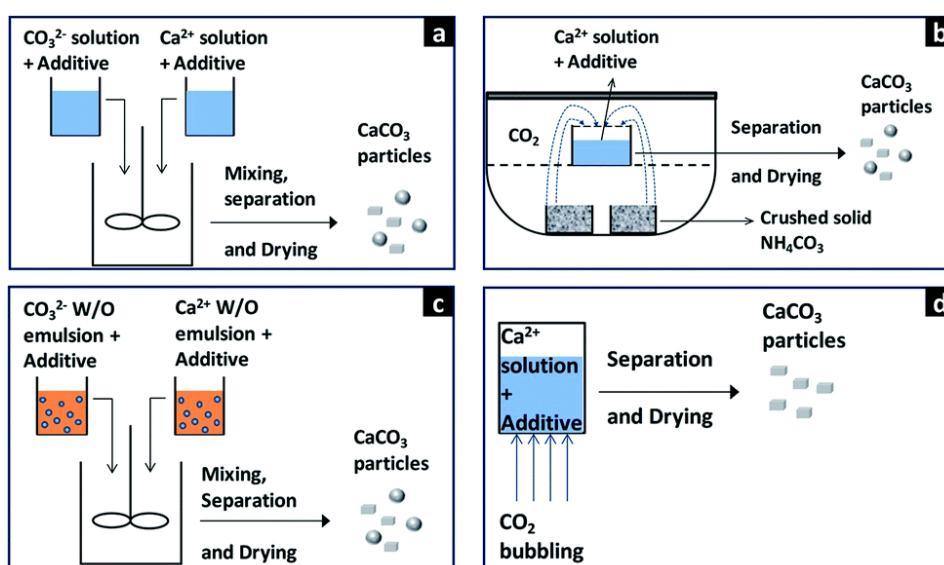


**Figure 1.4.** CaCO<sub>3</sub> particle synthesis methods: a) spontaneous precipitation, b) slow carbonation, c) reverse emulsion and d) CO<sub>2</sub> bubbling [19].

## 1.2 CaCO<sub>3</sub> Particles for Biomedical Applications

In literature, CaCO<sub>3</sub> particles were investigated for their efficacy in biomedical field, especially for orthopedic and drug delivery applications [36-39]. For instance, Tas [40] investigated the efficacy of using calcite particles to prepare biphasic (calcite and calcium phosphate) and macroporous bone cements for orthopedics. In another study, solely CaCO<sub>3</sub> particles (vaterite and amorphous CaCO<sub>3</sub>) were used as bone cements and they facilitated apatite-like crystal upon their immersion in simulated body fluid (SBF) [41]. Since CaCO<sub>3</sub> particles exhibited promising bioactive characteristics, they were also utilized as a coating on titanium surfaces [41,42]. By their utilization, hydroxyapatite layer formation enhanced without toxic effects *in vitro* [42].

Aside from orthopedic applications, drug delivery potential of CaCO<sub>3</sub> particles was also investigated. For example, Wei *et al.* [43] prepared hollow spherical vaterite particles to obtain a pH-sensitive platform to deliver anticancer drug doxorubicin (DOX). Though the particles were not toxic towards human liver cancer cells *in vitro*, cellular viability considerably decreased when the particles were loaded with DOX compared to free DOX [43]. Parakhonskiy *et al.* [44] investigated utilization of spherical vaterite particles and their polymorphic transformation to rhombohedral calcite for delayed burst-release of a payload and observed fast penetration of the CaCO<sub>3</sub> particles into human fibroblasts and ovarian carcinoma cells, while these particles did not exhibit any cytotoxicity. In another study, the same research group showed that morphology of CaCO<sub>3</sub> particles could alter drug delivery characteristics (Figure 1.5), where elliptical vaterite particles were shown to have a higher drug loading capacity compared to spherical vaterite particles [45]. Furthermore, it was observed that CaCO<sub>3</sub> particle size influenced loading capacity where smaller particles possessed higher loading capacity than large ones for the same total weight of CaCO<sub>3</sub> particles [45].

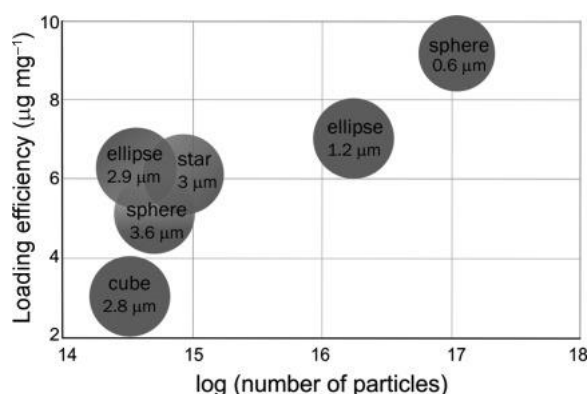


**Figure 1.5.** Loading capacity of CaCO<sub>3</sub> particles having different morphologies and sizes. The capacity values were represented in µg of dye per mg of the particles for the same total particle weight [45].

Clearly, altering the physical and chemical properties of CaCO<sub>3</sub> particles significantly influence the performance and final use of these particles. Thus, precisely controlled synthesis methods with a deeper understanding of CaCO<sub>3</sub> particle crystallization are required for biomedical applications.

### 1.3 Research and Thesis Organization

The main objectives of this thesis are:

1. Enhancing vaterite and aragonite content of the synthesized CaCO<sub>3</sub> particles.
2. Investigating the effects of solution pH on the properties of synthesized CaCO<sub>3</sub> particles.
3. Comparing the effects of solution pH and EG concentration on the synthesized CaCO<sub>3</sub> particles.
4. Investigating the effects of CaCO<sub>3</sub> polymorph in orthopedic applications.
5. Synthesis of aragonite and calcite microspheres via nitrogen (N<sub>2</sub>) bubbling approach for orthopedic applications.

The organization of the thesis is summarized as following:

The thesis consists of 7 chapters. In Chapter 1, CaCO<sub>3</sub> particles are introduced and the current studies on their synthesis and biomedical applications are exemplified. In Chapter 2, materials and methods used throughout the experiments are given. In Chapter 3, control on vaterite and aragonite content of the synthesized CaCO<sub>3</sub> particles, along with their morphology and size, are investigated by altering EG concentration and temperature of the precursor solutions. In Chapter 4, the effect of solution pH on polymorph, morphology and size of CaCO<sub>3</sub> particles is systematically characterized. In Chapter 5, vaterite, aragonite and calcite particles are compared in terms of their *in vitro* response towards human bone cells. In Chapter 6, a novel gas bubbling approach using N<sub>2</sub> is proposed to obtain porous/hollow aragonite and calcite microspheres for orthopedic applications. Finally, in Chapter 7, conclusions from the previous chapters are presented and recommendations for the future work are provided.

## CHAPTER 2

### EXPERIMENTAL METHODS

#### 2.1 Materials

Calcium acetate ( $\text{Ca}(\text{CH}_3\text{CO}_2)_2$ ), sodium bicarbonate ( $\text{NaHCO}_3$ ), SDS ( $\text{CH}_3(\text{CH}_2)_{11}\text{OSO}_3\text{Na}$ ), ethylene glycol (EG;  $(\text{CH}_2\text{OH})_2$ ) and ethanol ( $\text{C}_2\text{H}_5\text{OH}$ ) were purchased from Sigma Aldrich (St. Louis, Missouri) and used as received. Nitrogen ( $\text{N}_2$ ;  $\geq 99\%$ ) was obtained from Linde (Kocaeli, Turkey). Ultrapure water prepared with Millipore Milli-Q purification system (Burlington, Massachusetts) was used in all experiments.

#### 2.2 Particle Synthesis

In Chapter 3,  $\text{CaCO}_3$  particles were synthesized via the precipitation reaction between calcium acetate and sodium bicarbonate at 25 or 70 °C. For each temperature, 0-90% EG-containing aqueous solutions were prepared to investigate the effect of EG concentration on  $\text{CaCO}_3$  particle properties. In order to synthesize  $\text{CaCO}_3$  particles, aqueous calcium acetate (0.3 M) and sodium bicarbonate (0.9 M) precursor solutions were prepared separately, followed by incorporation of EG into each solution to obtain a total volume of 25 ml. Once the temperature of the solutions was stabilized at the desired value (25 or 70 °C), solutions were mixed quickly under magnetic agitation at 500 rpm for 15 minutes to initiate  $\text{CaCO}_3$  precipitation. Afterwards, the solution was kept at the same temperature for 1 hour without agitation. Then, the precipitate was washed using ethanol and ultrapure water, respectively. Lastly,  $\text{CaCO}_3$  particles were collected by centrifugation (7200 rpm, 15 minutes, 22 °C) and dried at 50 °C.

In Chapter 4, CaCO<sub>3</sub> particles were synthesized at room temperature (23 ± 1 °C). Briefly, calcium acetate and sodium bicarbonate were dissolved separately inside 4 ml ultrapure water at varying [Ca<sup>2+</sup>]:[CO<sub>3</sub><sup>2-</sup>] ratios ([5]:[1], [2]:[1], [1]:[1], [1]:[2], [1]:[3]), followed by the addition of 20 ml EG to each solution. The initial pH values of the solutions were adjusted to 8.0, 10.0, 11.0, 12.0 and 13.0 separately by using NaOH (1 M). Once pH values were adjusted, they were mixed with each other under magnetic agitation at 800 rpm for 15 minutes. Afterwards, precipitation of CaCO<sub>3</sub> particles was induced for 1 hour without magnetic stirring. CaCO<sub>3</sub> particles formed inside the solution were washed with ethanol and deionized water, respectively, collected by centrifugation (7200 rpm, 15 min, 22 °C) and dried overnight at 50 °C.

For the control experiments in Chapter 4, the same procedure was followed without pH adjustment. Since addition of NaOH (1 M) to adjust pH of the precursor solutions altered the EG concentration, control experiments were devised to distinguish the effects of precursor pH and EG concentration on the synthesized CaCO<sub>3</sub> particles. Briefly, volume of NaOH solution added into each precursor solution was measured and the same volume of ultrapure water (but no NaOH) were incorporated inside the precursor solutions for control experiments. Thus, similar EG concentrations were maintained, yet pH was not adjusted with NaOH (1 M).

In Chapter 5, CaCO<sub>3</sub> particles were synthesized at different [Ca<sup>2+</sup>]:[CO<sub>3</sub><sup>2-</sup>] molarity ratios using calcium acetate and sodium bicarbonate. [0.3]:[0.9] ratio was used to obtain ellipsoidal vaterite and bowknot-like aragonite, while [2.5]:[0.5] ratio was used to obtain rhombohedral calcite particles. The precursors were prepared separately, followed by addition of EG into each solution to obtain a total volume of 25 ml. For the synthesis of ellipsoidal vaterite particles, 90% EG-containing precursors were mixed at 70 °C. Similarly, 20% EG-containing precursors were mixed to synthesize bowknot-like aragonite particles at the identical temperature. To obtain rhombohedral calcite particles, the initial pH value of the 80% EG-containing precursors was adjusted to be 11 using NaOH (1 M) at 25 °C. After mixing the precursors for 15 minutes, the precipitated particles were aged for 1 hour at the

designated temperature, washed with ethanol and then ultra-pure water via centrifugation and dried at 50 °C.

In Chapter 6, CaCO<sub>3</sub> particles were precipitated at two different temperatures (25 °C and 90 °C) using 0% and 80% EG concentrations. Aqueous calcium acetate (0.3 M) and sodium bicarbonate (0.9 M) precursors were prepared separately and EG was added into these solutions to obtain a total volume of 25 mL for each solution. Afterwards, 0.576 g SDS was added into the sodium bicarbonate solution. While holding the temperature constant at 25 °C or 90 °C, N<sub>2</sub> bubbles were introduced (6 L/min) into the sodium bicarbonate solution, followed by incorporation of calcium acetate solution. After 15 minutes of N<sub>2</sub> bubbling, the solution was transferred to a fresh tube and aged for 4 hours at the designated temperature. To collect the precipitated CaCO<sub>3</sub> particles, the aged solution was centrifuged, followed by washing with ethanol and ultrapure water, respectively. The synthesized powder was dried at 50 °C.

To differentiate the effects of N<sub>2</sub> and SDS addition in Chapter 6, 4 different sets of CaCO<sub>3</sub> particles were synthesized using the identical protocol with minor changes. For the first set, neither SDS nor N<sub>2</sub> bubbling was introduced (referred as ‘No Addition’); for the second set, only SDS was introduced (referred as ‘SDS’), for the third set, only N<sub>2</sub> bubbling was performed (referred as ‘N<sub>2</sub> Bubble’) and for the last set, both SDS and N<sub>2</sub> bubbling were introduced (referred as ‘SDS and N<sub>2</sub> Bubble’). For the experiments without N<sub>2</sub> bubbling, the solutions were mixed under magnetic agitation at 500 rpm.

## **2.3 Particle Characterization**

### **2.3.1 Morphological Characterization**

FEI Nova NanoSEM 430 microscope (Brno, Czechia) was used to characterize CaCO<sub>3</sub> particle morphologies. 20 kV accelerating voltage was chosen to image the

surfaces. Prior to scanning electron microscope (SEM) characterization, Quorum SC7640 high-resolution sputter coater (East Sussex, United Kingdom) was used to coat a thin gold layer on CaCO<sub>3</sub> particles to create a conductive electrical path.

### 2.3.2 Polymorphic Characterization

In Chapter 3, 4 and 6, CaCO<sub>3</sub> polymorphs were identified using Rigaku D/Max-2200 X-ray diffractometer (Tokyo, Japan) with monochromatic Cu K<sub>α</sub> radiation ( $\lambda = 1.54 \text{ \AA}$ ) at 40 kV. Diffraction angles ( $2\theta$ ) from 20° to 60° were scanned at a scanning rate of 2°/min. Rietveld refinement analysis was also performed on the diffraction patterns of powders using GSAS-II software to calculate weight percentage of CaCO<sub>3</sub> polymorphs [46]. In Chapter 5, polymorph analysis was conducted using Bruker D8 Advance X-ray diffractometer (Karlsruhe, Germany) with monochromatic Cu K<sub>α</sub> ( $\lambda = 1.54 \text{ \AA}$ ) radiation at 40 kV. Diffraction angles ( $2\theta$ ) from 20° to 55° were scanned at a scanning rate of 2°/min.

In Chapter 6, average crystallite size of CaCO<sub>3</sub> particles was calculated using Scherrer equation ( $d = k \times \lambda / \beta \times \cos\theta$ ) where  $d$  represented average crystallite size,  $k$  was the shape factor,  $\lambda$  was the wavelength of the X-ray,  $\beta$  was the broadening at half maximum intensity and  $\theta$  was the diffraction angle. For crystallite size calculations, the most intense peaks of the X-ray Diffraction (XRD) scans ((104) plane at 29.4° for calcite particles and (111) plane at 26.2° for aragonite particles) were used.

### 2.3.3 Chemical Characterization

In Chapter 3 and 4, CaCO<sub>3</sub> particles were characterized using Perkin Elmer Spectrum 100 spectrometer (Waltham, Massachusetts) using attenuated total reflection (ATR) configuration. Samples were scanned in 1000-600 cm<sup>-1</sup> range with 4 cm<sup>-1</sup> resolution. In Chapter 5 and 6, Perkin Elmer 400 spectrometer (Waltham, Massachusetts) equipped with ATR configuration was used in 4000-400 cm<sup>-1</sup> range. The

background spectra were subtracted from the obtained reflectance. For Fourier transform infrared spectroscopy (FTIR) result of each sample, average of 4 spectra was reported.

#### **2.3.4 Internal Structure Analysis**

In Chapter 4, vaterite particles, synthesized at pH 10.0 using [1]:[2] ratio, were prepared for transmission electron microscopy (TEM) characterization by dispersing them ultrasonically in ethanol, followed by dropping 1 microliter of the dispersion onto lacey carbon-coated copper grids and air drying for 30 minutes. Calcite particles, synthesized at pH 13.0 using [1]:[2] ratio, were prepared for TEM characterization using FEI Nova NanoLab 600i focused ion beam (FIB) microscope (Brno, Czechia) at 30 kV acceleration voltage. Gallium ion source was used for milling at various beam currents ranging from 50 pA to 21 nA to prepare a thin calcite film. Prepared vaterite particles and FIB film of calcite particle were characterized in high-resolution (HR) and selected area electron diffraction (SAED) modes using JEOL JEM-2100F field-emission transmission electron microscope (Tokyo, Japan) at 200 kV accelerating voltage. SAED patterns were collected from a circular area approximately 0.12  $\mu\text{m}$  in diameter.

In Chapter 6, calcite and aragonite microspheres were prepared for TEM characterization by dispersing them ultrasonically in 2-propanol. 1  $\mu\text{l}$  of this solution was dropped onto holey carbon coated copper grid and dried for 5 minutes. Analysis was completed using bright-field, HR and SAED modes of FEI Tecnai G2 F30 TEM (Hillsboro, Oregon) at 200 kV accelerating voltage.

#### **2.3.5 Gas Adsorption Analysis**

Pore size and morphology of the  $\text{CaCO}_3$  particles were investigated by  $\text{N}_2$  gas adsorption using Quantachrome Autosorb 6B gas sorption analyzer (Boynton Beach, Florida). Prior to measurements, the particles were degassed at 70  $^\circ\text{C}$  for 6 hours.

Pore morphology, size and distribution of the particles were calculated based on the Barrett-Joyner-Halenda (BJH) model.

### **2.3.6 Particle Size Analysis**

In Chapter 3, ImageJ software was used to calculate average particle size from 30 particles for each sample. For size measurements, longest axis values of the predominant polymorph (vaterite or aragonite) were reported. In Chapter 4, size and circularity of CaCO<sub>3</sub> particles were measured using ImageJ software by analyzing 5 different micrographs from each sample group and measuring 50 different particles per image. In Chapter 5, size of the particles was measured using ImageJ software by analyzing 20 different particles for each sample group with 3 replicates.

In Chapter 6, size distribution of CaCO<sub>3</sub> particles was analyzed using Malvern Mastersizer 2000 particle size analyzer (Malvern, United Kingdom). Prior to the measurements, the particles were dispersed in ultrapure water for 10 minutes using an ultrasonicator. Average of 3 measurements was reported for each sample.

### **2.3.7 Cell Viability Assay**

In Chapter 5 and 6, human bone cells (hFOB, ATCC CRL-11372) were used to evaluate the effect of CaCO<sub>3</sub> particles on cell density and viability. hFOB cells were seeded onto 96-well plate at a density of 30,000 cells/cm<sup>2</sup> and incubated using Dulbecco's Modified Eagle's Medium (DMEM, Sigma Aldrich) supplemented with 10% fetal bovine serum, 1% penicillin-streptomycin and 1% L-glutamine for 24 h in a humidified incubator (5% CO<sub>2</sub>, 37 °C). Prior to cell culture experiments, the particles were sterilized with 70% ethanol and UV radiation. Afterwards, CaCO<sub>3</sub> particles were dispersed in DMEM at different concentrations (0.01, 0.1 and 1 mg/mL) and hFOB cells were exposed to these media up to 5 days. hFOB cells cultured using the same conditions without incorporation of CaCO<sub>3</sub> particles were used as control. At 2<sup>nd</sup> and 4<sup>th</sup> days of culture, media were replaced with freshly

prepared ones containing the designated concentration of CaCO<sub>3</sub> particles. At 1, 3 and 5 days of culture, media were aspirated, and the cells were washed with 1x PBS. Sterile 125 µl 3-(4,5-dimethyl-2-thiazolyl)-2,5-diphenyl-2H-tetrazolium bromide (MTT, Sigma Aldrich) was added onto each well at 1 mg/mL concentration to assess cellular viability. After incubating 4 hours at 37 °C, insoluble formazan crystals were dissolved with the addition of 125 µl isopropyl alcohol containing 0.77% HCl. Finally, absorbance of each well was measured at 570 nm using Thermo Scientific Multiskan Go microplate spectrophotometer (Waltham, Massachusetts). The absorbance value of blank samples without cells were subtracted from the measured values. In Chapter 6, cell densities were calculated by comparing the absorbance values to a standard curve constructed at the beginning of each trial.

### **2.3.8 Statistical Analysis**

In Chapter 5 and 6, *in vitro* experiments were performed in triplicate and the results were represented as mean ± SD. Statistical analyses were performed with one-way analysis of variance (ANOVA) using Tukey's post-hoc test with significance based on  $p < 0.05$ .



## CHAPTER 3

### ENHANCED VATERITE AND ARAGONITE CRYSTALLIZATION AT CONTROLLED ETHYLENE GLYCOL CONCENTRATIONS

In literature, most of the studies reported incorporation of surfactants or high synthesis temperatures to stabilize vaterite and aragonite particles. However, the use of EG as a precursor solvent to control stability of CaCO<sub>3</sub> particles might be an alternative approach [21,29]. EG is a non-aqueous polar solvent and miscible in water at all proportions [21,47]. Since water increases the solubility of metastable polymorphs and favor formation of calcite, using EG (instead of water) can limit formation of calcite. In fact, EG-based precursors were reported for the synthesis of different CaCO<sub>3</sub> morphologies [48,49]. However, systematic changes of precursor EG concentration at multiple temperatures and correlating the associated structural changes of CaCO<sub>3</sub> particles were not studied in detail. Herein, a simple processing route to decrease the solubility of vaterite and aragonite through the use of EG was presented. The processing route can serve as a simple alternative to control the formation of CaCO<sub>3</sub> particles with various morphologies and sizes, potentially offering ideal candidates for drug delivery and orthopedic applications.

#### 3.1 Results and Discussion

The XRD patterns of CaCO<sub>3</sub> particles synthesized using different concentrations of EG at 25 °C were shown in Figure 3.1a. In the spectra, all peaks could be indexed to vaterite (JCPDS: #033-0268) or calcite (JCPDS: #005-0586) polymorphs. In each sample, vaterite peaks at 24.92°, 26.99° and 32.78° corresponding to (110), (112) and (114) crystallographic planes, and/or calcite peaks at 29.40°, 35.90° and 39.50° corresponding to (104), (110) and (113) crystallographic planes were observed at varying intensities [50]. The variation of polymorph content in the synthesized

CaCO<sub>3</sub> particles with respect to the EG concentration is calculated by Rietveld refinement of XRD patterns given in Figure 3.1a. As shown in Figure 3.1b, in the absence of EG in the precursor solution (ultrapure water), CaCO<sub>3</sub> particles were composed of 50 wt% calcite and 50 wt% vaterite. As EG concentration of the precursor solutions gradually increased, vaterite fraction of the synthesized powder increased, reaching a maximum value at 60% EG. As mentioned previously, calcite is the most stable form of CaCO<sub>3</sub> at ambient conditions and synthesis of vaterite or aragonite without forming calcite is challenging [51]. However, almost phase-pure vaterite (98 wt%) was obtained in this study by incorporating 60% EG into the aqueous precursor solutions. Having this said, when the synthesis temperature increased to 70 °C, aragonite particles (JCPDS: #005-0453) along with calcite and vaterite particles formed. XRD patterns of CaCO<sub>3</sub> particles synthesized using different concentrations of EG at 70 °C were displayed in Figure 3.1c. Characteristic peaks of aragonite at 26.3° and 45.9° corresponding to (111) and (221) crystallographic planes and calcite peaks at 29.40°, 35.90° and 39.50° corresponding to (104), (110) and (113) crystallographic planes were observed, respectively [17]. As shown in the Rietveld refinement results (Figure 3.1d) of the XRD patterns given in Figure 3.1c, incorporation of EG into the precursor solutions favored formation of metastable CaCO<sub>3</sub> polymorphs (vaterite and aragonite) rather than calcite. In the absence of EG in the precursor solution, CaCO<sub>3</sub> particles consisted of 51 wt% calcite and 48 wt% aragonite. Upon the incorporation of 20% EG into the precursor solutions, vaterite/aragonite to calcite transformation was suppressed. At this EG concentration, particles contained 4 wt% vaterite, 75 wt% aragonite and 21 wt% calcite. As EG concentration increased further, the aragonite and vaterite content of the synthesized particles significantly altered. Up to 60% EG, aragonite formation dominated over vaterite, whereas after 70% EG, vaterite content maximized. These results indicated 60-70% EG concentration range to be critical in determining the degree of vaterite to aragonite transformation at a moderate synthesis temperature.

XRD findings were in agreement with previously published studies on CaCO<sub>3</sub> synthesis [21,52]. As previous studies suggested, incorporation of EG into the

precursor solutions provided hydroxyl groups (-OH) for the system. These hydroxyl groups possessed high cohesive energy and attracted oppositely charged  $\text{Ca}^{2+}$  cations [21,52]. The adsorption of hydroxyl groups changed the surface free energy of vaterite, leading to higher thermodynamic stability, and thus, vaterite dissolution was prevented [52,53]. In fact, the efficiency for suppression of calcite crystallization depended on the amount of -OH groups supplied by EG incorporation into the precursor solutions.

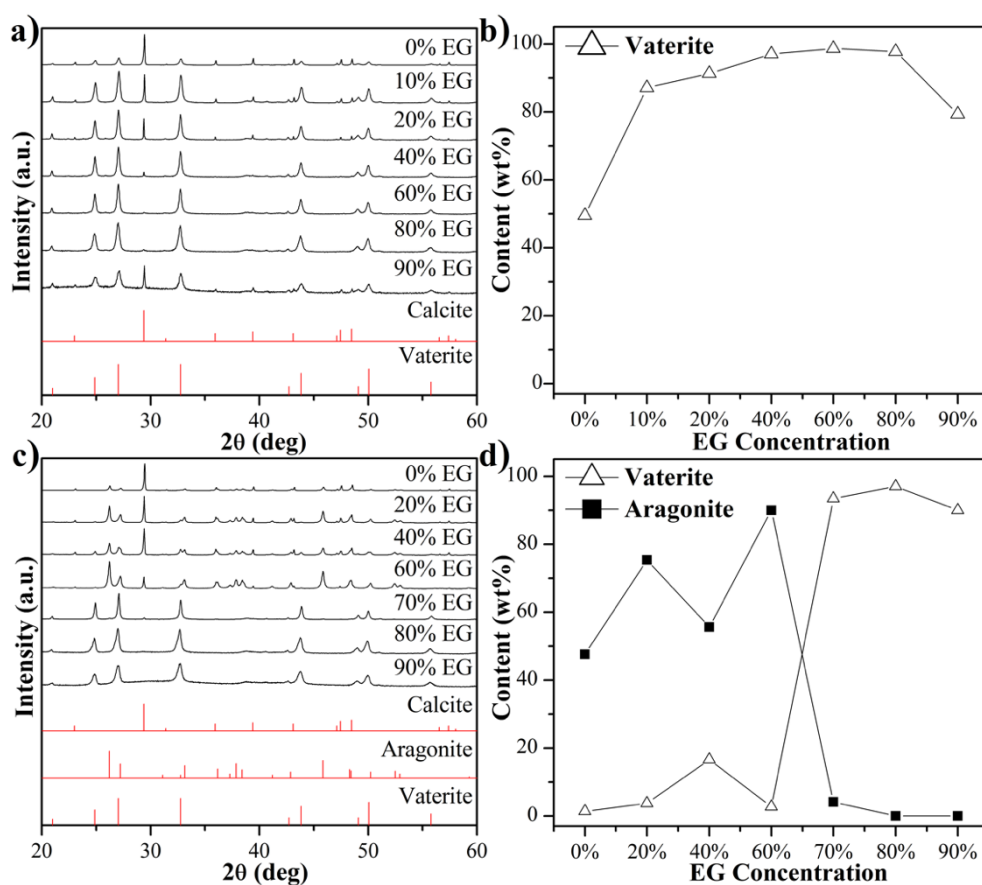


**Figure 3.1.** XRD spectra of  $\text{CaCO}_3$  particles synthesized at a) 25 °C and c) 70 °C. Weight percentages of vaterite and aragonite at b) 25 °C and d) 70 °C using different EG concentrations. Red lines are JCPDS references for vaterite, aragonite and calcite.

Aragonite particles, on the other hand, required extra energy to crystallize, which was typically provided via increasing the synthesis temperature. For instance, Flaten *et al.* [52] were able to synthesize aragonite particles (up to 76 wt%) at 80 °C, whereas repeating the same procedure at room temperature failed to obtain aragonite. In another study, Chen *et al.* [32] increased solution temperature during nucleation stage by microwave power and synthesized bundle-shaped aragonite particles at 90 °C. Similarly, in this study, almost phase-pure vaterite particles synthesized at 25 °C using high EG concentrations, yet aragonite particles could not be formed at this temperature independent of the presence or absence of EG. Along the same line, it can be speculated that incorporation of EG limited dissolution of vaterite to form aragonite and stabilized this polymorph despite the higher synthesis temperature, indicating its dominating efficacy at higher concentrations. It is clear that changing the amount of -OH group supply to the precursor solution via altering the precursor solvent type can provide potential stabilization routes for each CaCO<sub>3</sub> polymorph at temperatures ≤ 70 °C.

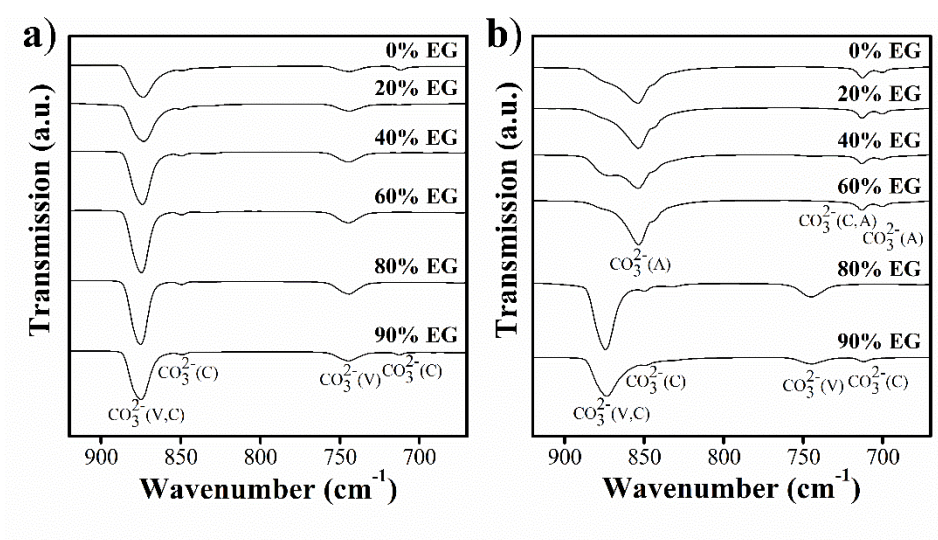


**Figure 3.2.** FTIR spectra of CaCO<sub>3</sub> particles synthesized using 0%, 20%, 40%, 60%, 80% and 90% EG at a) 25 °C and b) 70 °C. ‘V’, ‘A’ and ‘C’ denote peaks corresponding to vaterite, aragonite and calcite polymorphs, respectively.

In addition to XRD, FTIR was also used to characterize the  $\text{CaCO}_3$  polymorphs. Particles synthesized at 25 °C (Figure 3.2a) showed absorption bands of vaterite at 877 and 744  $\text{cm}^{-1}$  and calcite at 876, 848 and 714  $\text{cm}^{-1}$ , whereas particles synthesized at 70 °C (Figure 3.2b) showed additional aragonite absorption bands at 854, 712 and 700  $\text{cm}^{-1}$  [54,55]. These results were consistent with XRD results given in Figure 3.1, where vaterite and aragonite polymorphs were observed at different amounts depending on the EG concentration and synthesis temperature. FTIR confirmed formation of almost phase-pure vaterite using 60% EG at 25 °C and predominant formation of aragonite at EG concentration below 70% at 70 °C. Additionally, absorption bands of EG at 725  $\text{cm}^{-1}$  (C-H) and 885  $\text{cm}^{-1}$  (C-C) were not evident in any of the FTIR spectra, indicating complete removal of adsorbed EG from the precipitated  $\text{CaCO}_3$  particles [56].

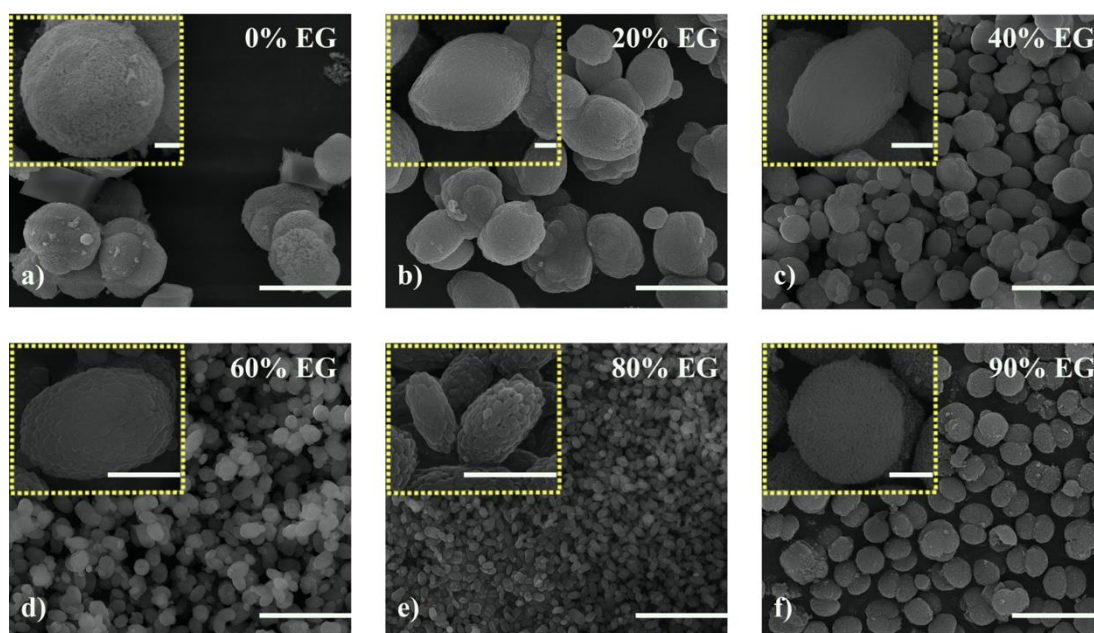


**Figure 3.3.** SEM micrographs of  $\text{CaCO}_3$  particles synthesized at 25 °C using a) 0%, b) 20%, c) 40%, d) 60%, e) 80% and f) 90% EG concentrations. Scale bars are 10 μm. Insets show higher magnification micrographs of  $\text{CaCO}_3$  particles and their scale bars are 1 μm.

In order to investigate the effect of EG incorporation on the particle size and morphology, synthesized  $\text{CaCO}_3$  particles were visualized using SEM. Figure 3.3 showed SEM micrographs of the particles obtained at 25 °C using various EG concentrations (0-90%). In literature, vaterite polymorph typically obtained in ellipsoidal or spherical, calcite polymorph typically obtained in rhombohedral and aragonite polymorph typically obtained in needle-like morphologies [19]. SEM micrographs of vaterite particles shown in Figure 3.3 were in-line with these findings. At the two extreme EG concentrations (0% and 90% EG), vaterite crystals exhibited spherical growth, whereas at intermediate concentrations, they grew in ellipsoidal and spheroidal morphologies. Considering that the sphere morphology is the lowest surface energy form of particles synthesized in solutions, ellipsoidal vaterite particles possessed higher surface free energy at intermediate EG concentrations. It can be speculated that as vaterite dissolution was inhibited by -OH groups of EG, highly viscous nature of EG limited migration of anions from the solution towards the surface, delaying growth of vaterite nuclei, and thus forming individual vaterite particles formed by the attachment of much smaller vaterite crystals (*i.e.* Figure 3.3e inset) [56]. These results also suggest that there might be a competition between the oriented attachment of small crystals on their highest energy planes, leading to growth into ellipsoidal particles (*i.e.* Figure 3.3e inset), along with dissolution and attachment of small nucleates uniformly across the particle to obtain a more spheroidal morphology (*i.e.* Figure 3.3 b, c, d inset) [22]. In addition, particles synthesized at 0% EG had the highest average particle size ( $8.09 \pm 1.64 \mu\text{m}$ ) at 25 °C as shown in Figure 3.5. Incorporation of more EG into the precursor solutions decreased average particle size, reaching its minimum ( $0.92 \pm 0.17 \mu\text{m}$ ) at 80% EG. Parakhonskiy *et al.* [57] also observed a similar trend in their study and obtained minimum vaterite particle sizes using 83% EG compared to 0% (pure water), 17% and 50% EG concentrations.

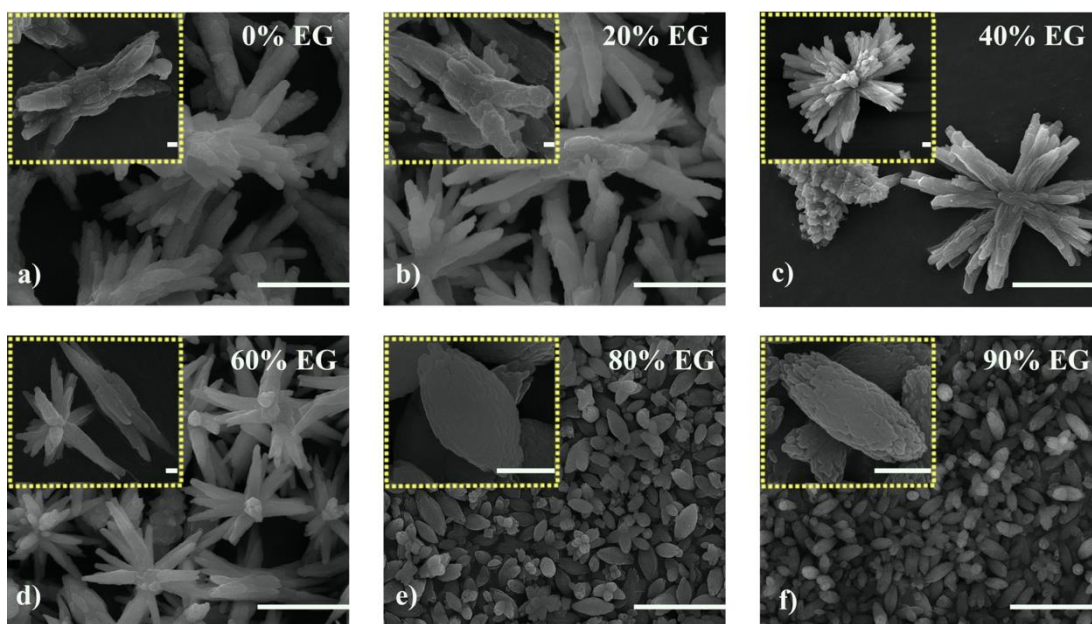


**Figure 3.4.** SEM micrographs of  $\text{CaCO}_3$  particles synthesized at  $70\text{ }^\circ\text{C}$  using a) 0%, b) 20%, c) 40%, d) 60%, e) 80% and f) 90% EG concentrations. Scale bars are  $10\text{ }\mu\text{m}$ . Insets show higher magnification micrographs of  $\text{CaCO}_3$  particles and their scale bars are  $1\text{ }\mu\text{m}$ .

At  $70\text{ }^\circ\text{C}$  (Figure 3.4), crab-like aragonite particles crystallized at concentrations below 60% EG. The attachment of aragonite needles to each other, most probably on the same crystallographic plane, leading to crab-like morphology observed at each EG concentration below 60%. Similar to growth of vaterite, the underlying reason for the attachment of needles to obtain a crab-like morphology was to decrease the surface energy via growing around their highest energy crystallographic planes. For  $\text{CaCO}_3$  particles synthesized at  $70\text{ }^\circ\text{C}$ , the effect of EG concentration on average particle size was more remarkable due to the polymorphic transformation and the morphological change. Figure 3.5 showed the highest average particle size ( $20.60 \pm 2.11\text{ }\mu\text{m}$ ) at 0% EG for particles synthesized at  $70\text{ }^\circ\text{C}$ , while this value decreased with increasing EG concentrations, reaching its minimum ( $1.92 \pm 0.52\text{ }\mu\text{m}$ ) at 80% EG.

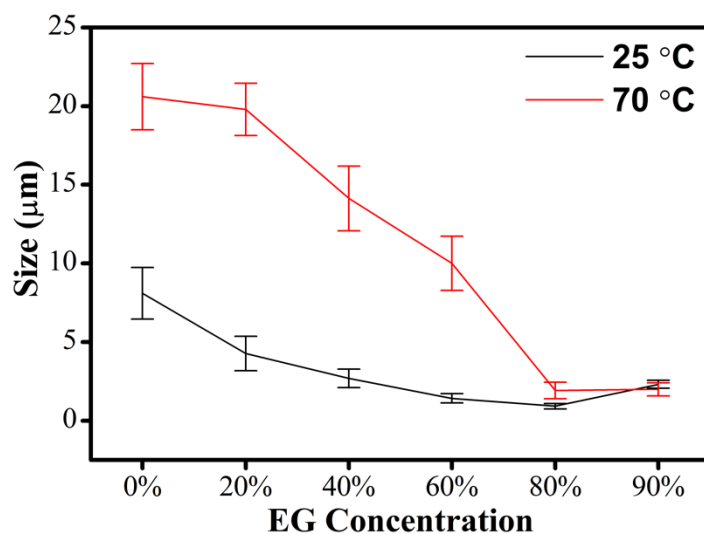


**Figure 3.5.** Average size of CaCO<sub>3</sub> particles synthesized at 25 °C and 70 °C using different EG concentrations. Values are mean ± SEM, n=3.

In this study, the effects of EG incorporation and temperature on the polymorph, morphology and size of CaCO<sub>3</sub> particles were investigated. Findings can be summarized under two main titles:

1 – Stabilization (inhibition of dissolution) of the CaCO<sub>3</sub> polymorphs under certain conditions:

To stabilize a CaCO<sub>3</sub> polymorph, one of the key parameters is decreasing its solubility in the mixed precursor solution. Among four main forms of CaCO<sub>3</sub>, amorphous CaCO<sub>3</sub> has the highest solubility leading to its rapid formation and dissolution during the initial stages of precursor solution mixing. Once amorphous CaCO<sub>3</sub> dissolves, ions recrystallize into vaterite, which is the least stable among the anhydrous forms of CaCO<sub>3</sub> (vaterite, aragonite, calcite) [14]. The inhibition of dissolution and calcite crystallization by changing the number of available ions in solution is the key approach to stabilize vaterite and/or aragonite. This study suggested that -OH groups in EG can bind polymorph ions, therefore alter supersaturation and lead to stabilization of unstable CaCO<sub>3</sub> polymorphs [53].

## 2 – Morphology and size of the precipitated polymorphs:

Results revealed that 60% EG as the optimum concentration to synthesize phase-pure vaterite at 25 °C and aragonite at 70 °C. At 25 °C, spheroidal (20-60% EG), ellipsoidal (80% EG) and spherical (0% and 90% EG) vaterite particles were observed. As temperature increased to 70 °C, crab-like aragonite particles (0-60% EG) in addition to spheroidal (80% EG) and ellipsoidal (90% EG) vaterite particles were obtained. At both temperatures, average particle size was highest at 0% EG, *i.e.*  $8.09 \pm 1.64 \mu\text{m}$  at 25 °C and  $20.60 \pm 2.11 \mu\text{m}$  at 70 °C, whereas these values decreased with increasing EG concentration and minimum values were obtained at 80% EG,  $0.92 \pm 0.17 \mu\text{m}$  at 25 °C and  $1.92 \pm 0.52 \mu\text{m}$  at 70 °C. Though the determination of growth behavior necessitated detailed HR-TEM analysis, it could be speculated that with increasing EG concentration, particles nucleated and stabilized at smaller sizes, and then grew by oriented attachment depending on the limits imposed by the presence (inhibition of dissolution) and the motion (high viscosity) of the free ions in the solution [22].

This study presents a road map to limit and control the extend of vaterite/aragonite to calcite transformation at lower temperatures without using surfactants or complex synthesis procedures reported in literature. According to the results, EG concentration and temperature of the precursor solutions may be used as experimental variables for precisely controlling polymorph, morphology and size of the synthesized  $\text{CaCO}_3$  particles to maximize efficacy of these particles in biomedical applications.



## CHAPTER 4

### INFLUENCE OF PH ON MORPHOLOGY, SIZE AND POLYMORPH OF ROOM TEMPERATURE SYNTHESIZED CaCO<sub>3</sub> PARTICLES

Though there are numerous studies on the synthesis of vaterite and calcite particles, there is still a gap in knowledge regarding the influence of pH on the polymorph, morphology and size of CaCO<sub>3</sub> particles obtained via room temperature spontaneous precipitation method due in part to the unstability of vaterite polymorph at ambient conditions [50,58,59]. In this study, the influence of initial pH and [Ca<sup>2+</sup>]:[CO<sub>3</sub><sup>2-</sup>] ratio of the precursor solutions on morphology, size and polymorph of CaCO<sub>3</sub> particles was investigated at room temperature without referring to the use of any surfactants. Having this said, in literature, incorporation of EG into the precursor solutions was utilized as an alternative method to adjust CaCO<sub>3</sub> particle properties [32]. In order to assess the influence of solution pH alone, control experiments were performed where EG concentration of the precursor solutions was kept constant. With these experiments, the effects of solution pH and EG concentration on CaCO<sub>3</sub> particle properties were distinguished.

#### 4.1 Results and Discussion

##### 4.1.1 Effect of pH and [Ca<sup>2+</sup>]:[CO<sub>3</sub><sup>2-</sup>] Ratio on CaCO<sub>3</sub> Particle Polymorph

CaCO<sub>3</sub> polymorphs synthesized by spontaneous precipitation method were visualized using SEM (Figure 4.1), where micrographs showed characteristic particle morphologies for anhydrous CaCO<sub>3</sub> polymorphs, namely vaterite and calcite. At pH 8.0 and 10.0, vaterite particles formed independent of the [Ca<sup>2+</sup>]:[CO<sub>3</sub><sup>2-</sup>] ratio used in this study. Once pH of the precursor solutions increased,

particles underwent polymorphic transformation from vaterite to calcite depending both on the pH values and the  $[\text{Ca}^{2+}]:[\text{CO}_3^{2-}]$  ratios. XRD (Figure 4.2) and Rietveld refinement analysis (Figure 4.3) on  $\text{CaCO}_3$  particles were completed to assess  $\text{CaCO}_3$  particle polymorphs. XRD spectra showed characteristic peaks of vaterite at  $24.92^\circ$ ,  $26.99^\circ$  and  $32.78^\circ$  corresponding to (110), (112) and (114) crystallographic planes and calcite at  $29.40^\circ$ ,  $35.90^\circ$  and  $39.50^\circ$  corresponding to crystallographic planes of (104), (110) and (113), respectively [50]. XRD analysis showed that vaterite was the major polymorph with minor amounts of calcite for all investigated  $[\text{Ca}^{2+}]:[\text{CO}_3^{2-}]$  ratios at pH 8.0. Presence of calcite as a minor polymorph for  $\text{CaCO}_3$  particles synthesized via spontaneous precipitation method was an expected finding due to the unstable nature of vaterite at ambient conditions, demonstrating the ease of transformation from vaterite to calcite [51]. Non-uniformity in supersaturation during solution-based  $\text{CaCO}_3$  synthesis has been offered to be one of the reasons behind this phenomenon [30]. When pH of the precursor solutions increased to 13.0, diffraction peaks of vaterite polymorph disappeared and calcite became the  $\text{CaCO}_3$  polymorph. Only for the sample having [5]:[1]  $[\text{Ca}^{2+}]:[\text{CO}_3^{2-}]$  ratio, in addition to calcite peaks, calcium hydroxide ( $\text{Ca}(\text{OH})_2$ ) peaks were also observed. Formation of  $\text{Ca}(\text{OH})_2$  was the result of excess  $\text{Ca}^{2+}$  and  $\text{OH}^-$  in the system since [5]:[1]  $[\text{Ca}^{2+}]:[\text{CO}_3^{2-}]$  sample had the highest  $\text{Ca}^{2+}$  cation concentration among all the samples and required incorporation of a large amounts of NaOH solution to adjust its pH to 13.0. Obtaining  $\text{Ca}(\text{OH})_2$  crystals along with calcite polymorph was consistent with the findings of Konno *et al.* [60] where transformation of calcite to  $\text{Ca}(\text{OH})_2$  was induced using NaOH solvent solution.

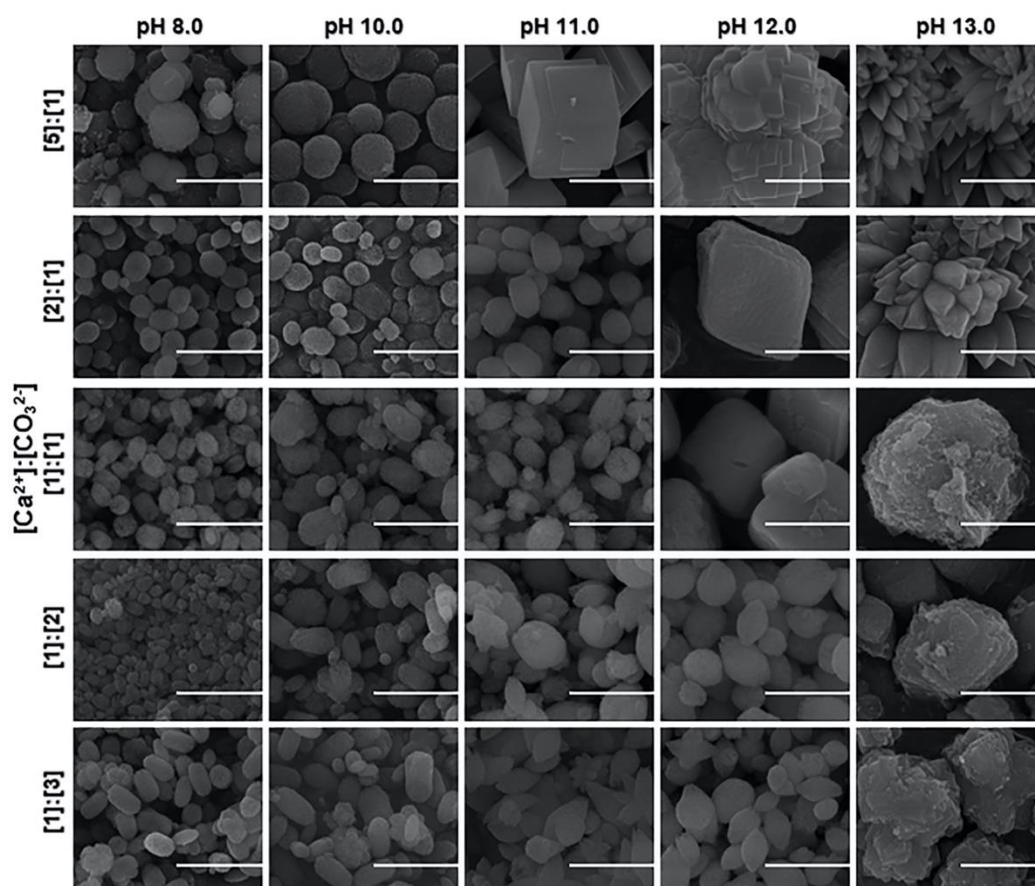


**Figure 4.1.** SEM micrographs of  $\text{CaCO}_3$  particles synthesized at pH 8.0, 10.0, 11.0, 12.0 and 13.0 using 5 different  $[\text{Ca}^{2+}]:[\text{CO}_3^{2-}]$  ratios. Ellipsoidal, spherical and spheroidal vaterite particles transformed to rhombohedral, flower-like and irregular calcite particles with an increase in pH. Scale bars are 3  $\mu\text{m}$ .

A detailed quantification of vaterite and calcite content of each sample was performed using Rietveld refinement analysis (Figure 4.3). Results showed that calcite weight percent was limited to 10-15% at pH 8.0 and 10.0, the rest being vaterite. However, when pH values of the precursor solutions increased, vaterite polymorph transformed to calcite polymorph at different pH values depending on their  $[\text{Ca}^{2+}]:[\text{CO}_3^{2-}]$  ratios. Vaterite to calcite transformation occurred at lower pH values as  $[\text{Ca}^{2+}]:[\text{CO}_3^{2-}]$  ratio increased, which was also evident in SEM micrographs (Figure 4.1). For samples having [1]:[3], [1]:[1] and [5]:[1]  $[\text{Ca}^{2+}]:[\text{CO}_3^{2-}]$  ratio, vaterite to calcite transformation took place at pH 12-13, pH 11-12 and pH 10-11,

respectively. Alteration in the polymorphic transformations with changes in ionic concentration was in agreement with previous studies. For instance, Han *et al.* [61] observed that excess  $\text{Ca}^{2+}$  cations in the solution favored transformation from spherical vaterite to rhombohedral calcite.

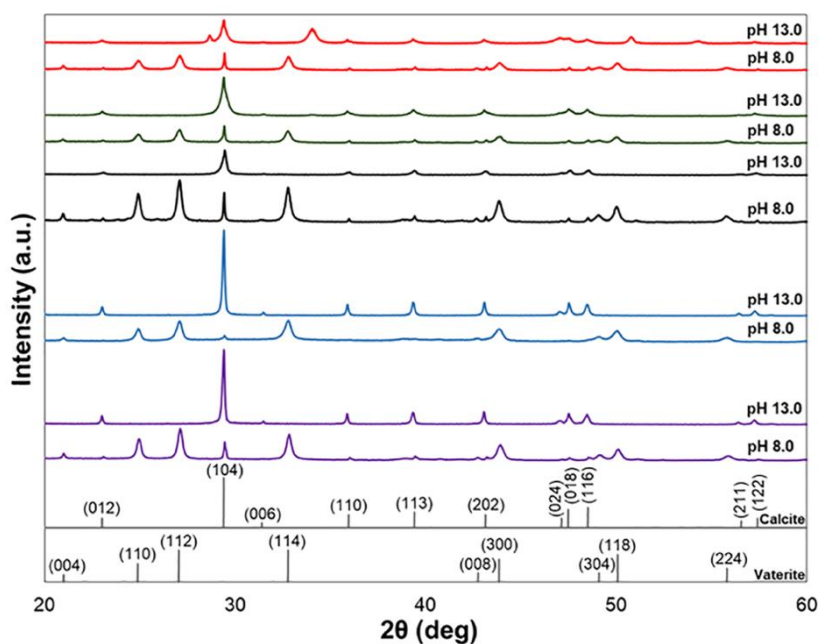


**Figure 4.2.** XRD patterns of  $\text{CaCO}_3$  particles synthesized at 5 different  $[\text{Ca}^{2+}]:[\text{CO}_3^{2-}]$  ratios at pH 8.0 and 13.0. Red, green, black, blue and purple lines indicate [5]:[1], [2]:[1], [1]:[1], [1]:[2] and [1]:[3] ratios, respectively. At pH 8.0, vaterite was the main  $\text{CaCO}_3$  polymorph, while calcite was the main  $\text{CaCO}_3$  polymorph at pH 13.0 for the investigated  $[\text{Ca}^{2+}]:[\text{CO}_3^{2-}]$  ratios. Gray lines are JCPDS references for vaterite (#033-0268) and calcite (#005-0586).

Having this said, independent of the  $[\text{Ca}^{2+}]:[\text{CO}_3^{2-}]$  ratios, vaterite to calcite polymorphic transformation was observed with an increase in pH for all the sample sets. This phenomenon could potentially be related to alteration in supersaturation upon changes in pH. According to estimations on supersaturation ( $S = (\text{IAP}/K_{\text{sp}})^{1/2}$  where IAP is ionic activity product ( $\text{IAP} = [\text{Ca}^{2+}][\text{CO}_3^{2-}]$ ) and  $K_{\text{sp}}$  is solubility product), supersaturation of the solution increased with increasing  $[\text{Ca}^{2+}]/[\text{CO}_3^{2-}]$  ratio [62]. In addition, increase in supersaturation was well-documented in literature

with increasing pH for CaCO<sub>3</sub> synthesis [54,63]. However, these assumptions of increased supersaturation were valid only at early stages of particle synthesis and prone to changes with time. For instance, Chen *et al.* [64] observed drastic decrease in supersaturation during CaCO<sub>3</sub> particle synthesis due to short induction times at high pH solutions. In this study, particles having [5]:[1] molarity ratio had the highest supersaturation and their supersaturation increased further with an increase in pH at early stages of particle synthesis. We could speculate that vaterite particles were obtained during the early stages independent of pH in this molarity ratio. However, at later stages, supersaturation dramatically decreased due to high nucleation rates observed at high pH solutions and vaterite particles transformed to calcite by dissolution and recrystallization reactions, whereas vaterite particles remained stable for low pH synthesis conditions [63,64]. Due to having different supersaturation values at different molar ratios and pH values, vaterite to calcite polymorphic transformation were not observed at a precise pH for all experimental set, yet a range of pH values for this polymorphic transformation was obtained in this study. Chen *et al.* [64] also observed that supersaturation of low pH solutions could surpass high pH solutions as reaction proceeds since low pH solutions did not have such drastic decrease in terms of supersaturation. Considering [1]:[3] molarity ratio solution, which had the lowest supersaturation, it was still possible to obtain vaterite, though. The supersaturation could constantly increase with increasing pH in this molarity ratio without the aforementioned decrease in supersaturation up to pH 12.0. Hence, calcite content obtained for [1]:[3] molarity ratio was lowered from 11.1 wt% at pH 8.0 to 1.8 wt% at pH 12.0.

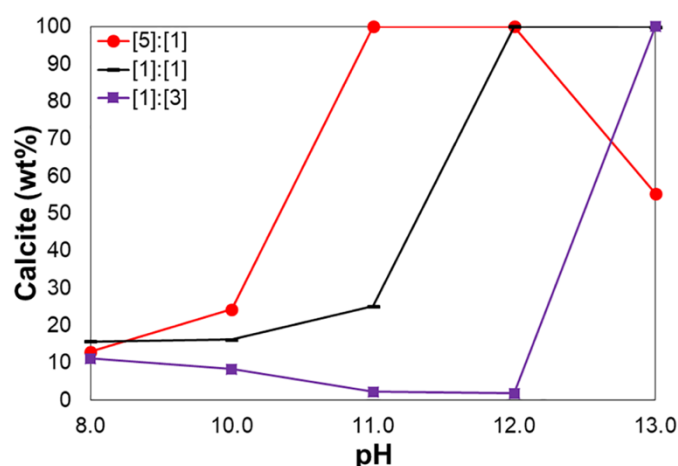


**Figure 4.3.** Percentage of calcite polymorph at different pH values for different  $[\text{Ca}^{2+}]:[\text{CO}_3^{2-}]$  ratios. Red, black and purple lines denote  $[5]:[1]$ ,  $[1]:[1]$  and  $[1]:[3]$  ratios, respectively. Vaterite to calcite polymorphic transformation was observed with an increase in pH value of the precursor solutions. The transformation pH decreased with increasing  $[\text{Ca}^{2+}]:[\text{CO}_3^{2-}]$  ratio.

$\text{CaCO}_3$  particles were also characterized using FTIR to observe the characteristic absorption bands of the  $\text{CaCO}_3$  polymorphs in  $1000\text{-}600\text{ cm}^{-1}$  region. Within this region, vaterite has absorption bands at  $877$  and  $744\text{ cm}^{-1}$  and calcite has absorption bands at  $876$ ,  $848$  and  $714\text{ cm}^{-1}$  [54,55]. FTIR analyses demonstrated the presence of vaterite and calcite polymorphs at pH 8.0, while there were only calcite polymorphs at pH 13.0 for all the investigated  $[\text{Ca}^{2+}]:[\text{CO}_3^{2-}]$  ratios. The FTIR results were in agreement with the XRD results (Figure 4.2) as discussed previously. Additionally, FTIR analysis did not show any of the EG absorption bands (C-H at  $725\text{ cm}^{-1}$  and C-C at  $885\text{ cm}^{-1}$ ) suggesting complete removal of the adsorbed EG from the  $\text{CaCO}_3$  particles [56].

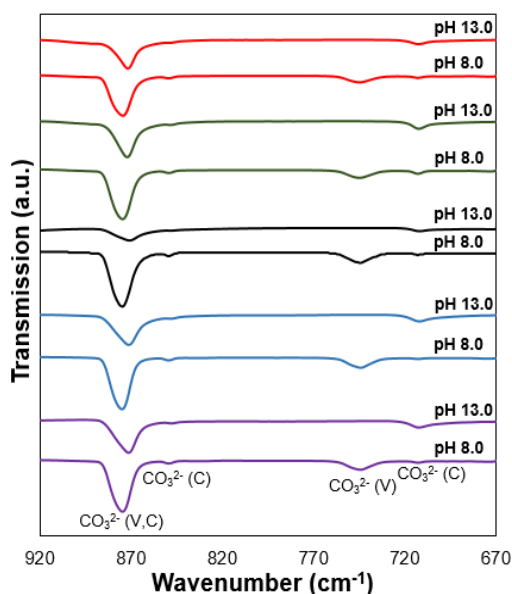


**Figure 4.4.** FTIR spectra of  $\text{CaCO}_3$  particles synthesized at 5 different  $[\text{Ca}^{2+}]:[\text{CO}_3^{2-}]$  ratios at pH 8.0 and 13.0. Red, green, black, blue and purple lines indicate [5]:[1], [2]:[1], [1]:[1], [1]:[2] and [1]:[3]  $[\text{Ca}^{2+}]:[\text{CO}_3^{2-}]$  ratios, respectively. ‘V’ and ‘C’ denote peaks corresponding to vaterite and calcite polymorphs. Both vaterite and calcite peaks were present at pH 8.0, while only calcite peaks were observed at pH 13.0.

To obtain information on the internal structures of synthesized vaterite and calcite polymorphs, TEM characterizations were performed. For these analyses, particles synthesized at pH 8.0 and 13.0 having [1]:[2] ratio were used. Bright-field micrograph of vaterite (Figure 4.5a) showed elliptical geometry of the particle and the constituent nanocrystals having 50-100 nm length joined in an aligned fashion to form the vaterite polymorph. Having discontinuous circles in the SAED pattern, the polycrystalline nature of vaterite particle was evident (Figure 4.5a-inset) and in accord with polycrystalline pattern shown in its XRD spectra (Figure 4.2). In addition, porous structure of vaterite particle was evident in the TEM micrograph, consistent with previous findings of Wang *et al.* [31]. Although full mechanism of vaterite particle formation has not been elucidated yet, decreasing total surface energy upon particle formation has been proposed as the driving force for the

synthesis of vaterite [56]. For the case of calcite polymorph (Figure 4.5c), bright-field micrographs showed its rhombohedral morphology. Due to having a large particle size ( $3\mu$ ), FIB was used to prepare 80 nm thick film for detailed structural analysis. HR-TEM micrographs of vaterite (Figure 4.8b) and calcite (Figure 4.8d) exhibited the differences between their d-spacing, where d-spacing of calcite was 0.301 nm, while that of vaterite was 0.276 nm, again highlighting the influence of precursor pH on  $\text{CaCO}_3$  polymorph. According to JCPDS references for calcite (#005-0586) and vaterite (#033-0268), d-spacing values corresponded to (104) and (114) planes, respectively.

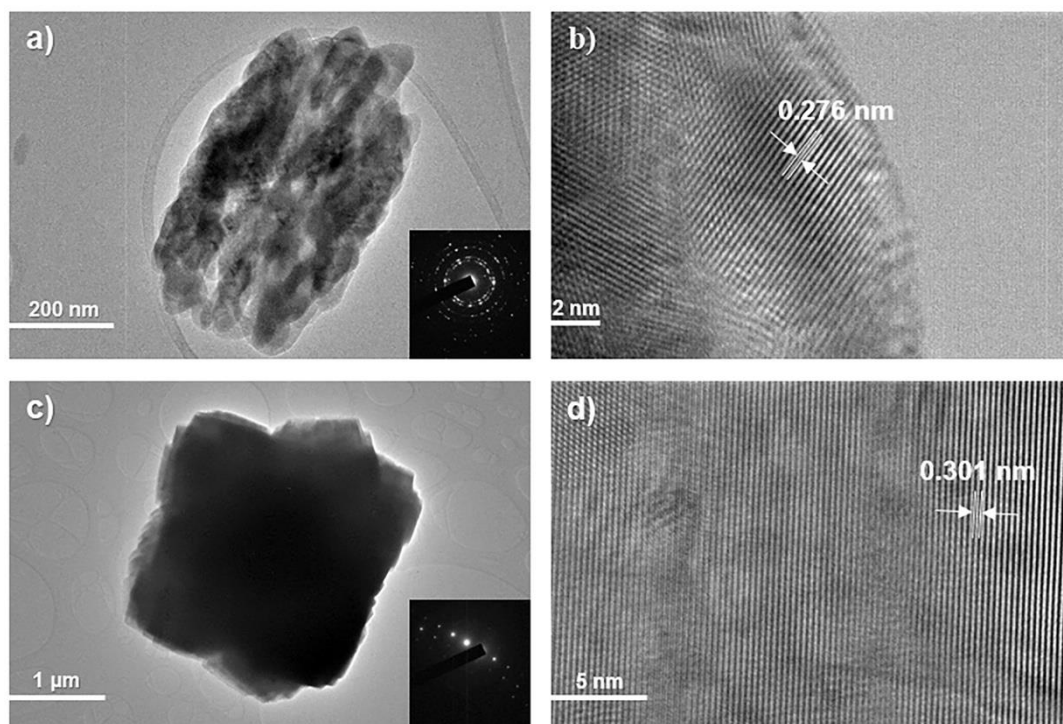


**Figure 4.5.** a) and b) vaterite (pH 8.0) and c) and d) calcite (pH 13.0) polymorphs synthesized at [1]:[2]  $[\text{Ca}^{2+}]:[\text{CO}_3^{2-}]$  ratio. a) and c) TEM and b) and d) HR-TEM micrographs. Insets show selected area diffraction patterns obtained from the particles.

#### 4.1.2 Effect of pH and $[\text{Ca}^{2+}]:[\text{CO}_3^{2-}]$ Ratio on $\text{CaCO}_3$ Particle Size and Morphology

Figures 4.1 and 4.6 highlighted the correlation between precursor solution pH and  $\text{CaCO}_3$  particle size, where increased basicity of the precursor solutions increased  $\text{CaCO}_3$  particle size. The aforementioned size change was especially noticeable when there was a polymorphic transformation from vaterite to calcite. It was also possible to form  $\text{CaCO}_3$  particles having submicron dimensions via proper selection of pH and  $[\text{Ca}^{2+}]:[\text{CO}_3^{2-}]$  ratios, where the smallest average particle size obtained in this study was  $0.66 \pm 0.13 \mu\text{m}$  using pH 8.0 and [1]:[2] ratio. When pH of the precursor solutions increased, the size of  $\text{CaCO}_3$  particles synthesized using [1]:[2]  $[\text{Ca}^{2+}]:[\text{CO}_3^{2-}]$  ratio constantly increased, reaching  $4.09 \pm 0.87 \mu\text{m}$  at pH 13.0. The increase in  $\text{CaCO}_3$  particle size with an increase in precursor solution pH was independent from the  $[\text{Ca}^{2+}]:[\text{CO}_3^{2-}]$  ratios used in this study, offering a potential method to fine-tune  $\text{CaCO}_3$  particle size for a desired application. In fact, the largest average particle size among all samples was observed using [5]:[1] and [2]:[1]  $[\text{Ca}^{2+}]:[\text{CO}_3^{2-}]$  ratios at pH 13.0 (Figure 4.1), yet the size of flower-like morphology could not be reported accurately due to irregularity of this morphology. Increase in average size of  $\text{CaCO}_3$  particles could be explained with pH and its influence on supersaturation. As mentioned previously, increase in pH of the precursor solutions led to an increase in supersaturation. In literature, growth rate of  $\text{CaCO}_3$  particles was found to be linearly proportional with supersaturation [65-67]. It could be speculated that the growth rate, and thus, the average size of vaterite particles increased with an increase in pH of the precursor solutions. For the case of calcite particles, which form at high pH values, the uncontrolled nucleation rates observed at high pH values could contribute for the changes in average particle size [30].

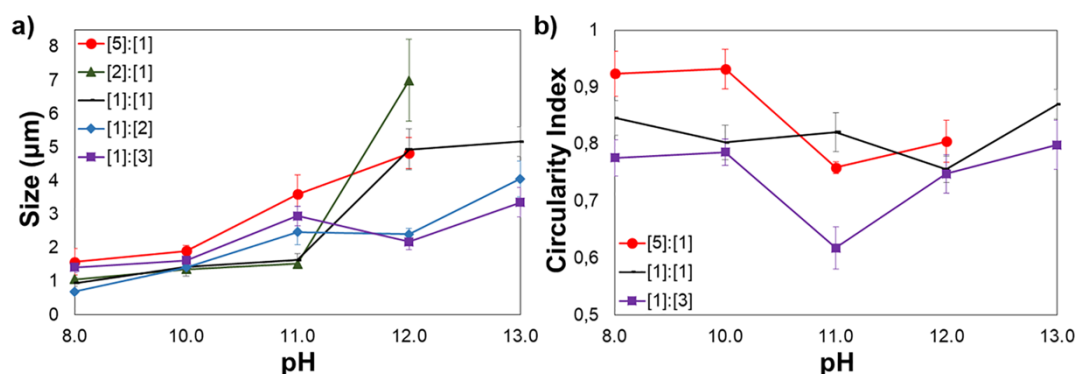


**Figure 4.6.** a) CaCO<sub>3</sub> particle size obtained at different pH values using 5 different [Ca<sup>2+</sup>]:[CO<sub>3</sub><sup>2-</sup>] ratios. Increase in particle size with an increase in precursor solution pH was observed. Values are mean ± SEM; n=5. b) Circularity index of CaCO<sub>3</sub> particles synthesized at different pH values using 3 different [Ca<sup>2+</sup>]:[CO<sub>3</sub><sup>2-</sup>] ratios. Higher circularity indices were obtained for solutions having excess Ca<sup>2+</sup> cations at lower pH values. Circularity indices of 1.0, 0.88 and 0.66 correspond to circle, square and ellipsoid particle morphology, respectively. Red, green, black, blue and purple lines indicate [5]:[1], [2]:[1], [1]:[1], [1]:[2] and [1]:[3] [Ca<sup>2+</sup>]:[CO<sub>3</sub><sup>2-</sup>] ratios, respectively.

Having this said, morphology of the synthesized CaCO<sub>3</sub> particles (Figure 4.1) were also altered by the pH and [Ca<sup>2+</sup>]:[CO<sub>3</sub><sup>2-</sup>] ratio of the precursor solutions. For instance, at pH 8.0 and 10.0 using [5]:[1] ratio, spherical vaterite morphologies were obtained. Holding the pH value constant and decreasing the [Ca<sup>2+</sup>]:[CO<sub>3</sub><sup>2-</sup>] ratio, vaterite polymorph morphologies transformed to a more ellipsoidal form. As mentioned previously, supersaturation increased with increasing [Ca<sup>2+</sup>]:[CO<sub>3</sub><sup>2-</sup>] ratio for CaCO<sub>3</sub> synthesis. In fact, obtaining spherical particles at high supersaturation solutions were consistent with findings of Granasy *et al.* [68] and Beck *et al.* [69]. In another study, Andreassen *et al.* [70] obtained dumbbell-shaped particles at low supersaturation solutions due to insufficient branching, whereas fully grown spherulites were synthesized at high supersaturation solutions. Therefore, we can speculate that common morphology of vaterite (ellipsoidal) was obtained at low supersaturation, whereas branching increased and spherical morphologies were

obtained with increase in supersaturation. Furthermore, at pH 11.0, spherical vaterite particles transformed to rhombohedral calcite particles (for [5]:[1] ratio), while particles having [1]:[3] and [1]:[2] ratios slightly changed their morphologies to spheroidal vaterite, *i.e.* morphology having sharper tips and wider midsection than ellipsoidal morphology, without undergoing any polymorph transformation. Furthermore, once pH values reached 12.0, particles having [5]:[1] and [2]:[1] ratios showed flower-like and rhombohedral calcite morphologies, respectively; finally transforming to flower-like calcite at pH 13.0. For the case of spheroidal vaterite, it transformed to irregular calcite at pH 13.0. In literature, rhombohedral morphology of calcite is commonly encountered, yet irregular and flower-like morphologies were also obtained in this study. These morphologies observed at high pH solutions might be related to pH-dependent dissolution of calcite, *i.e.* favored dehydration of  $\text{Ca}^{2+}$  with increase in excess  $\text{OH}^-$  ions [71,72]. Cizer *et al.* [71] also stated that calcite may re-grow after dissolution if sufficient amount of  $\text{Ca}^{2+}$  and  $\text{CO}_3^{2-}$  ions were present in the system. Therefore, flower-like morphologies obtained in this study might be the result of dissolution and re-growth processes of calcite particles. Although the main mechanism was not clear, re-growth process might not be applicable for calcite particles at low  $[\text{Ca}^{2+}]:[\text{CO}_3^{2-}]$  ratios, and thus irregular rhombohedral morphologies were obtained.

To better discuss  $\text{CaCO}_3$  particle morphologies, circularity index of particles (Figure 4.6b) were obtained using ImageJ software. Having a high circularity index, spherical vaterite morphology at low pH and high  $[\text{Ca}^{2+}]:[\text{CO}_3^{2-}]$  ratio was confirmed. The abrupt decrease in circularity values of particles around pH 11.0 were attributed to transformation of spherical/ellipsoidal vaterite to rhombohedral calcite/spheroidal vaterite, further stressing the influence of pH and  $[\text{Ca}^{2+}]:[\text{CO}_3^{2-}]$  ratios on particle size and morphology.

### 4.1.3 Comparison of pH and EG Ratio Effects on CaCO<sub>3</sub> Particle Properties

There are several studies investigating the effect of EG as a non-aqueous polar solvent for CaCO<sub>3</sub> particle synthesis [21,57,73]. For instance, Svenskaya *et al.* [56] synthesized the least stable form of CaCO<sub>3</sub> polymorph (vaterite) by adjusting EG concentration of the precursor solutions to 80%, while calcite polymorph was stable at 50% EG concentration. Similarly, Flaten *et al.* [52] controlled calcite polymorph ratio between 100 wt% to 35 wt% by using 0 wt% and 75 wt% (mono)EG, respectively. In these studies, vaterite (the least stable anhydrous CaCO<sub>3</sub> polymorph having the strongest tendency for polymorphic transformation) was synthesized using high EG concentrations due to the strong association of Ca<sup>2+</sup> cations with alcohol groups of EG, which increased local supersaturation of the solution [21,57]. Thus, to be able to synthesize both vaterite and calcite particles in this study, EG concentration of the precursor solutions were chosen to be 83% before adjusting pH values [29]. However, while adjusting solution pH via incorporating of aqueous NaOH solution, EG concentrations got diluted. Since adjusting pH of the precursor solutions to different values (*i.e.* pH 10.0 and pH 13.0) required incorporation of different volumes of NaOH solution (less NaOH addition for pH 10.0 and more NaOH addition for pH 13.0), EG concentration of the precursor solutions was differing up to 50%. In other words, to increase pH of the precursor solutions by incorporation of NaOH solution, their EG concentrations had to be decreased. The decrease in EG concentration was more biased towards high pH solutions due to incorporation of more NaOH solution to adjust pH to higher values. Since EG to water ratio was important in determining the CaCO<sub>3</sub> polymorph, it was critical to understand if the observed trends were due to increasing the water content (decreasing EG content) or increasing the pH value of the experimental set-up. Thus, to understand the dominant factor controlling particle morphology and vaterite to calcite transformation, control experiments were devised. For samples having [1]:[2] [Ca<sup>2+</sup>]:[CO<sub>3</sub><sup>2-</sup>] ratio, one set of experiments were completed with adjusting the pH of

the precursor solutions to 10.0, 11.0, 12.0 and 13.0 by incorporation of NaOH solution (Figure 4.7, top row), while a control set was devised to have the exact same concentration of EG for each pH condition without adjusting their pH (Figure 4.7, bottom row).

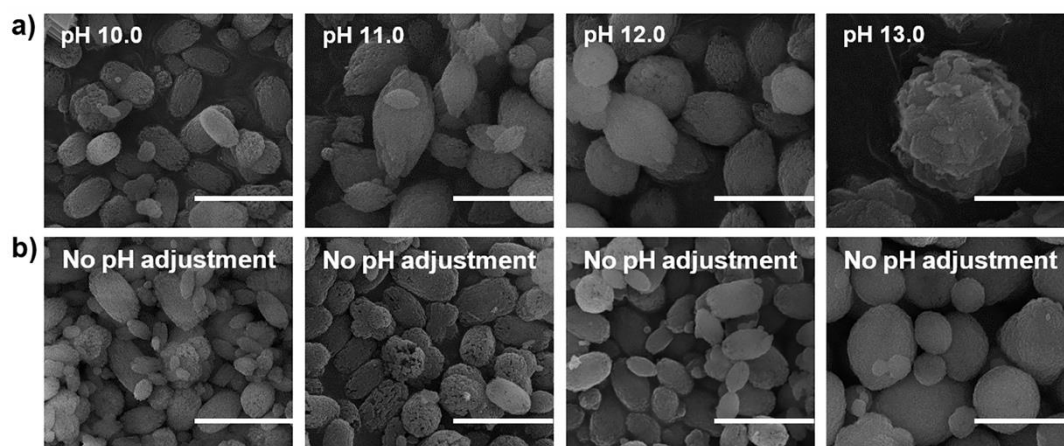


**Figure 4.7.** SEM micrographs of  $\text{CaCO}_3$  particles synthesized using [1]:[2]  $[\text{Ca}^{2+}]:[\text{CO}_3^{2-}]$  ratio a) with (top row) and b) without pH adjustment (bottom row). Particles on each column have the same EG concentration.  $\text{CaCO}_3$  particle morphology and polymorph differed upon changes in pH value. Scale bars are 3  $\mu\text{m}$ .

SEM (Figure 4.7) and XRD (Figure 4.8a) results of these samples revealed morphological and polymorphic differences between pH-adjusted and their corresponding control samples. At pH 10.0, these differences were minute (both samples consist of ellipsoidal vaterite particles with a negligible amount of calcite). However, with an increase in pH, differences between two sets began to appear. When pH of the precursor solutions was adjusted to 11.0 and 12.0, spheroidal vaterite morphologies were obtained in pH-adjusted samples. Their XRD results also showed low-intensity calcite peaks for these particles. However, control samples of pH 11.0 and 12.0 showed ellipsoidal morphology and had more intense calcite peaks at their XRD spectra. The effect of pH became more evident when it was adjusted to 13.0. For the pH-adjusted sample, only calcite peaks appeared, whereas its corresponding control sample did not exhibit polymorphic transformation and had both vaterite and

calcite peaks at its XRD spectra. In addition, pH-adjusted sample exhibited irregular rhombohedral morphology, whereas its control sample showed spherical morphology. FTIR results (Figure 4.8b) of control samples supported these findings, where all of the control samples expressed absorption bands belonging to vaterite and calcite polymorphs.

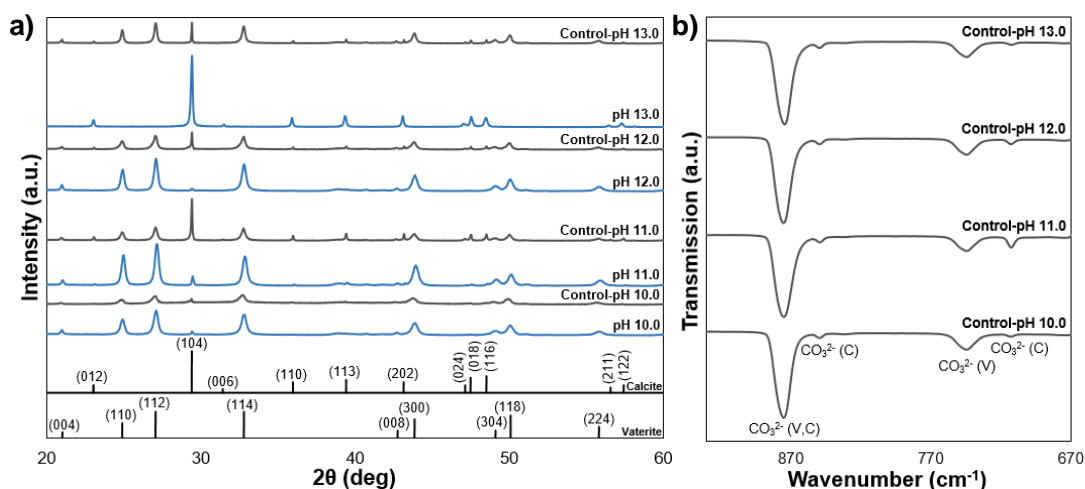


**Figure 4.8.** a) XRD patterns of particles synthesized at pH 10.0, 11.0, 12.0 and 13.0 having [1]:[2] [Ca<sup>2+</sup>]:[CO<sub>3</sub><sup>2-</sup>] ratio (blue lines) and their corresponding control samples having the same EG concentration but without any pH adjustment (gray lines). Black lines are JCPDS references for vaterite (#033-0268) and calcite (#005-0586). b) FTIR spectra of the control samples. ‘V’ and ‘C’ denote peaks corresponding to vaterite and calcite, respectively. While pH-controlled samples exhibited vaterite to calcite transformation with an increase in pH, control samples did not show polymorph transformation.

It should be noted that for the control samples, the change in vaterite morphology from ellipsoidal to spherical, mixed with different amounts of calcite, supported the previous findings of Svenskaya *et al.* [56] and Qi *et al.* [29], who observed EG concentration was influential in determining CaCO<sub>3</sub> particle properties. However, comparison of pH-adjusted and their corresponding control samples suggested pH to be a stronger factor controlling CaCO<sub>3</sub> particle properties. Though EG concentration

affected the particle morphology, the influence of pH was greater than that of EG concentration and controlled polymorphic transformation of CaCO<sub>3</sub> particles.

This study showed that pH and [Ca<sup>2+</sup>]:[CO<sub>3</sub><sup>2-</sup>] ratio of the precursor solutions can be utilized as experimental variables to obtain desired CaCO<sub>3</sub> particle morphology, size and polymorph. In addition, control experiments showed the strong influence of solution pH on the synthesized CaCO<sub>3</sub> particle properties compared to EG concentration of the precursor solutions. To conclude, well-specified fabrication routes offered in this study can be used to synthesize CaCO<sub>3</sub> particles with controlled properties for biomedical applications.



## CHAPTER 5

### EFFECT OF POLYMORPHISM ON THE BIOCOMPATIBILITY OF CaCO<sub>3</sub> PARTICLES

Until recently, various synthesis routes for the well-known morphologies of vaterite (ellipsoidal), aragonite (needle-like) and calcite (rhombohedral) were investigated in detail [19]. In parallel, there were numerous studies revealing the biocompatibility of CaCO<sub>3</sub> particles and their potential use in biomedical applications [73]. For example, researchers showed that CaCO<sub>3</sub> microspheres could be used to encapsulate biomacromolecules and drugs [74]. As the solution-precipitated CaCO<sub>3</sub> particles had an isoelectric point of 8.5, negatively charged proteins could be adsorbed onto the particles at lower pH values (< 8.5) [74]. In addition, owing to the interconnected porosity and nanoscale roughness of aragonite-based scaffolds, they were observed to stimulate *in vitro* cellular functions [75]. Vaterite particles were also proposed for drug delivery applications due to their large surface area and degradability in biological fluids. Since tumor niche typically presents acidic conditions (pH < 6.5), pH-triggered degradation of CaCO<sub>3</sub> particles was a potential approach to control the release of their payload [76].

Once the potential of different CaCO<sub>3</sub> polymorphs was revealed for biomedical applications, researchers aimed to improve their performance, especially in bone regeneration via the synthesis of CaCO<sub>3</sub> particles in various hierarchical morphologies [19]. Despite all the beneficial literature on biomedical use of CaCO<sub>3</sub> polymorphs in their conventional morphologies, a systematic study investigating the biocompatibility of vaterite, aragonite and calcite particles at identical conditions was not present. In our previous studies, we showed that CaCO<sub>3</sub> polymorphs to possess different particle morphologies could be obtained by altering the precipitation medium, pH and temperature [77,78]. In this work, by following a previously established synthesis route, a systematic study on the precipitation of

CaCO<sub>3</sub> particles and their interactions with human bone cells (hFOB) were performed. Initially, ellipsoidal vaterite, bowknot-like aragonite and rhombohedral calcite particles were precipitated in aqueous environments using different precursor ratios, EG concentrations, pH and temperature. Then, hFOB cell proliferation upon the interaction with the particles was investigated up to 5 days *in vitro*.

## 5.1 Results and Discussion

Morphology of the synthesized particles was investigated using SEM (Figure 5.1). As these micrographs clearly showed, reacting the precursors at [0.3]:[0.9] ratio in 90% EG solution at 70 °C led to the formation of ellipsoidal particles (Figure 5.1a). Decreasing the EG concentration to 20%, while keeping the precursor ratio and the synthesis temperature constant, led to the formation of bowknot-like morphology (Figure 5.1b). For the synthesis of rhombohedral particles (Figure 5.1c), the initial EG concentration was adjusted to be 80%, while pH value of the precursors was controlled to be 11 via the addition of NaOH at 25 °C. Image analysis revealed that ellipsoidal, bowknot-like and rhombohedral particles had average size values of  $2.36 \pm 0.49$ ,  $19.59 \pm 1.96$  and  $3.20 \pm 0.78$   $\mu\text{m}$ , respectively.

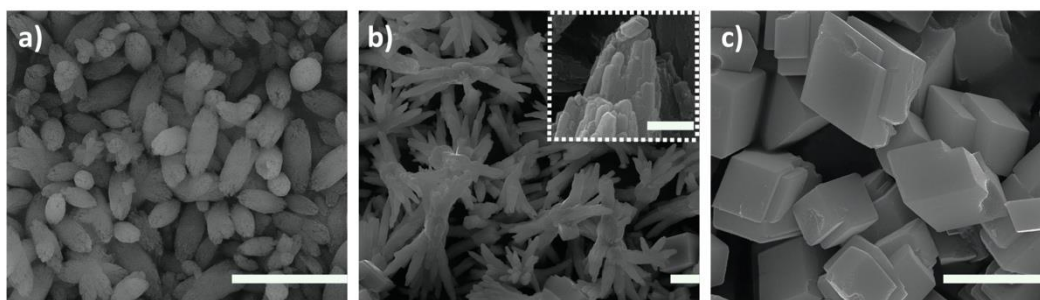


**Figure 5.1.** SEM micrographs of a) ellipsoidal vaterite, b) bowknot-like aragonite and c) rhombohedral calcite particles synthesized at different conditions. Scale bars are 5  $\mu\text{m}$ . Inset shows high magnification SEM micrograph of bowknot-like aragonite particles and its scale bar is 1  $\mu\text{m}$ .

In order to investigate the particle polymorphs, XRD and FTIR analyses were performed. XRD spectra of the synthesized particles were shown and compared to JCPDS references of vaterite, aragonite and calcite polymorphs of  $\text{CaCO}_3$  in Figure 5.2. The XRD spectrum obtained from ellipsoidal particles (Figure 5.2a) expressed peaks that could be ascribed to (004), (110), (112), (114), (008), (300), (304) and (118) crystallographic planes of vaterite (#033-0268), respectively. Due to the unstability of vaterite polymorph, nonaqueous polar solvents, such as EG and glycerol, were typically used to stabilize vaterite particles [29]. Since transformation of vaterite occurred via dissolution and recrystallization reactions, low solubility of  $\text{CaCO}_3$  inside EG limited vaterite to calcite transformation [66]. For bowknot-like particles, XRD spectrum was shown in Figure 5.2b, where the peaks could be indexed to (111), (021), (002), (121), (012), (200), (031), (112), (130), (211), (220), (221), (041), (202) and (132) planes of aragonite (#005-0453) and (012), (104), (006), (110), (113), (202), (024), (018) and (116) planes of calcite (#005-0586), respectively. On the other hand, XRD spectrum of rhombohedral particles (Figure 5.2c) contained only calcite peaks due to being the most stable form of  $\text{CaCO}_3$ . FTIR spectra of the particles were also given in Figure 5.3 and they were in-line with the findings of XRD analysis. The characteristic IR absorbance bands at 877 and 744  $\text{cm}^{-1}$  corresponded to the formation of vaterite, bands at 854, 712 and 700  $\text{cm}^{-1}$  corresponded to aragonite and bands at 876, 848 and 714  $\text{cm}^{-1}$  corresponded to calcite polymorph [54,55]. XRD and FTIR results showed that ellipsoidal and bowknot-like particles contained low amount of calcite, yet rhombohedral calcite particles were phase-pure due to the thermodynamic stability of calcite polymorph.

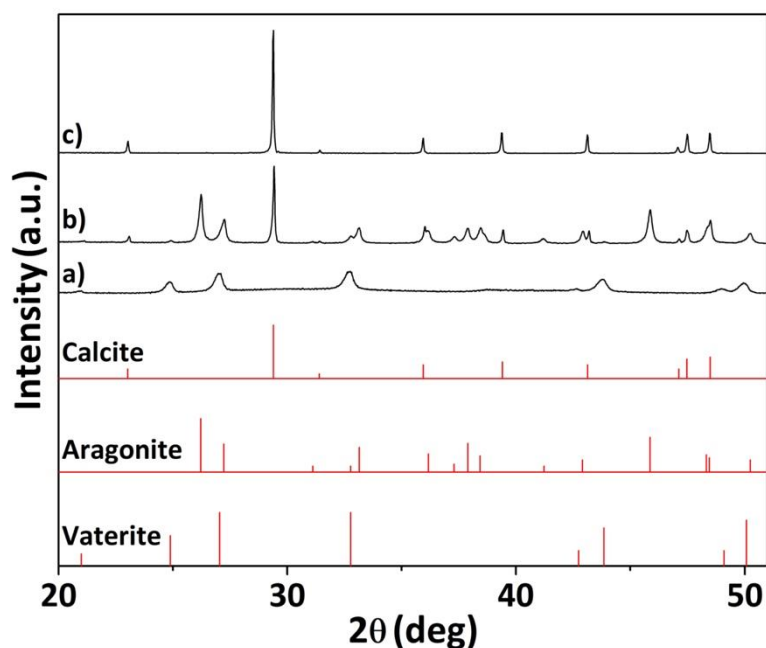


**Figure 5.2.** XRD patterns of a) ellipsoidal vaterite, b) bowknot-like aragonite and c) rhombohedral calcite particles. Red lines are JCPDS references for vaterite (#033-0268), aragonite (#005-0453) and calcite (#005-0586).

Precipitation of ellipsoidal vaterite particles inside EG-containing solutions was also observed in previous studies [29]. In order to stabilize vaterite particles, decreasing their solubility by utilization of a high EG-containing precursor was a successful strategy [66]. However, formation of aragonite particles in bowknot-like morphology at a moderately low temperature (70 °C) was uncommon. As clearly seen in Figure 5.1b inset, smaller particles attached to each other rather than forming a smooth surface consisting of large crystallites, as observed in rhombohedral calcite particles (Figure 5.1c). This observation could indicate that bowknot-like particle formation occurred by a mechanism based on oriented attachment theory of crystals [79]. It could be speculated that oriented attachment mechanism, typically observed for the formation of hierarchical ceramic particles under hydrothermal conditions, dominated over the classical (homogeneous) growth mechanism for bowknot-like aragonite particles [79,80]. Although time-dependent experiments should be devised to obtain more information on the growth behavior, it could be said that high-energy

faces combined at the core to decrease the surface energy, leading to growth on these surfaces and forming the branches of the bowknot-like morphology [79,80]. For rhombohedral calcite particles, an alternate protocol was utilized where solution pH dictated the particle polymorph. During  $\text{CaCO}_3$  particle synthesis, increase in supersaturation was typically observed at early stages of nucleation with an increase in pH values of the precursor solutions [54]. However, short induction times observed at high pH solutions could lead to drastic decrease in supersaturation [64]. In this study, pH was adjusted to 11 during the synthesis of rhombohedral calcite particles, which allows us to speculate nucleation of vaterite particles at early time points. However, due to the low stability of vaterite polymorph in aqueous environments and the decrease in supersaturation due to the short induction times, the initially obtained vaterite particles could transform to rhombohedral calcite during the synthesis time (1 h) via dissolution and recrystallization reactions.

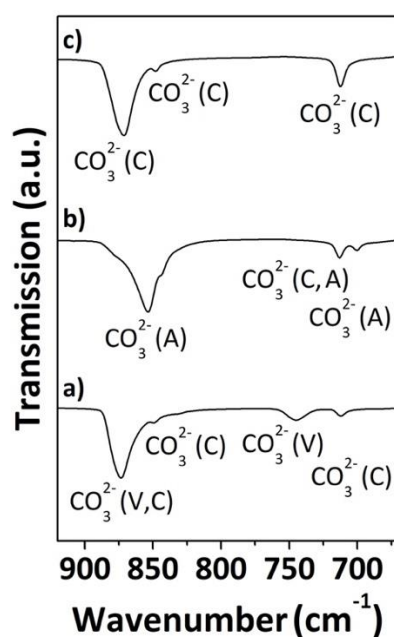


**Figure 5.3.** FTIR spectra of a) ellipsoidal vaterite, b) bowknot-like aragonite and c) rhombohedral calcite particles. ‘V’, ‘A’ and ‘C’ denote peaks corresponding to vaterite, aragonite and calcite polymorphs, respectively.

Since  $\text{CaCO}_3$  particles have remarkable potential in bone tissue engineering applications, metabolic activity of hFOB cells upon the interaction with these particles was investigated using an MTT assay. For the biological experiments, ellipsoidal vaterite, bowknot-like aragonite and rhombohedral calcite particles were dispersed in DMEM at 0.01, 0.1, and 1 mg/ml concentrations and interacted with hFOB cells up to 5 days *in vitro* (Figure 5.4). The results showed that hFOB cells were viable and proliferated up to 5 days independent of the particle type and concentration, while the highest particle concentration (1 mg/ml) for bowknot-like aragonite particles exhibited the least cellular proliferation. For ellipsoidal vaterite particles (Figure 5.4a), cellular proliferation decreased with an increase in the particle concentration compared to the control group. For the case of bowknot-like aragonite (Figure 5.4b) and rhombohedral calcite (Figure 5.4c) particles, there was no change in cellular proliferation compared to the control group at 0.01 and 0.1 mg/ml concentrations. However, a drastic decrease in cellular proliferation was observed upon the incorporation of 1 mg/ml aragonite particles into the culture medium, whereas decrease in cellular proliferation was less for calcite and vaterite particles at the same concentration.

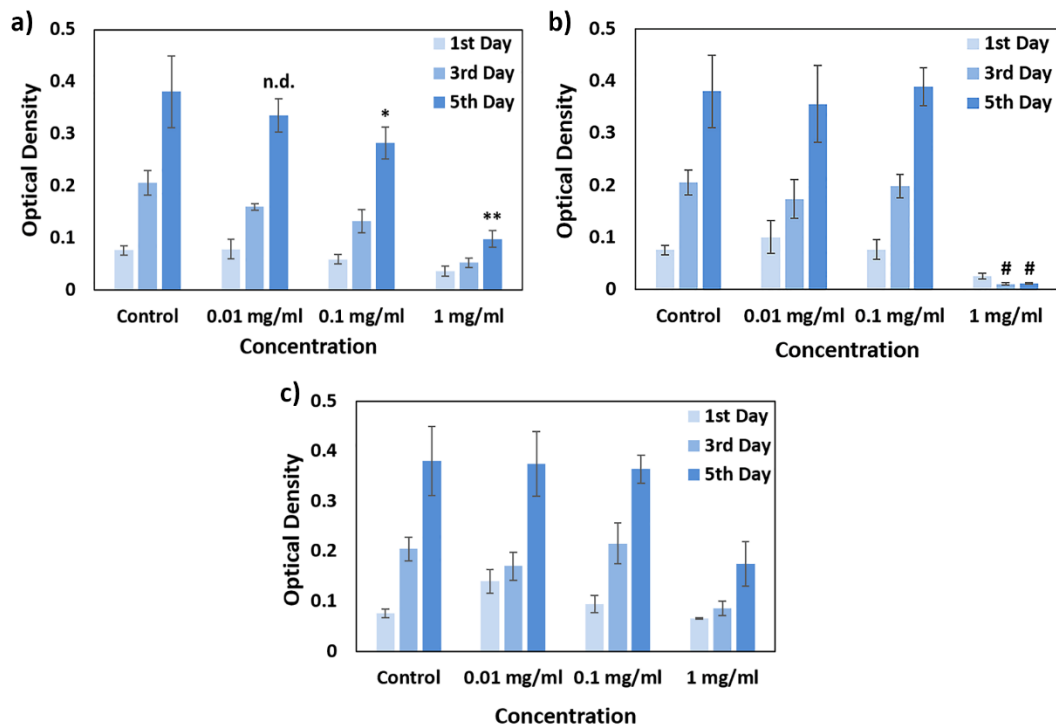


**Figure 5.4.** Proliferation of hFOB cells exposed to a) ellipsoidal vaterite, b) bowknot-like aragonite and c) rhombohedral calcite particles at different concentrations up to 5 days of culture (Mean  $\pm$  SD, n = 3). Cells cultured without the particles were denoted as control. \* $p < 0.01$  and \*\* $p < 0.001$  compared to control group. # $p < 0.001$  compared to all groups.

It could be stated that independent of the particle properties, 0.01 mg/ml concentration did not influence cellular densities. For ellipsoidal vaterite particles, hFOB cells exhibited an earlier response to concentration changes, which showed statistically significant decrease at 0.1 mg/ml concentration at 5 days *in vitro*. On the other hand, hFOB cells were more tolerant to bowknot-like aragonite and rhombohedral calcite particles, which exhibited similar cellular densities with the control groups at 0.1 mg/ml particle concentration. As an important finding, rhombohedral calcite particles allowed the highest cellular density at 1 mg/ml concentration at 5 days of culture. It was interesting to note the aforementioned differences in cellular densities upon the interaction with different  $\text{CaCO}_3$  particles.

It was known that vaterite polymorph had the highest solubility in aqueous solutions, including the cell culture medium used in this study [73]. Therefore, ellipsoidal vaterite particles could increase the ionic concentration in the medium, which further decreased the cellular proliferation in a dose-dependent fashion. Since aragonite had a lower solubility than vaterite, bowknot-like aragonite particles did not lead to a decrease in cellular density at 0.1 mg/ml concentration. Among all CaCO<sub>3</sub> polymorphs, calcite was the most stable one in aqueous environments, and thus exhibited the highest cellular density [73]. In addition to the solubility differences between CaCO<sub>3</sub> polymorphs, morphology and size of the particles could affect cellular densities. In literature, it was shown that the frequency of particle internalization, which was inversely correlated with cell viability, increased with an increase in aspect ratio for ellipsoidal, cuboidal and spherical CaCO<sub>3</sub> particles [36,81]. It was possible that cellular density differences observed between ellipsoidal vaterite and rhombohedral calcite particles, which had similar particle size, could be due to the differences in particle morphologies, where higher aspect ratio of ellipsoidal vaterite had a high internalization frequency, and thus yielded lower cellular densities at 0.1 and 1 mg/ml concentrations. On the other hand, high size of bowknot-like aragonite particles (> 6 times higher than ellipsoidal vaterite and rhombohedral calcite particles) could play a more decisive role for the observed cellular densities. Since micron-sized particles having a needle-like shape was more likely to damage cellular membranes compared to smaller and lower aspect ratio particles, the coupled effect of these parameters could lead to the sharp decrease in cellular density at 1 mg/ml concentration for bowknot-like aragonite particles [1]. Therefore, this study highlighted ellipsoidal vaterite and rhombohedral calcite particles, rather than bowknot-like aragonite particles, as promising candidates for orthopedic applications.

## CHAPTER 6

### SYNTHESIS OF CaCO<sub>3</sub> MICROSPHERES VIA INERT GAS BUBBLING FOR ORTHOPEDIC APPLICATIONS

Among various CaCO<sub>3</sub> morphologies, CaCO<sub>3</sub> spheres exhibited significant potential for biomedical applications, and thus their synthesis routes captured the attention of various research groups [19]. For instance, Geng *et al.* [82] synthesized vaterite and calcite spheres via incorporation of polystyrene sulfonate (PSS) as an additive using gas-liquid diffusion method. Ahmed *et al.* [83] utilized micro-emulsion method, where CTAB and 1-butanol were used to promote precipitation of vaterite spheres. On the other hand, Zhang *et al.* [33] used simple mixing approach where water/ethanol solution in the presence of PSS was mixed with precursors to obtain vaterite spheres.

Aside from particle synthesis studies, the use of CaCO<sub>3</sub> spheres in dental, orthopedic and drug delivery applications was also reported [19]. For instance, CaCO<sub>3</sub> spheres could transform to hydroxyapatite compounds, the naturally occurring component of bone and dentin, upon interacting with SBF and revealed enhanced bioactivity for bone-tissue engineering [84]. Similarly, Li *et al.* [85] observed that CaCO<sub>3</sub>/casein spheres could enhance deposition of hydroxyapatite compounds in SBF solution. In another study, Zhong *et al.* [86] used CaCO<sub>3</sub> spheres as a secondary phase within sodium alginate to obtain a degradable composite structure. Upon injection of this composite into subcutaneous tissue of mice, improved tissue fiber penetration and vessel ingrowth were observed at 3 months of implantation [86]. Once CaCO<sub>3</sub> spheres were synthesized to have hollow cores, they provided distinct advantages, *i.e.* high specific surface area, low bulk density and high permeability, over the conventionally-used ceramic based microparticles [87]. As stated previously, Wei *et al.* [43] used hollow vaterite spheres to deliver anticancer drug DOX to liver carcinoma cells. Almost no toxic effect was observed without DOX, yet death of

cancer cells soared upon the incorporation of DOX into the hollow particles [43]. In addition, CaCO<sub>3</sub> spheres with hollow cores could allow encapsulation of biomolecules, *i.e.* bovine serum albumin and DNA, for sustained release in body fluids [88].

Due to the potential use of hollow CaCO<sub>3</sub> spheres in biological applications, sound synthesis methods to advance the properties of hollow CaCO<sub>3</sub> spheres are required. Several studies investigated fabrication of hollow CaCO<sub>3</sub> spheres by synergistically coupling the use of additives with a suitable temperature adjustment during particle synthesis. Chen *et al.* [31] obtained hollow vaterite spheres via the incorporation of urea into water/ethanol mixture and holding the solution temperature at 90 °C for 24 hours. Yan *et al.* [89] showed that hollow calcite spheres could be fabricated using an aqueous mixture of Pluronic F127 and SDS at 30 °C. Water-in-oil-in-water method was also utilized to precipitate hollow vaterite spheres at 30 °C, where Tween 85 was used as non-anionic surfactant in the presence of n-hexane [90]. Cumulatively, all of these studies point to either high temperatures or high concentration of surfactants/additives to crystallize CaCO<sub>3</sub> spheres having hollow cores.

Until recently, the synthesized hollow CaCO<sub>3</sub> particles were mostly vaterite, the most soluble anhydrous polymorph of CaCO<sub>3</sub>. As stated previously, vaterite particles dissolve in aqueous conditions and spontaneously transform to more stable polymorphs. This polymorphic transformation induces dramatic changes in CaCO<sub>3</sub> particle size and morphology, and lead to premature loss of the hollow core inside the particle before completing its intended use. Precipitation of more stable CaCO<sub>3</sub> polymorphs, while maintaining their spherical and hollow characteristics, could be a potential remedy for the aforementioned problem. For this purpose, N<sub>2</sub> bubbles stabilized by SDS were used -for the first time- in this study as templates for CaCO<sub>3</sub> precipitation.

## 6.1 Results and Discussion

### 6.1.1 Influence of Synthesis Parameters on CaCO<sub>3</sub> Polymorph and Morphology

Investigation of the CaCO<sub>3</sub> particles using SEM (Figures 6.1 and 6.2) and XRD (Figure 6.3a) highlighted drastic differences upon SDS incorporation and N<sub>2</sub> bubbling under different synthesis conditions. In Figure 6.1, the morphologies of the synthesized CaCO<sub>3</sub> particles were shown as per changes in temperature, precursor solution and template type. When water was used as a precursor solution, the lack of N<sub>2</sub> bubbles and SDS led to the formation of characteristic CaCO<sub>3</sub> polymorphs and morphologies. Due to the stability of calcite at ambient conditions, rhombohedral calcite particles (Figure 6.1a) were obtained at 25 °C [9]. However, with an increase in temperature, bowknot-like particles (Figure 6.1e) consisting of predominantly aragonite, the kinetically favorable polymorph of CaCO<sub>3</sub> at high temperatures, were crystallized [9]. When SDS was incorporated into the precursor solutions, calcite particles having platelet morphology (Figure 6.1b) crystallized at 25 °C. Though most of the synthesized particles had platelet morphology, microspherical aggregates consisting of calcite platelets were also present. Formation of calcite microspheres via the attachment of thin platelets was in-line with previous findings in literature, where Shen *et al.* [91] utilized poly(vinylpyrrolidone) as a water-soluble polymer and SDS as an anionic surfactant at pH 7.0 to obtain CaCO<sub>3</sub> microspheres consisting of calcite platelets. When synthesis temperature increased to 90 °C, calcite particles having platelet morphology (Figure 6.1f), rather than the kinetically favorable aragonite polymorph, were obtained. The reason for this situation could be the electrostatic interaction between the negatively charged SDS surfactant and the Ca<sup>2+</sup> cations. In fact, it was observed that the Ca<sup>2+</sup> concentration drastically increased around SDS due to their mutual electrostatic attraction [92]. Afterwards, the Ca<sup>2+</sup> cations surrounding the SDS aggregates could further attracted CO<sub>3</sub><sup>2-</sup> anions present inside the precursor solution [92]. We could speculate that the SDS aggregates could

act as heterogeneous nucleation sites and decrease the activation energy for the nucleation of stable calcite particles.

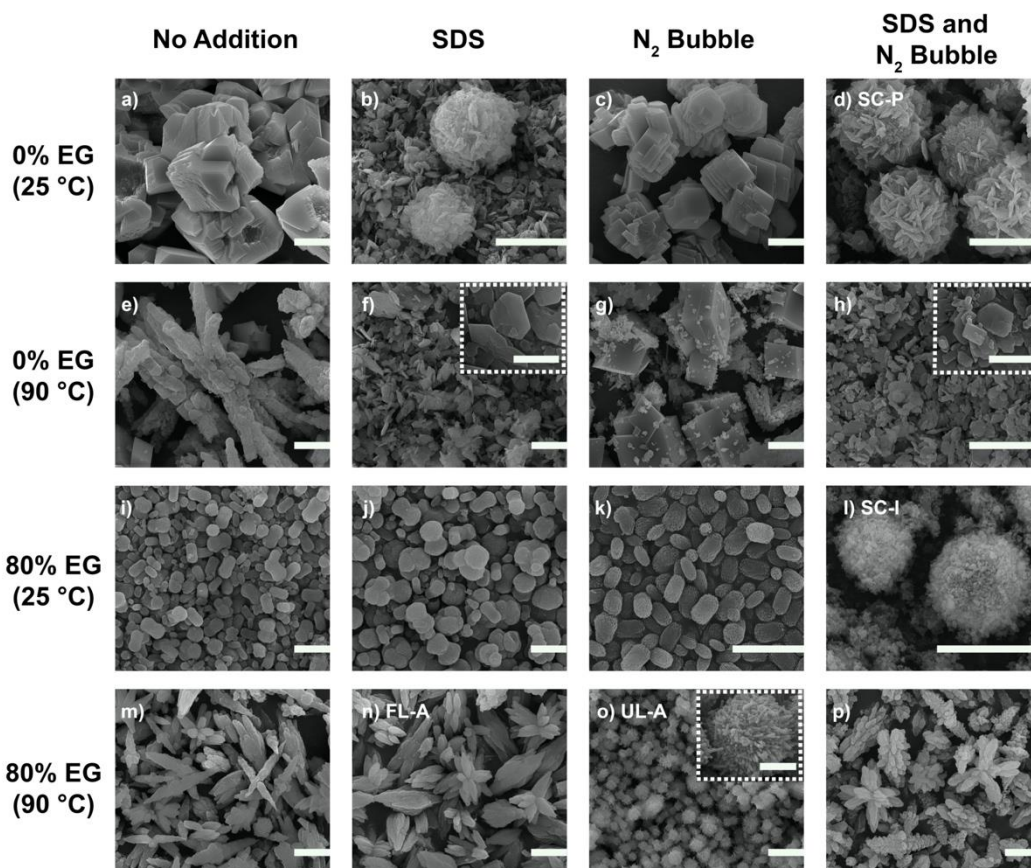


**Figure 6.1.** SEM micrographs of CaCO<sub>3</sub> particles prepared using a-d) 0% EG (25 °C), e-h) 0% EG (90 °C), i-l) 80% EG (25 °C) and m-p) 80% EG (90 °C) precursor solutions. a, e, i and m) have neither SDS nor N<sub>2</sub> bubbling, b, f, j and n) have SDS addition only, c, g, k and o) have N<sub>2</sub> bubbling only and d, h, l and p) have both SDS and N<sub>2</sub> bubbling. Platelet shaped spherical calcite (SC-P), irregular shaped spherical calcite (SC-I), flower-like aragonite (FL-A) and urchin-like aragonite (UL-A) particles are highlighted in the figure. Insets show higher magnification micrographs of the particles. Scale bars are 5 μm and 1 μm for lower and higher magnification micrographs, respectively.

When N<sub>2</sub> bubbling was incorporated into the precursor solutions, rhombohedral calcite particles (Figures 6.1c and 6.1g) were obtained independent of the synthesis temperature. There was no change in CaCO<sub>3</sub> particle morphology or polymorph upon N<sub>2</sub> bubbling (Figure 6.1c) compared to the particles synthesized without N<sub>2</sub> incorporation (Figure 6.1a), and thus N<sub>2</sub> bubbling alone was identified to be ineffective at 25 °C in aqueous media for crystallization of CaCO<sub>3</sub>. Upon increasing the synthesis temperature to 90 °C in the presence of N<sub>2</sub> bubbles (Figure 6.1g), aragonite polymorph (26.3 wt%) as well as calcite polymorph (73.7 wt%) crystallized. Crystallization of calcite could be explained with the incorporation of N<sub>2</sub> gas at room temperature into the precursor solution. Since the temperature surrounding the N<sub>2</sub> bubbles locally decreased, the synthesis conditions around the N<sub>2</sub> bubbles were suitable for spontaneous rhombohedral calcite nucleation, as it was typically observed at 25 °C. Due to the stable nature of calcite under ambient conditions, its transformation to aragonite was not favored [9]. However, during the gas bubbling step where local temperatures did not fluctuate and throughout the 4-hour aging step at 90 °C, the synthesis conditions favored aragonite crystallization (Figure 6.1g). When the effects of N<sub>2</sub> and SDS were synergistically coupled, particle morphology was considerably altered. Similar to the particles obtained upon SDS incorporation (Figures 6.1b and 6.1f), calcite particles having platelet morphology (Figures 6.1d and 6.1h) were obtained independent of the synthesis temperature. However, almost all of the platelet particles rearranged themselves to possess a microspherical morphology at 25 °C, while calcite microspheres were not present at 90 °C. Calcite microspheres having constituent particles with a platelet morphology (Figure 6.1d) was referred as ‘SC-P’ and their higher magnification image was displayed in Figure 6.2a.

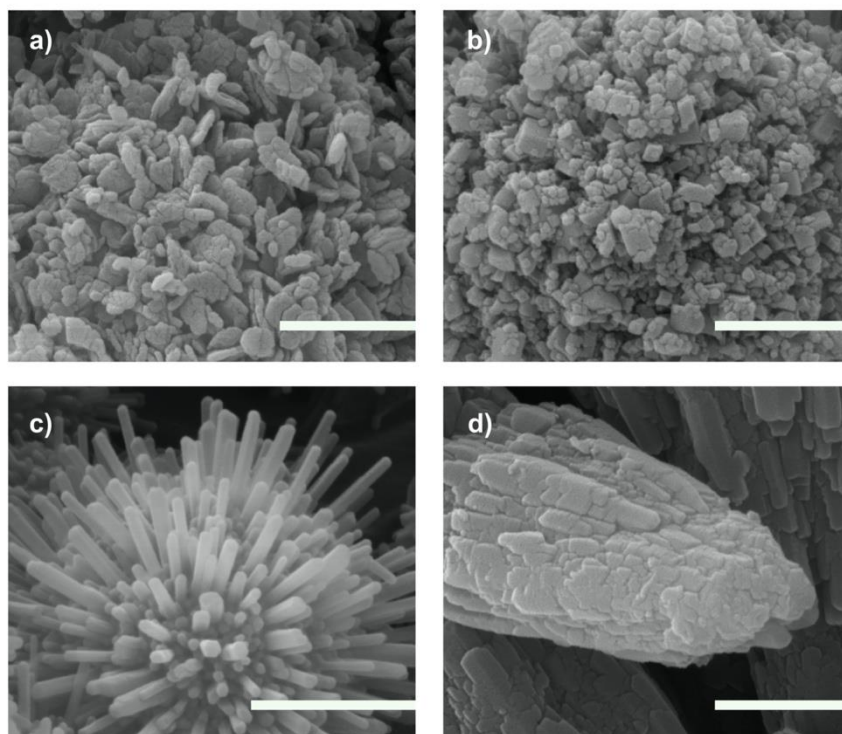


**Figure 6.2.** Surface morphologies of a) SC-P, b) SC-I, c) UL-A and d) FL-A particles. Scale bars are 1  $\mu\text{m}$ .

Similar experiments were also performed using precursor solutions containing 80% EG to identify the effects of EG on  $\text{CaCO}_3$  particle properties upon the use of  $\text{N}_2$  bubbling and SDS incorporation. When neither  $\text{N}_2$  bubbles nor SDS were introduced during particle synthesis,  $\text{CaCO}_3$  particles consisted of ellipsoidal vaterite (Figure 6.1i) and mostly flower-like aragonite (Figure 6.1m) at 25  $^\circ\text{C}$  and 90  $^\circ\text{C}$ , respectively. Once SDS was incorporated into the system, image analysis revealed  $64\% \pm 14\%$  and  $20\% \pm 4\%$  increase in average size (maximum length) of vaterite (Figure 6.1j) and aragonite (Figure 6.1n) particles, respectively. Similar results were also obtained by Qiao *et al.* [93] where increase in SDS content was correlated with an increase in average size of calcite microspheres. In this study, flower-like aragonite particles were referred as ‘FL-A’ and highlighted in Figure 6.1n and Figure 6.2c. The polymorphic and morphological changes observed for  $\text{CaCO}_3$  particles to obtain ellipsoidal vaterite and flower-like aragonite particles as per changes with EG

concentration were consistent with previous findings in literature [78]. For example, Flaten *et al.* [52] increased vaterite content of the synthesized  $\text{CaCO}_3$  particles from 0% to 65% by incorporating 75% (mono)EG into the precursor solutions. Andreassen *et al.* [70] controlled (mono)EG concentration of the precursor solutions by increasing supersaturation to alter particle morphology from dumbbell-like to spherulite. Similarly, increased branching of the aragonite polymorph obtained at 80% EG (Figure 6.1m) compared to its EG-free counterpart (Figure 6.1e) could be the result of improved nucleation rate in the growth front with an increase in supersaturation upon the EG incorporation [69]. Having this said, EG was a non-aqueous solvent miscible in water at all proportions and had high cohesive energy for  $\text{Ca}^{2+}$  ions of the precursor solutions [21]. Therefore, a local increase in supersaturation was anticipated upon EG incorporation into aqueous environments [21,29]. In addition to the increase in supersaturation due to the decrease in the solubility of  $\text{CaCO}_3$  polymorphs with an increase in the EG concentration, the lifetime of vaterite polymorph was also enhanced in the presence of EG, where the polymorph transformation to calcite was inhibited [66].

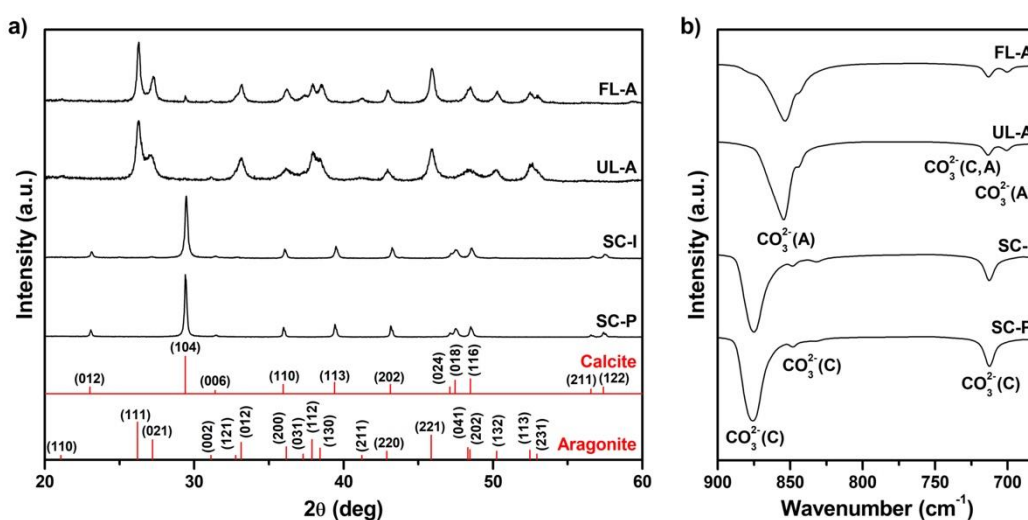


**Figure 6.3.** a) XRD and b) FTIR spectra of SC-P, SC-I, UL-A and FL-A particles. Red lines are JCPDS references for aragonite (#005-0453) and calcite (#005-0586).

‘C’ and ‘A’ denote peaks corresponding to calcite and aragonite polymorphs, respectively.

Similar to the results obtained for crystallization in water (0% EG), N<sub>2</sub> bubbling was not effective to alter particle polymorph and morphology at 25 °C (Figure 6.1k) compared to the particles synthesized without N<sub>2</sub> bubbling (Figure 6.1i). However, once solution temperature increased to 90 °C, particle morphology completely changed upon N<sub>2</sub> bubbling and urchin-like aragonite (Figure 6.1o) particles, referred as ‘UL-A’, were obtained. Similar to SC-P particles (Figure 6.1d), UL-A particles formed by the rearrangement of smaller particles in a needle-like morphology (Figure 6.2d) rather than a platelet morphology as in the case for SC-P. Once N<sub>2</sub> bubbles and SDS were both incorporated into the precursor solutions containing 80% EG, calcite microspheres (Figure 6.1l) were obtained at 25 °C. They were similar to SC-P particles synthesized at 80% EG (Figure 6.1d), yet the constituent particles of the microsphere altered from platelet to irregular morphology due to the presence of EG. In this study, calcite microspheres having irregular constituent particle morphologies were referred as ‘SC-I’ and highlighted at a higher magnification in Figure 6.2b.

**Table 6.1.** Physical properties of SC-P, SC-I, UL-A and FL-A particles.

Sample Name	CaCO <sub>3</sub> Polymorph (wt%)		Crystallite Size (nm)	Average Particle Size (μm)	Multipoint Surface Area (m <sup>2</sup> /g)
	Calcite	Aragonite			
SC-P	100	-	38.8	4.4	24.4
SC-I	98.7	1.3	30.1	4.7	28.2
UL-A	0.7	99.3	16.9	3.9	28.8
FL-A	1.6	98.4	26.6	6.8	4.7

### 6.1.2 Properties of CaCO<sub>3</sub> Microspheres

Since CaCO<sub>3</sub> microspheres exhibited promising characteristics for biomedical applications, the particles possessing spherical morphology in this study (SC-P (Figure 6.1d), SC-I (Figure 6.1l) and UL-A (Figure 6.1o)), along with FL-A particles (Figure 6.1n) as a non-spherical control group were further investigated. The percentages of each polymorph for these CaCO<sub>3</sub> particles were calculated from their XRD spectra (Figure 6.3a) using Rietveld refinement method. As shown in Table 5.1, calcite or aragonite polymorph constituted more than 98% of each investigated sample, making them almost phase-pure particles. Crystallite size of each sample was also calculated using the XRD spectra, where UL-A particles exhibited the smallest crystallite size (16.9 nm), followed by FL-A particles (26.6 nm). On the other hand, larger crystallite sizes, 38.8 nm and 30.1 nm, were present for SC-P and SC-I particles, respectively. The polymorphic analysis obtained by SEM and XRD was further supported with FTIR spectra of the particles (Figure 6.3b). Calcite and aragonite polymorphs had characteristic CO<sub>3</sub><sup>2-</sup> absorption bands within the highlighted region (900-680 cm<sup>-1</sup>). Absorption bands of calcite (at 876, 848 and 714 cm<sup>-1</sup>) [54] and aragonite (at 854, 712 and 700 cm<sup>-1</sup>) [55] were visible in the FTIR spectra of the particles. Importantly, EG (at 885 and 725 cm<sup>-1</sup>) and SDS (at 836, 763 and 722 cm<sup>-1</sup>) absorption bands were not present in the FTIR spectra, suggesting complete removal of the adsorbed EG and SDS from the CaCO<sub>3</sub> particles during particle washing steps [56,94]. Removal of these impurities was critical due to the potential toxic effects of EG and SDS in biomedical applications [21,93].

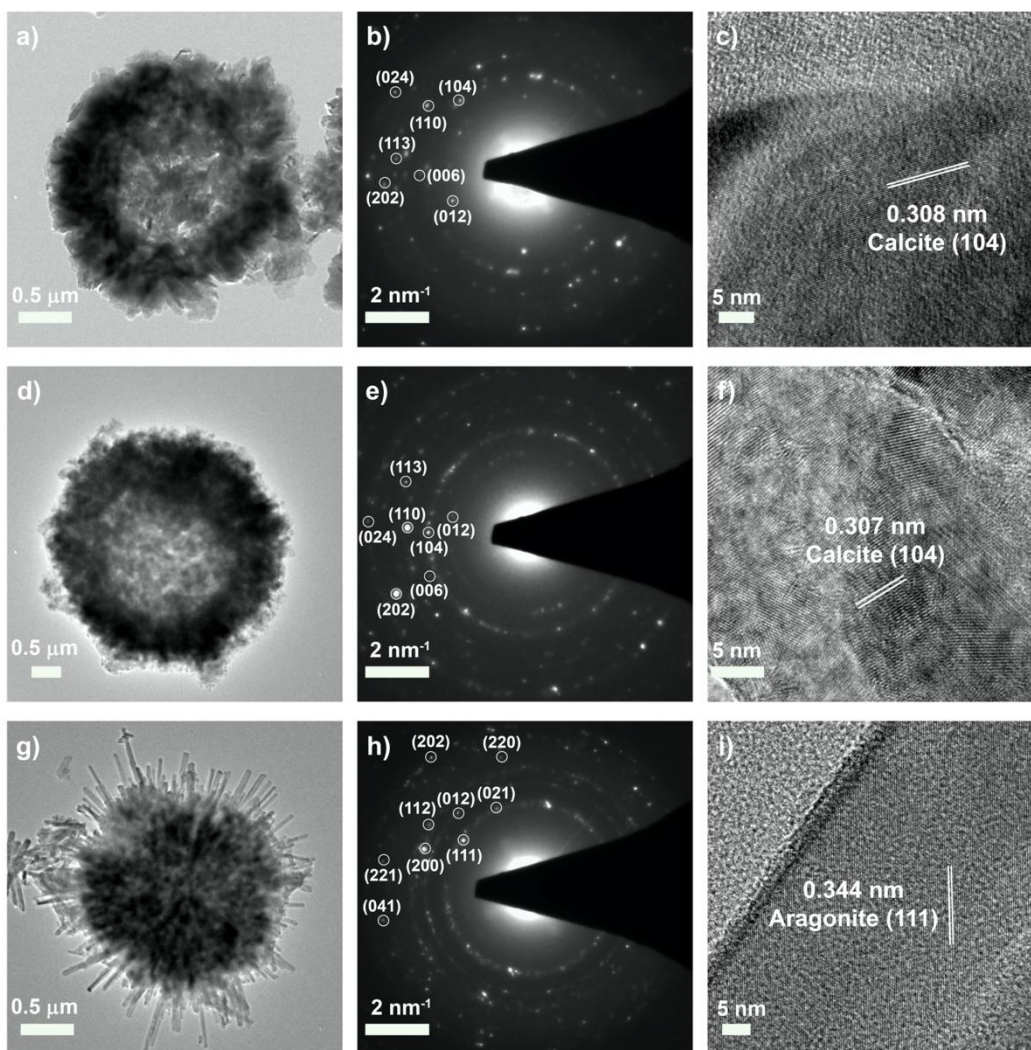


**Figure 6.4.** a, d and g) Bright-field TEM, b, e and h) SAED and c, f and i) HR-TEM micrographs of a, b and c) SC-P, d, e and f) SC-I and g, h and i) UL-A particles.

For characterization of the interior structure, particles were visualized using TEM. The hollow cores of the SC-P and SC-I particles were apparent, as shown in Figure 6.4a and d, respectively. Bright-field TEM micrographs revealed the shell thicknesses of calcite microspheres to be approximately  $0.67 \pm 0.11 \mu\text{m}$ . In literature, the shell thicknesses of hollow calcite microspheres were found to correlate with SDS concentration of the precursor solutions, and thus the SDS concentration used in this study was optimized to prevent particle fracture during synthesis with a

decrease in shell thickness [93]. For the case of UL-A particles (Figure 6.4g), instead of a hollow core observed for SC-P and SC-I particles, a porous internal structure was evident. The differences in internal structures between microspheres could be attributed to the use of N<sub>2</sub> bubbling alone for UL-A, whereas N<sub>2</sub> bubbling and SDS addition for SC-P and SC-I particles. Independent of the inner structures, polymorph analysis of CaCO<sub>3</sub> microspheres was supported with their SAED patterns (Figure 6.4b, e and h) and HR-TEM micrographs (Figure 6.4c, f and i). According to the JCPDS references for calcite (#005–0586) and aragonite (#005–0453), the d-spacing values and their corresponding planes were measured to be 0.308 nm (calcite, (104)), 0.307 nm (calcite, (104)) and 0.344 nm (aragonite, (111)) for SC-P, SC-I and UL-A particles, respectively.

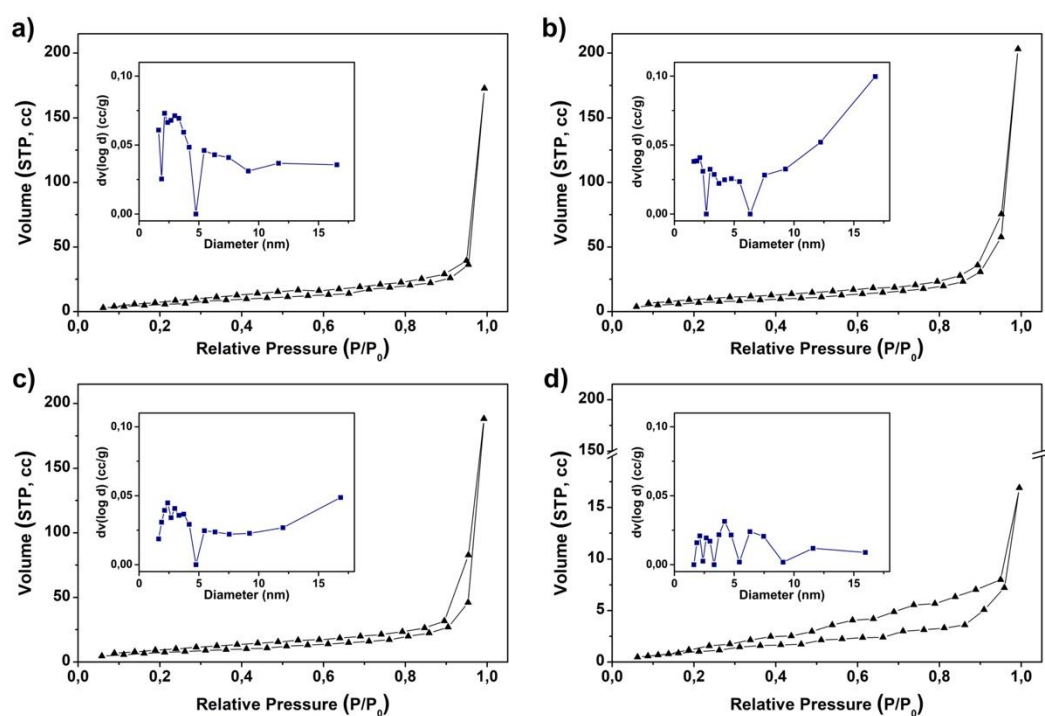


**Figure 6.5.** Nitrogen gas adsorption-desorption isotherms of a) SC-P, b) SC-I, c) UL-A and d) FL-A particles. Insets show pore size distribution of the particles.

Hollow and porous structures of the particles were also investigated using Branuer-Emmett-Teller (BET) method. As shown in Figure 6.5, particles exhibited typical V

isotherms with H3 type hysteresis loop according to International Union of Pure and Applied Chemistry (IUPAC) classification system [95]. V isotherm was correlated with relatively weak adsorbent–adsorbate interactions, whereas H3 hysteresis loop was observed at solid materials consisting of aggregates or agglomerates forming slit shaped pores having non-uniform sizes [95,96]. Multipoint surface areas of the particles (Table 5.1) showed that CaCO<sub>3</sub> microspheres expressed up to 6-fold higher surface area compared to FL-A particles. These differences could be attributed to the porous nature of the SC-P, SC-I and UL-A particles which contributed to the total surface area, while FL-A particles had a solid core. Particle pore size distributions (Figure 6.5 insets) were calculated according to Barrett-Joyner-Halenda (BJH) model and indicated that SC-P, SC-I and UL-A particles had higher concentration of meso- and macro-pores compared to FL-A particles. This result could also be related to the fact that FL-A particles had a solid core, while CaCO<sub>3</sub> microspheres investigated in this study had porous structures (Figure 6.4).

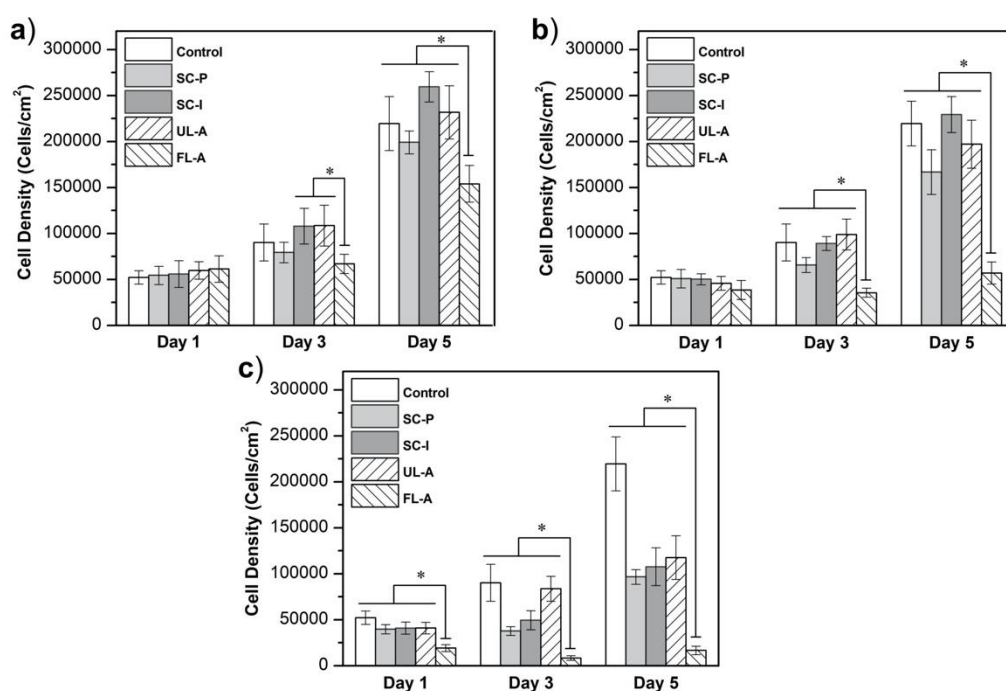


**Figure 6.6.** hFOB cell densities exposed to CaCO<sub>3</sub> particles at a) 0.01 mg/ml, b) 0.1 mg/ml and c) 1 mg/ml concentrations up to 5 days. Cells cultured without the

particles were denoted as control. The results were represented as mean  $\pm$  SD. n = 3, \*p < 0.001.

In literature, hard templates were typically used to obtain hollow CaCO<sub>3</sub> particles, yet this approach required elimination of the initial template to generate a hollow core, which was an important drawback [43,97]. In this study, inert gas (N<sub>2</sub>) bubbling was proposed as an alternative technique to overcome the drawbacks of utilizing hard templates for the synthesis of hollow CaCO<sub>3</sub> particles, including post-processing to leach particle cores and possibility of damaging structural integrity of the particles [43,97]. Since bubbles in an aqueous environment could easily dissolve due to concentration gradient across the bubble surface and the high interfacial tension between the gas and the aqueous environment, stabilizing the bubbles with different materials, *i.e.* surfactants, polymers and proteins, were proposed to enhance their stability [98,99]. Among various alternatives, an anionic surfactant (SDS) was selected in this study due to the high tendency of SDS monomers to adsorb onto the newly created interface between gas and aqueous environment, which leads to a decrease in the interfacial tension [100]. Specifically, SDS monomers self-assembled onto N<sub>2</sub> bubbles with their hydrophilic heads (SO<sub>4</sub><sup>-</sup>) facing the aqueous environment and the tails facing the N<sub>2</sub> bubble core [101]. The adsorbed SDS layer stabilized the N<sub>2</sub> bubbles, forming a spherical-shaped template for particle nucleation and attachment. Since the diffusivity of N<sub>2</sub> gas inside the bubble decreased with nucleation and attachment of more calcite particles onto the bubble surfaces, dissolution of spherical templates was limited during the synthesis processes, which allowed more nucleation, growth and attachment of CaCO<sub>3</sub> particles on the surface of these bubbles [98]. In this study, the synthesized calcite microspheres were observed to have different surface morphologies, *i.e.* platelet (Figure 6.2a) and irregular (Figure 6.2b) calcite. The difference between calcite crystallite size (Table 5.1) and morphology (Figure 6.2) between SC-P and SC-I particles could be attributed to the EG concentration of the precursor solutions. As mentioned previously, the supersaturation of the solutions increased with the incorporation of EG into the precursor solutions, which further led to an increase in nucleation rate

and thus the formation of nano-sized irregular calcite particles for SC-I (average size:  $93 \pm 25$  nm). On the other hand, when EG was not incorporated into the precursor solutions, submicron-sized platelet particles (average size:  $276 \pm 69$  nm) were obtained for SC-P [21].

The typical morphologies observed for an aragonite polymorph are needles or bundles of thin fibers. Even though the formation of needle-like aragonite particles requires relatively high temperatures, the fabrication of aragonite microspheres with a hollow interior could not be performed at 90 °C with the aid of N<sub>2</sub> bubbles and SDS. It could be speculated that the decrease in viscosity of the aqueous environment and the increased diffusivity of the N<sub>2</sub> gas with an increase in temperature could potentially contribute to the detachment of the adsorbed SDS monomers from the N<sub>2</sub> bubble surfaces and destabilize them to dissociate inside the aqueous environment [102,103]. Therefore, platelet calcite (Figure 6.1h) and FL-A (Figure 6.1p) particles were crystallized rather than CaCO<sub>3</sub> microspheres. For the case of UL-A particle crystallization, SDS-coated N<sub>2</sub> template mechanism was not applicable. Mixing the precursor solutions with intense N<sub>2</sub> bubbling could lead to UL-A formation at 80% EG. In fact, previous researchers observed polymorphic transformations upon altered precursor mixing conditions [26,104]. For instance, Santos *et al.* [17] compared mixing of precursor solutions using ultrasound or mechanical agitation and observed that aragonite content of the particles could be increased from 20.4% to 92.7% using ultrasound rather than mechanical agitation. Yang *et al.* [104] obtained rhombohedral calcite particles instead of needle-like aragonite particles by simply increasing the stirring rate of a shear mixer. Although the formation mechanism for UL-A particles requires further research, it could be speculated that needle-like aragonite particles initially precipitated to form bundles at 80% EG. Afterwards, aragonite bundles coalesced at intense N<sub>2</sub> bubbling to form porous aragonite particles. The urchin-like morphology was attained when needle-like crystallites of the coalesced aragonite particles resumed growing along their preferred planes.

As stated previously, CaCO<sub>3</sub> microspheres are suitable candidates for biomedical applications [43]. For this reason, the interaction of SC-P, SC-I, UL-A and FL-A particles with hFOB cells was investigated at 3 different concentrations up to 5 days of culture. The results showed significant difference in bone cell density between the CaCO<sub>3</sub> microspheres (SC-P, SC-I and UL-A) and FL-A particles at 0.01 mg/mL (Figure 6.6a) and 0.1 mg/mL (Figure 6.6b) concentrations at day 3 and 5. With a further increase in CaCO<sub>3</sub> concentration to 1 mg/mL (Figure 6.6c), the difference in cell densities between the CaCO<sub>3</sub> microspheres and FL-A particles became even more apparent. In fact, FL-A particles, which were proposed by other researchers for orthopedic applications [105], did not allow proliferation of bone cells at medium and high concentrations, whereas the CaCO<sub>3</sub> microspheres promoted proliferation of bone cells up to 5 days of culture. At low and medium CaCO<sub>3</sub> concentrations, the CaCO<sub>3</sub> microspheres did not exhibit any significant difference in cell densities compared to hFOB cells incubated with CaCO<sub>3</sub>-free medium, highlighting biocompatible nature of the CaCO<sub>3</sub> microspheres synthesized in this study. It should be noted that the differences in particle morphologies could be the reason for the obtained bone cell density response of the CaCO<sub>3</sub> microspheres and FL-A particles. Parakhonskiy *et al.* [36] used ellipsoidal, cuboidal and spherical CaCO<sub>3</sub> particles and observed that the frequency of particle internalization increased with an increase in the aspect ratio of the particles. In another study, cell viability was inversely correlated with the amount of internalized particles, which disrupt cell membrane and disorganize cell cytoskeleton, followed by direct interaction of the particles with intracellular organelles [81]. In addition, puncture of the cell membrane was also observed with using needle-like particles [106]. It was possible that the coupled effect of particle internalization and puncturing of cell membrane for FL-A particles, compared to the CaCO<sub>3</sub> microspheres, limited the proliferation of the bone cells and potentially decreased cell viability. On the other hand, similar bone cell densities were obtained for SC-P, SC-I and UL-A particles due to having similar aspect ratios and particle size. The biocompatible nature and stability of SC-P, SC-I and UL-A

particles indicated their high potential in biomedical applications compared to conventionally obtained form of CaCO<sub>3</sub> particles, *i.e.* flower-like aragonite.

In this study, synthesis routes for hollow and porous calcite and aragonite microspheres were identified in detail. The results showed that N<sub>2</sub> bubbles and SDS were required to synthesize hollow calcite microspheres, whereas porous aragonite microspheres could be obtained with the addition of only N<sub>2</sub> bubbles. In addition, *in vitro* experiments with human bone cells revealed that the microspheres could promote cellular proliferation compared to the conventional aragonite particles. Therefore, this study offered a novel approach to synthesize CaCO<sub>3</sub> microspheres for orthopedic applications.

## CHAPTER 7

### CONCLUSIONS AND FUTURE WORK

In this thesis, synthesis of  $\text{CaCO}_3$  particles with controlled properties was studied for their future use in biomedical applications. For this purpose, in Chapter 3, vaterite and aragonite content of the synthesized particles were enhanced using EG concentration and temperature as the experimental variables. At 25 °C, ellipsoidal and spherical vaterite particles were obtained depending on the EG concentration of the precursor solutions. When the synthesis temperature was increased to 70 °C, crab-like aragonite particles, along with ellipsoidal vaterite, were obtained. Results showed that 60% EG-containing precursor solution -without using any other additive- can prevent vaterite/aragonite to calcite transformation regardless of the synthesis temperature. At this EG concentration, vaterite (at 25 °C) and aragonite (at 70 °C) content of the synthesized particles were maximized at 98 wt% and 90 wt%, respectively. Furthermore, the size of  $\text{CaCO}_3$  particles decreased as EG concentration increased and it reached its minimum values at 80% EG where  $0.92 \pm 0.17$  and  $1.92 \pm 0.52$   $\mu\text{m}$  sized particles were obtained at 25 and 70 °C, respectively.

In Chapter 4, the effects of pH and  $[\text{Ca}^{2+}]:[\text{CO}_3^{2-}]$  ratio on the synthesized  $\text{CaCO}_3$  particles were investigated. At pH 8.0 and 10.0, spherical and ellipsoidal vaterite particles were obtained via altering  $[\text{Ca}^{2+}]:[\text{CO}_3^{2-}]$  ratio of the precursor solutions. Once pH of the precursor solutions increased to 11.0-12.0, vaterite particles transformed to calcite particles at high  $[\text{Ca}^{2+}]:[\text{CO}_3^{2-}]$  ratios, while spheroidal vaterite particles were obtained at low  $[\text{Ca}^{2+}]:[\text{CO}_3^{2-}]$  ratios. With further increase in pH to 12.0-13.0, calcite polymorph having flower-like and irregular morphologies were observed in each  $[\text{Ca}^{2+}]:[\text{CO}_3^{2-}]$  ratio investigated in this study. Along with these transformations, particle size increased from submicron to micron values by increasing the initial pH of the precursor solutions. In addition, control experiments

were performed to distinguish the effects of pH and EG concentration of the precursor solutions. It was found that pH, rather than EG concentration, was the major factor controlling CaCO<sub>3</sub> particle properties.

In Chapter 5, ellipsoidal vaterite, bowknot-like aragonite and rhombohedral calcite particles were synthesized via altering [Ca<sup>2+</sup>]:[CO<sub>3</sub><sup>2-</sup>] ratio, pH, temperature and solvent concentration. hFOB cell proliferation upon the interaction with these particles was investigated up to 5 days *in vitro*. The results highlighted the potential of ellipsoidal vaterite and rhombohedral calcite particles for orthopedic applications.

In Chapter 6, CaCO<sub>3</sub> microspheres were obtained via a novel inert gas bubbling approach. When N<sub>2</sub> bubbles and SDS were supplied to the precursor solutions at different EG concentrations, hollow calcite microspheres, having platelet and irregular constituent particle morphologies, were synthesized at 25 °C. Control experiments were also performed to distinguish the effects of N<sub>2</sub> bubbling and SDS incorporation separately on CaCO<sub>3</sub> particle properties. In addition to calcite microspheres, urchin-like aragonite microspheres with a porous structure were obtained at 90 °C by N<sub>2</sub> bubbling. Synthesized microspheres that have high specific surface area and low bulk density, along with a conventional form of aragonite, were further analyzed using hFOB cells to unveil their biological performance *in vitro*. Results showed that aragonite and calcite microspheres could promote proliferation of hFOB cells, while conventional aragonite particles were shown to decrease cellular viability.

Apart from these findings, the following points may be considered as future work. Though CaCO<sub>3</sub> particles synthesized in this thesis are suitable candidates for biomedical applications, there are still issues requiring further investigation. For example, cellular functions, including alkaline phosphatase activity and calcium phosphate mineral synthesis, should be investigated. Degradation and Ca<sup>2+</sup> release rate of the particles should also be analyzed due to their importance in biomedical applications. In addition, due to the enhanced bone cell functions on nanophase ceramic materials, efforts can be focused on synthesizing nano-sized CaCO<sub>3</sub>

particles, followed by detailed studies on the comparison of micron- and nano-sized  $\text{CaCO}_3$  particles, which are missing in literature. Having successfully completed these *in vitro* studies, one can start to work with *in vivo* models to understand the efficacy of the synthesized  $\text{CaCO}_3$  particles under more realistic conditions.

Furthermore, since  $\text{N}_2$  bubbling is a novel approach to obtain hollow  $\text{CaCO}_3$  microspheres, it may be applied to various particle synthesis systems. Along with these studies, *in situ* experiments are required to obtain a better understanding on the crystallization mechanism of the particles synthesized with this approach. In addition,  $\text{CaCO}_3$  particles are suitable candidates to be used as templates to control the properties of other materials, such as hydroxyapatite and silica. Due to the high solubility of  $\text{CaCO}_3$ , it is also possible to obtain hollow structures by removing the  $\text{CaCO}_3$  cores. Therefore, they may be ideal candidates to be used as reservoir for drug loading, highlighting the versatility of the proposed synthesis approaches in this thesis.



## REFERENCES

- [1] C. Kinnear, T.L. Moore, L. Rodriguez-Lorenzo, B. Rothen-Rutishauser, A. Petri-Fink, Form Follows Function: Nanoparticle Shape and Its Implications for Nanomedicine, *Chem. Rev.* 117 (2017) 11476–11521. <https://doi.org/10.1021/acs.chemrev.7b00194>.
- [2] C. Qi, J. Lin, L.H. Fu, P. Huang, Calcium-based biomaterials for diagnosis, treatment, and theranostics, *Chem. Soc. Rev.* 47 (2018) 357–403. <https://doi.org/10.1039/c6cs00746e>.
- [3] G. De Crozals, R. Bonnet, C. Farre, C. Chaix, Nanoparticles with multiple properties for biomedical applications: A strategic guide, *Nano Today*. 11 (2016) 435–463. <https://doi.org/10.1016/j.nantod.2016.07.002>.
- [4] V. Lauth, M. Maas, K. Rezwan, An evaluation of colloidal and crystalline properties of CaCO<sub>3</sub> nanoparticles for biological applications, *Mater. Sci. Eng. C*. 78 (2017) 305–314. <https://doi.org/10.1016/j.msec.2017.04.037>.
- [5] T. Schüler, W. Tremel, Versatile wet-chemical synthesis of non-agglomerated CaCO<sub>3</sub> vaterite nanoparticles, *Chem. Commun.* 47 (2011) 5208–5210. <https://doi.org/10.1039/c0cc05717g>.
- [6] M. Ni, B.D. Ratner, Differentiating calcium carbonate polymorphs by surface analysis techniques - An XPS and TOF-SIMS study, *Surf. Interface Anal.* 40 (2008) 1356–1361. <https://doi.org/10.1002/sia.2904>.
- [7] J. Aizenberg, G. Lambert, S. Weiner, L. Addadi, Factors involved in the formation of amorphous and crystalline calcium carbonate: A study of an ascidian skeleton, *J. Am. Chem. Soc.* 124 (2002) 32–39. <https://doi.org/10.1021/ja016990l>.
- [8] Z. Zou, W.J.E.M. Habraken, G. Matveeva, A.C.S. Jensen, L. Bertinetti, M.A. Hood, C. Sun, P.U.P.A. Gilbert, I. Polishchuk, B. Pokroy, J. Mahamid, Y. Politi, S. Weiner, P. Werner, S. Bette, R. Dinnebier, U. Kolb, E. Zolotoyabko, P. Fratzl, A hydrated crystalline calcium carbonate phase: Calcium carbonate hemihydrate, *Science* (80-. ). 363 (2019) 396–400. <https://doi.org/10.1126/science.aav0210>.
- [9] F.C. Donnelly, F. Purcell-Milton, V. Framont, O. Cleary, P.W. Dunne, Y.K. Gun'ko, Synthesis of CaCO<sub>3</sub> nano- and micro-particles by dry ice carbonation, *Chem. Commun.* 53 (2017) 6657–6660. <https://doi.org/10.1039/c7cc01420a>.
- [10] A. V. Radha, T.Z. Forbes, C.E. Killian, P.U.P.A. Gilbert, A. Navrotsky, Transformation and crystallization energetics of synthetic and biogenic amorphous calcium carbonate, *Proc. Natl. Acad. Sci. U. S. A.* 107 (2010)

16438–16443. <https://doi.org/10.1073/pnas.1009959107>.

- [11] P. Bots, L.G. Benning, J.D. Rodriguez-Blanco, T. Roncal-Herrero, S. Shaw, Mechanistic insights into the crystallization of amorphous calcium carbonate (ACC), *Cryst. Growth Des.* 12 (2012) 3806–3814. <https://doi.org/10.1021/cg300676b>.
- [12] C. Li, G.D. Botsaris, D.L. Kaplan, Selective in Vitro Effect of Peptides on Calcium Carbonate Crystallization, *Cryst. Growth Des.* 2 (2002) 387–393. <https://doi.org/10.1021/cg0255467>.
- [13] L. Brecevic, A.E. Nielsen, Solubility of amorphous calcium carbonate, *J. Cryst. Growth.* 98 (1989) 504–510. [https://doi.org/10.1016/0022-0248\(89\)90168-1](https://doi.org/10.1016/0022-0248(89)90168-1).
- [14] R. Beck, J.P. Andreassen, The onset of spherulitic growth in crystallization of calcium carbonate, *J. Cryst. Growth.* 312 (2010) 2226–2238. <https://doi.org/10.1016/j.jcrysgro.2010.04.037>.
- [15] H. Cölfen, S. Mann, Higher-order organization by mesoscale self-assembly and transformation of hybrid nanostructures, *Angew. Chemie - Int. Ed.* 42 (2003) 2350–2365. <https://doi.org/10.1002/anie.200200562>.
- [16] Y. Wang, Y.X. Moo, C. Chen, P. Gunawan, R. Xu, Fast precipitation of uniform CaCO<sub>3</sub> nanospheres and their transformation to hollow hydroxyapatite nanospheres, *J. Colloid Interface Sci.* 352 (2010) 393–400. <https://doi.org/10.1016/j.jcis.2010.08.060>.
- [17] R.M. Santos, P. Ceulemans, T. Van Gerven, Synthesis of pure aragonite by sonochemical mineral carbonation, *Chem. Eng. Res. Des.* 90 (2012) 715–725. <https://doi.org/10.1016/j.cherd.2011.11.022>.
- [18] A.C. Tas, Aragonite coating solutions (ACS) based on artificial seawater, *Appl. Surf. Sci.* 330 (2015) 262–269. <https://doi.org/10.1016/j.apsusc.2014.12.195>.
- [19] Y. Boyjoo, V.K. Pareek, J. Liu, Synthesis of micro and nano-sized calcium carbonate particles and their applications, *J. Mater. Chem. A.* 2 (2014) 14270–14288. <https://doi.org/10.1039/c4ta02070g>.
- [20] J.H. Lee, A.S. Madden, W.M. Kriven, A.C. Tas, Synthetic Aragonite (CaCO<sub>3</sub>) as a Potential Additive in Calcium Phosphate Cements: Evaluation in Tris-Free SBF at 37°C, *J. Am. Ceram. Soc.* 97 (2014) 3052–3061. <https://doi.org/10.1111/jace.13124>.
- [21] D.B. Trushina, T. V. Bukreeva, M.N. Antipina, Size-Controlled Synthesis of Vaterite Calcium Carbonate by the Mixing Method: Aiming for Nanosized Particles, *Cryst. Growth Des.* 16 (2016) 1311–1319. <https://doi.org/10.1021/acs.cgd.5b01422>.

- [22] J.P. Andreassen, Formation mechanism and morphology in precipitation of vaterite - Nano-aggregation or crystal growth?, *J. Cryst. Growth.* 274 (2005) 256–264. <https://doi.org/10.1016/j.jcrysgro.2004.09.090>.
- [23] S. Kirboga, M. Oner, E. Akyol, The effect of ultrasonication on calcium carbonate crystallization in the presence of biopolymer, *J. Cryst. Growth.* 401 (2014) 266–270. <https://doi.org/10.1016/j.jcrysgro.2013.11.048>.
- [24] O.A. Jimoh, K.S. Ariffin, H. Bin Hussin, A.E. Temitope, Synthesis of precipitated calcium carbonate: a review, *Carbonates and Evaporites.* 33 (2018) 331–346. <https://doi.org/10.1007/s13146-017-0341-x>.
- [25] Y. Mori, T. Enomae, A. Isogai, Preparation of pure vaterite by simple mechanical mixing of two aqueous salt solutions, *Mater. Sci. Eng. C.* 29 (2009) 1409–1414. <https://doi.org/10.1016/j.msec.2008.11.009>.
- [26] R. Ševčík, M. Pérez-Estébanez, A. Viani, P. Šásek, P. Mácová, Characterization of vaterite synthesized at various temperatures and stirring velocities without use of additives, *Powder Technol.* 284 (2015) 265–271. <https://doi.org/10.1016/j.powtec.2015.06.064>.
- [27] S. Yamanaka, Y. Sugawara, T. Oiso, T. Fujimoto, Y. Ohira, Y. Kuga, Phase transformation of mesoporous calcium carbonate by mechanical stirring, *CrystEngComm.* 17 (2015) 1773–1777. <https://doi.org/10.1039/c4ce02460e>.
- [28] A. Sarkar, S. Mahapatra, Synthesis of all crystalline phases of anhydrous calcium carbonate, *Cryst. Growth Des.* 10 (2010) 2129–2135. <https://doi.org/10.1021/cg9012813>.
- [29] R.-J.J. Qi, Y.-J.J. Zhu, Microwave-assisted synthesis of calcium carbonate (vaterite) of various morphologies in water - Ethylene glycol mixed solvents, *J. Phys. Chem. B.* 110 (2006) 8302–8306. <https://doi.org/10.1021/jp060939s>.
- [30] C.Y. Tai, F.B. Chen, Polymorphism of CaCO<sub>3</sub> precipitated in a constant-composition environment, *AIChE J.* 44 (1998) 1790–1798. <https://doi.org/10.1002/aic.690440810>.
- [31] S.F. Chen, S.H. Yu, J. Hang, F. Li, Y. Liu, Polymorph discrimination of CaCO<sub>3</sub> mineral in an ethanol/water solution: Formation of complex vaterite superstructures and aragonite rods, *Chem. Mater.* 18 (2006) 115–122. <https://doi.org/10.1021/cm0519028>.
- [32] Y. Chen, X. Ji, X. Wang, Microwave-assisted synthesis of spheroidal vaterite CaCO<sub>3</sub> in ethylene glycol-water mixed solvents without surfactants, *J. Cryst. Growth.* 312 (2010) 3191–3197. <https://doi.org/10.1016/j.jcrysgro.2010.07.034>.
- [33] Z. Zhang, B. Yang, H. Tang, X. Chen, B. Wang, High-yield synthesis of vaterite CaCO<sub>3</sub> microspheres in ethanol/water: structural characterization

and formation mechanisms, *J. Mater. Sci.* 50 (2015) 5540–5548.  
<https://doi.org/10.1007/s10853-015-9101-2>.

- [34] Z. Chen, Z. Nan, Controlling the polymorph and morphology of CaCO<sub>3</sub> crystals using surfactant mixtures, *J. Colloid Interface Sci.* 358 (2011) 416–422. <https://doi.org/10.1016/j.jcis.2011.02.062>.
- [35] G. Yan, L. Wang, J. Huang, The crystallization behavior of calcium carbonate in ethanol/water solution containing mixed nonionic/anionic surfactants, *Powder Technol.* 192 (2009) 58–64.  
<https://doi.org/10.1016/j.powtec.2008.11.013>.
- [36] B. Parakhonskiy, M. V Zyuzin, A. Yashchenok, S. Carregal-Romero, J. Rejman, H. Möhwald, W.J. Parak, A.G. Skirtach, The influence of the size and aspect ratio of anisotropic, porous CaCO<sub>3</sub> particles on their uptake by cells, *J. Nanobiotechnology.* 13 (2015). <https://doi.org/10.1186/s12951-015-0111-7>.
- [37] D.B. Trushina, T. V. Bukreeva, T.N. Borodina, D.D. Belova, S. Belyakov, M.N. Antipina, Heat-driven size reduction of biodegradable polyelectrolyte multilayer hollow capsules assembled on CaCO<sub>3</sub> template, *Colloids Surfaces B Biointerfaces.* 170 (2018) 312–321.  
<https://doi.org/10.1016/j.colsurfb.2018.06.033>.
- [38] A. V. Ermakov, O.A. Inozemtseva, D.A. Gorin, G.B. Sukhorukov, S. Belyakov, M.N. Antipina, Influence of Heat Treatment on Loading of Polymeric Multilayer Microcapsules with Rhodamine B, *Macromol. Rapid Commun.* 1800200 (2018) 1–6. <https://doi.org/10.1002/marc.201800200>.
- [39] S. Schmidt, K. Uhlig, C. Duschl, D. Volodkin, Stability and cell uptake of calcium carbonate templated insulin microparticles, *Acta Biomater.* 10 (2014) 1423–1430. <https://doi.org/10.1016/j.actbio.2013.11.011>.
- [40] A.C. Tas, Use of Vaterite and Calcite in Forming Calcium Phosphate Cement Scaffolds. *Developments in Porous, Biological and Geopolymer Ceramics, Eng. Sci. Proc.* 28 (2008) 135–150.
- [41] J. Rodríguez-Sánchez, B. Myszka, A.R. Boccaccini, D.K. Dysthe, Setting behavior and bioactivity assessment of calcium carbonate cements, *J. Am. Ceram. Soc.* 102 (2019) 6980–6990. <https://doi.org/10.1111/jace.16593>.
- [42] M.A.E. Cruz, G.C.M. Ruiz, A.N. Faria, D.C. Zancanela, L.S. Pereira, P. Ciancaglini, A.P. Ramos, Calcium carbonate hybrid coating promotes the formation of biomimetic hydroxyapatite on titanium surfaces, *Appl. Surf. Sci.* 370 (2016) 459–468. <https://doi.org/10.1016/j.apsusc.2015.12.250>.
- [43] W. Wei, G. Hu, D. Yu, T. Mcleish, Z. Su, Z. Shen, Preparation of Hierarchical Hollow CaCO<sub>3</sub> Particles and the Application as Anticancer Drug Carrier, *J. Am. Chem. Soc.* 130 (2008) 15808–15810.

- [44] C. Foss, M. Fedel, R. Antolini, A. Motta, C. Migliaresi, A. Haase, E. Carletti, B. V. Parakhonskiy, Tailored intracellular delivery via a crystal phase transition in 400 nm vaterite particles, *Biomater. Sci.* 1 (2013) 1273. <https://doi.org/10.1039/c3bm60141b>.
- [45] B. V. Parakhonskiy, A.M. Yashchenok, S. Donatan, D. V. Volodkin, F. Tessarolo, R. Antolini, H. Möhwald, A.G. Skirtach, Macromolecule Loading into Spherical, Elliptical, Star-Like and Cubic Calcium Carbonate Carriers, *ChemPhysChem.* 15 (2014) 2817–2822. <https://doi.org/10.1002/cphc.201402136>.
- [46] B.H. Toby, R.B. Von Dreele, GSAS-II: The genesis of a modern open-source all purpose crystallography software package, *J. Appl. Crystallogr.* 46 (2013) 544–549. <https://doi.org/10.1107/S0021889813003531>.
- [47] F. Chen, Y.-J.J. Zhu, K.-W.W. Wang, K.-L. Le Zhao, Surfactant-free solvothermal synthesis of hydroxyapatite nanowire/nanotube ordered arrays with biomimetic structures, *CrystEngComm.* 13 (2011) 1858–1863. <https://doi.org/10.1039/c0ce00574f>.
- [48] H. Cölfen, M. Antonietti, Crystal Design of Calcium Carbonate Microparticles Using Double-Hydrophilic Block Copolymers, *Langmuir.* 14 (2002) 582–589. <https://doi.org/10.1021/la970765t>.
- [49] E.M. Flaten, M. Seiersten, J.P. Andreassen, Induction time studies of calcium carbonate in ethylene glycol and water, *Chem. Eng. Res. Des.* 88 (2010) 1659–1668. <https://doi.org/10.1016/j.cherd.2010.01.028>.
- [50] J.A. Juhasz-Bortuzzo, B. Myszka, R. Silva, A.R. Boccaccini, Sonosynthesis of Vaterite-Type Calcium Carbonate, *Cryst. Growth Des.* 17 (2017) 2351–2356. <https://doi.org/10.1021/acs.cgd.6b01493>.
- [51] G.-T. Zhou, Q.-Z. Yao, S.-Q. Fu, Y.-B. Guan, Controlled crystallization of unstable vaterite with distinct morphologies and their polymorphic transition to stable calcite, *Eur. J. Mineral.* 22 (2010) 259–269. <https://doi.org/10.1127/0935-1221/2009/0022-2008>.
- [52] E.M. Flaten, M. Seiersten, J.P. Andreassen, Polymorphism and morphology of calcium carbonate precipitated in mixed solvents of ethylene glycol and water, *J. Cryst. Growth.* 311 (2009) 3533–3538. <https://doi.org/10.1016/j.jcrysgr.2009.04.014>.
- [53] Q. Li, Y. Ding, F. Li, B. Xie, Y. Qian, Solvothermal growth of vaterite in the presence of ethylene glycol, 1,2-propanediol and glycerin, *J. Cryst. Growth.* 236 (2002) 357–362. [https://doi.org/10.1016/S0022-0248\(01\)02130-3](https://doi.org/10.1016/S0022-0248(01)02130-3).
- [54] W.-S. Kim, I. Hirasawa, W.-S. Kim, Polymorphic Change of Calcium Carbonate during Reaction Crystallization in a Batch Reactor, *Ind. Eng. Chem. Res.* 43 (2004) 2650–2657. <https://doi.org/10.1021/ie034161y>.

- [55] J. Chen, L. Xiang, Controllable synthesis of calcium carbonate polymorphs at different temperatures, *Powder Technol.* 189 (2009) 64–69. <https://doi.org/10.1016/j.powtec.2008.06.004>.
- [56] Y.I. Svenskaya, H. Fattah, O.A. Inozemtseva, A.G. Ivanova, S.N. Shtykov, D.A. Gorin, B. V. Parakhonskiy, Key Parameters for Size- and Shape-Controlled Synthesis of Vaterite Particles, *Cryst. Growth Des.* 18 (2018) 331–337. <https://doi.org/10.1021/acs.cgd.7b01328>.
- [57] B. V. Parakhonskiy, A. Haase, R. Antolini, Sub-micrometer vaterite containers: Synthesis, substance loading, and release, *Angew. Chemie - Int. Ed.* 51 (2012) 1195–1197. <https://doi.org/10.1002/anie.201104316>.
- [58] M.H. Nielsen, S. Aloni, J.J. De Yoreo, In situ TEM imaging of CaCO<sub>3</sub> nucleation reveals coexistence of direct and indirect pathways, *Science* (80-. ). 345 (2014) 1158–1162. <https://doi.org/10.1126/science.1254051>.
- [59] E.M. Pouget, P.H.H. Bomans, J.A.C.M. Goos, P.M. Frederik, G. de With, N.A.J.M. Sommerdijk, The Initial Stages of Template-Controlled CaCO<sub>3</sub> Formation Revealed by Cryo-TEM, *Science* (80-. ). 323 (2009) 1455–1458. <https://doi.org/doi:10.1126/science.1169434>.
- [60] H. Konno, Y. Nanri, M. Kitamura, Crystallization of aragonite in the causticizing reaction, *Powder Technol.* 123 (2002) 33–39. [https://doi.org/10.1016/S0032-5910\(01\)00424-7](https://doi.org/10.1016/S0032-5910(01)00424-7).
- [61] Y.S. Han, G. Hadiko, M. Fuji, M. Takahashi, Influence of initial CaCl<sub>2</sub> concentration on the phase and morphology of CaCO<sub>3</sub> prepared by carbonation, *J. Mater. Sci.* 41 (2006) 4663–4667. <https://doi.org/10.1007/s10853-006-0037-4>.
- [62] H. Tang, J. Yu, X. Zhao, D.H.L. Ng, Influence of PSSS on the morphology and polymorph of calcium carbonate in the ethanol-water mixed system, *J. Alloys Compd.* 463 (2008) 343–349. <https://doi.org/10.1016/j.jallcom.2007.09.009>.
- [63] J. Gómez-Morales, J. Torrent-Burgués, R. Rodríguez-Clemente, Nucleation of calcium carbonate at different initial pH conditions, *J. Cryst. Growth.* 169 (1996) 331–338. [https://doi.org/10.1016/S0022-0248\(96\)00381-8](https://doi.org/10.1016/S0022-0248(96)00381-8).
- [64] P.-C.C. Chen, C.Y. Tai, K.. C. Lee, Morphology and growth rate of calcium carbonate crystals in a gas-liquid-solid reactive crystallizer, *Chem. Eng. Sci.* 52 (1997) 4171–4177. [https://doi.org/10.1016/S0009-2509\(97\)00259-5](https://doi.org/10.1016/S0009-2509(97)00259-5).
- [65] J.P. Andreassen, M.J. Hounslow, Growth and aggregation of vaterite in seeded-batch experiments, *AIChE J.* 50 (2004) 2772–2782. <https://doi.org/10.1002/aic.10205>.
- [66] E.M. Flaten, M. Seiersten, J.P. Andreassen, Growth of the calcium carbonate polymorph vaterite in mixtures of water and ethylene glycol at conditions of

- gas processing, *J. Cryst. Growth*. 312 (2010) 953–960.  
<https://doi.org/10.1016/j.jcrysgr.2010.01.015>.
- [67] N. Spanos, P.G. Koutsoukos, Kinetics of Precipitation of Calcium Carbonate in Alkaline pH at Constant Supersaturation. Spontaneous and Seeded Growth, *J. Phys. Chem. B*. 102 (2002) 6679–6684.  
<https://doi.org/10.1021/jp981171h>.
- [68] L. Gránásy, T. Pusztai, G. Tegze, J.A. Warren, J.F. Douglas, Growth and form of spherulites, *Phys. Rev. E - Stat. Nonlinear, Soft Matter Phys.* 72 (2005) 1–14. <https://doi.org/10.1103/PhysRevE.72.011605>.
- [69] R. Beck, J.P. Andreassen, Spherulitic growth of calcium carbonate, *Cryst. Growth Des.* 10 (2010) 2934–2947. <https://doi.org/10.1021/cg901460g>.
- [70] J.P. Andreassen, E.M. Flaten, R. Beck, A.E. Lewis, Investigations of spherulitic growth in industrial crystallization, *Chem. Eng. Res. Des.* 88 (2010) 1163–1168. <https://doi.org/10.1016/j.cherd.2010.01.024>.
- [71] E. Ruiz-Agudo, D. Van Gemert, J. Elsen, C. Rodriguez-Navarro, K. Van Balen, Ö. Cizer, Phase and morphology evolution of calcium carbonate precipitated by carbonation of hydrated lime, *J. Mater. Sci.* 47 (2012) 6151–6165. <https://doi.org/10.1007/s10853-012-6535-7>.
- [72] O. Nilsson, J. Sternbeck, A mechanistic model for calcite crystal growth using surface speciation, *Geochim. Cosmochim. Acta.* 63 (1999) 217–225. [https://doi.org/10.1016/S0016-7037\(99\)00026-5](https://doi.org/10.1016/S0016-7037(99)00026-5).
- [73] D.B. Trushina, T. V Bukreeva, M. V Kovalchuk, M.N. Antipina, CaCO<sub>3</sub> vaterite microparticles for biomedical and personal care applications, *Mater. Sci. Eng. C*. 45 (2015) 644–658. <https://doi.org/10.1016/j.msec.2014.04.050>.
- [74] G.B. Sukhorukov, D. V. Volodkin, A.M. Günther, A.I. Petrov, D.B. Shenoy, H. Möhwald, Porous calcium carbonate microparticles as templates for encapsulation of bioactive compounds, *J. Mater. Chem.* 14 (2004) 2073–2081. <https://doi.org/10.1039/b402617a>.
- [75] E. Kon, D. Robinson, P. Verdonk, M. Drobic, J.M. Patrascu, O. Dulic, G. Gavriloic, G. Filardo, A novel aragonite-based scaffold for osteochondral regeneration: early experience on human implants and technical developments, *Injury*. 47 (2016) S27–S32. [https://doi.org/10.1016/S0020-1383\(16\)30836-1](https://doi.org/10.1016/S0020-1383(16)30836-1).
- [76] S.M. Dizaj, M. Barzegar-Jalali, M.H. Zarrintan, K. Adibkia, F. Lotfipour, Calcium carbonate nanoparticles as cancer drug delivery system, *Expert Opin. Drug Deliv.* 12 (2015) 1649–1660.  
<https://doi.org/10.1517/17425247.2015.1049530>.
- [77] Ç.M. Oral, B. Ercan, Influence of pH on morphology, size and polymorph of room temperature synthesized calcium carbonate particles, *Powder Technol.*

- 339 (2018) 781–788. <https://doi.org/10.1016/j.powtec.2018.08.066>.
- [78] Ç.M. Oral, D. Kapusuz, B. Ercan, Enhanced vaterite and aragonite crystallization at controlled ethylene glycol concentrations, *Sak. Univ. J. Sci.* 23 (2019) 129–138. <https://doi.org/10.16984/saufenbilder.433985>.
- [79] G.T. Zhou, Q.Z. Yao, J. Ni, G. Jin, Formation of aragonite mesocrystals and implication for biomineralization, *Am. Mineral.* 94 (2009) 293–302. <https://doi.org/10.2138/am.2009.2957>.
- [80] J. Zhang, F. Huang, Z. Lin, Progress of nanocrystalline growth kinetics based on oriented attachment, *Nanoscale.* 2 (2010) 18–34. <https://doi.org/10.1039/b9nr00047j>.
- [81] X.Y. Sun, Q.Z. Gan, J.M. Ouyang, Size-dependent cellular uptake mechanism and cytotoxicity toward calcium oxalate on Vero cells, *Sci. Rep.* 7 (2017). [https://doi.org/10.1038/srep41949\\_1](https://doi.org/10.1038/srep41949_1).
- [82] X. Geng, L. Liu, J. Jiang, S.H. Yu, Crystallization of CaCO<sub>3</sub> mesocrystals and complex aggregates in a mixed solvent media using polystyrene sulfonate as a crystal growth modifier, *Cryst. Growth Des.* 10 (2010) 3448–3453. <https://doi.org/10.1021/cg100206y>.
- [83] J. Ahmed, Menaka, A.K. Ganguli, Controlled growth of nanocrystalline rods, hexagonal plates and spherical particles of the vaterite form of calcium carbonate, *CrystEngComm.* 11 (2009) 927–932. <https://doi.org/10.1039/b820928f>.
- [84] S. Kim, C.B. Park, Mussel-inspired transformation of CaCO<sub>3</sub> to bone minerals, *Biomaterials.* 31 (2010) 6628–6634. <https://doi.org/10.1016/j.biomaterials.2010.05.004>.
- [85] Y. Li, X. Li, Z. Cao, Y. Xu, Y. Gong, X. Shi, Fabrication of Uniform Casein/CaCO<sub>3</sub> Vaterite Microspheres and Investigation of Its Formation Mechanism, *Cryst. Growth Des.* 17 (2017) 6178–6188. <https://doi.org/10.1021/acs.cgd.7b00306>.
- [86] Q. Zhong, W. Li, X. Su, G. Li, Y. Zhou, S.C. Kundu, J. Yao, Y. Cai, Degradation pattern of porous CaCO<sub>3</sub> and hydroxyapatite microspheres in vitro and in vivo for potential application in bone tissue engineering, *Colloids Surfaces B Biointerfaces.* 143 (2016) 56–63. <https://doi.org/10.1016/j.colsurfb.2016.03.020>.
- [87] Y. Mizuno, X. Wang, M. Takahashi, H. Watanabe, M. Fuji, T. Endo, Effect of initial pH on formation of hollow calcium carbonate particles by continuous CO<sub>2</sub> gas bubbling into CaCl<sub>2</sub> aqueous solution, *Adv. Powder Technol.* 20 (2011) 89–93. <https://doi.org/10.1016/j.appt.2008.10.004>.
- [88] Y. Nakahara, M. Fujiwara, Y. Zhu, K. Shiokawa, K. Morigaki, Calcium carbonate microcapsules encapsulating biomacromolecules, *Chem. Eng. J.*

- 137 (2008) 14–22. <https://doi.org/10.1016/j.cej.2007.09.010>.
- [89] G.W. Yan, J.H. Huang, J.F. Zhang, C.J. Qian, Aggregation of hollow CaCO<sub>3</sub> spheres by calcite nanoflakes, *Mater. Res. Bull.* 43 (2008) 2069–2077. <https://doi.org/10.1016/j.materresbull.2007.09.014>.
- [90] M. Fujiwara, K. Shiokawa, M. Araki, N. Ashitaka, K. Morigaki, T. Kubota, Y. Nakahara, Encapsulation of proteins into CaCO<sub>3</sub> by phase transition from vaterite to calcite, *Cryst. Growth Des.* 10 (2010) 4030–4037. <https://doi.org/10.1021/cg100631v>.
- [91] Q. Shen, H. Wei, L. Wang, Y. Zhou, Y. Zhao, Z. Zhang, D. Wang, G. Xu, D. Xu, Crystallization and aggregation behaviors of calcium carbonate in the presence of poly(vinylpyrrolidone) and sodium dodecyl sulfate, *J. Phys. Chem. B.* 109 (2005) 18342–18347. <https://doi.org/10.1021/jp052094a>.
- [92] P. Jamrunroj, S. Wongsakulphasatch, A. Maneedaeng, C.K. Cheng, S. Assabumrungrat, Surfactant assisted CaO-based sorbent synthesis and their application to high-temperature CO<sub>2</sub> capture, *Powder Technol.* 344 (2019) 208–221. <https://doi.org/10.1016/j.powtec.2018.12.011>.
- [93] W. Qiao, X. Lan, J.K.H. Tsoi, Z. Chen, R.Y.X. Su, K.W.K. Yeung, J.P. Matinlinna, Biomimetic hollow mesoporous hydroxyapatite microsphere with controlled morphology, entrapment efficiency and degradability for cancer therapy, *RSC Adv.* 7 (2017) 44788–44798. <https://doi.org/10.1039/c7ra09204k>.
- [94] Z. Chen, Z. Nan, Effects of 1,3,5-trimethylbenzene on morphology and polymorph of CaCO<sub>3</sub> crystals in the presence of SDS, *Mater. Res. Bull.* 48 (2013) 4319–4328. <https://doi.org/10.1016/j.materresbull.2013.07.005>.
- [95] M. Thommes, K. Kaneko, A. V. Neimark, J.P. Olivier, F. Rodriguez-Reinoso, J. Rouquerol, K.S.W. Sing, Physisorption of gases, with special reference to the evaluation of surface area and pore size distribution (IUPAC Technical Report), *Pure Appl. Chem.* 87 (2015). <https://doi.org/10.1515/pac-2014-1117>.
- [96] S.H. Yu, H. Li, Q.Z. Yao, S.Q. Fu, G.T. Zhou, Hierarchically nanostructured shuttle-like aragonite mesocrystals: Preparation, characterization, growth mechanism, and removal ability to La(III), *J. Environ. Chem. Eng.* 5 (2017) 893–905. <https://doi.org/10.1016/j.jece.2017.01.004>.
- [97] T. Tomioka, M. Fuji, M. Takahashi, C. Takai, M. Utsuno, Hollow structure formation mechanism of calcium carbonate particles synthesized by the CO<sub>2</sub> bubbling method, *Cryst. Growth Des.* 12 (2012) 771–776. <https://doi.org/10.1021/cg201103z>.
- [98] M. Azmin, G. Mohamedi, M. Edirisinghe, E.P. Stride, Dissolution of coated microbubbles: The effect of nanoparticles and surfactant concentration,

Mater. Sci. Eng. C. 32 (2012) 2654–2658.  
<https://doi.org/10.1016/j.msec.2012.06.019>.

- [99] Z. Xing, H. Ke, J. Wang, B. Zhao, X. Yue, Z. Dai, J. Liu, Novel ultrasound contrast agent based on microbubbles generated from surfactant mixtures of Span 60 and polyoxyethylene 40 stearate, *Acta Biomater.* 6 (2010) 3542–3549. <https://doi.org/10.1016/j.actbio.2010.03.007>.
- [100] M. Kukizaki, Y. Baba, Effect of surfactant type on microbubble formation behavior using Shirasu porous glass (SPG) membranes, *Colloids Surfaces A Physicochem. Eng. Asp.* 326 (2008) 129–137.  
<https://doi.org/10.1016/j.colsurfa.2008.05.025>.
- [101] M. Parhizkar, M. Edirisinghe, E. Stride, The effect of surfactant type and concentration on the size and stability of microbubbles produced in a capillary embedded T-junction device, *RSC Adv.* 5 (2015) 10751–10762.  
<https://doi.org/10.1039/c4ra15167d>.
- [102] R. Farajzadeh, A. Andrianov, H. Bruining, P.L.J. Zitha, Comparative Study of CO<sub>2</sub> and N<sub>2</sub> Foams in Porous Media at Low and High Pressure-Temperatures, *Ind. Eng. Chem. Res.* 48 (2009) 4542–4552.
- [103] L. Zhang, X. Guo, Y. Zhang, P. Zhang, J. Kang, S. Khataniar, S. Ren, Experimental Investigation of Amine-Surfactant CO<sub>2</sub> Foam Stability Enhanced by Silica Nanoparticles, *J. Energy Resour. Technol.* 140 (2018) 112902. <https://doi.org/10.1115/1.4040205>.
- [104] C. Yang, J. Zhang, W. Li, S. Shang, C. Guo, Synthesis of aragonite CaCO<sub>3</sub> nanocrystals by reactive crystallization in a high shear mixer, *Cryst. Res. Technol.* 52 (2017) 1–7. <https://doi.org/10.1002/crat.201700002>.
- [105] H. Oudadesse, A.C. Derrien, A. Lucas-Girot, S. Martin, G. Cathelineau, T. Sauvage, G. Blondiaux, In vivo mineral composition evolution of a synthetic CaCO<sub>3</sub> aragonite used as biomaterial for osseous substitution, *Instrum. Sci. Technol.* 32 (2004) 545–554. <https://doi.org/10.1081/CI-200029803>.
- [106] F. Lebre, R. Sridharan, M.J. Sawkins, D.J. Kelly, F.J. O'Brien, E.C. Lavelle, The shape and size of hydroxyapatite particles dictate inflammatory responses following implantation, *Sci. Rep.* 7 (2017) 1–13.  
<https://doi.org/10.1038/s41598-017-03086-0>.